A General Purpose Detector Simulation for the EDDA Experiment

Application in Monte Carlo Studies of the Luminosity Detectors

Dissertation
zur
Erlangung des Doktorgrades (Dr. rer. nat.)
der
Mathematisch-Naturwissenschaftlichen Fakultät
der
Rheinischen Friedrich-Wilhelms-Universität Bonn

vorgelegt von

Rüdiger Groß-Hardt
aus
Aachen

Bonn 2001

Angefertigt mit Genehmigung der Mathematisch-Naturwissenschaftlichen
Fakultät der Rheinischen Friedrich-Wilhelms-Universität Bonn

1. Referent:	Prof. Dr. F. Hinterberger
2. Referent:	Prof. Dr. J. Ernst

Zusammenfassung

Das EDDA Experiment findet an einem internen Targetplatz des Cooler Synchrotrons COSY am Forschungszentrum Jülich statt. Das Detektorkonzept erlaubt es, mit hoher relativer Genauigkeit Anregungsfunktionen der elastischen Proton-Proton-Streuung im Bereich kinetischer Laborenergien von 500 MeV bis 2500 MeV aufzunehmen. In der ersten Phase des Experiments wurden unpolarisierte differentielle Wirkungsquerschnitte mit CH_2-Fädchentargets gemessen. Zur Simulation des EDDA-Experiments wurde das Simulationsprogramm SIGI entwickelt. SIGI basiert auf dem Simulationspaket Gismo. Dieses Programmpaket wurde u.a. um einen Programmteil namens MICRES zur Simulation hadronischer Schauer erweitert, der für den zur Verfügung stehenden Energiebereich besonders geeignet ist. Darüber hinaus wurden diverse geometrische Elemente hinzugefügt und das Unterprogramm zur Spurverfolgung durch bestimmte Teile des Detektors optimiert. Schließlich wurden ein bekanntes Simulationsproblem, das „Touching- Boundary-Problem“, gelöst. Es tritt z.B. bei Konfigurationen auf, bei denen sich zwei Detektorelemente berühren. Um die in der ersten Phase des Experimentes gemessenen Daten zu eichen, wurde die Luminosität mit Hilfe zweier Luminositätsmonitore, dem Sekundärelektronenmonitor SEM und den PIN-Dioden, aufgenommen. Bei den PIN-Dioden handelt es sich um Halbleiterdetektoren, die die vom Target emittierten δ-Elektronen messen. Die Effizienz der PIN-Dioden hängt vom Strahlimpuls ab. Um mit den PIN-Dioden gemessene Daten korrekt interpretieren zu können, muss die Effizienz mit Hilfe der Simulation bestimmt werden. Ein wichtiger Aspekt dieser Anwendung ist eine Abschätzung der systematischen Fehler der Simulation. Bezogen auf die verwendete Kombination aus zwei PIN-Dioden beträgt der systematische Fehler im überwiegenden Teil des Impulsbereichs weniger als 1,0%. Lediglich für Impulse unter 1455 MeV/c steigt der Fehler auf 3,1% an. Für eine der PIN-Dioden liegt der systematische Fehler sogar unter 0,6% im gesamten Impulsbereich. Diese Ergebnisse erlauben die Nutzung der PIN-Dioden zur Kontrolle der Messungen mit dem Sekundärelektronenmonitor SEM.

Abstract

The EDDA experiment is an internal target experiment at the Cooler Synchrotron COSY at the Forschungszentrum Jülich. It was designed to study proton-proton elastic scattering excitation functions ranging from 500 MeV to 2500 MeV of laboratory kinetic energy with high relative accuracy. In the first phase of the experiment unpolarized differential cross sections were measured using CH_2 fiber targets. To simulate the EDDA experiment, a simulation software named SIGI was developed. SIGI is based on the detector simulation toolkit Gismo. This toolkit had to be extended by a hadronic shower code named MICRES, especially suitable for the energy range available. Several geometrical elements were added and the tracking in certain parts of the detector was optimized. Finally, a well known simulation problem, the touching boundary problem, was solved. The problem occurs e.g., when two detector elements in a simulation setup touch. To normalize the data taken in the first phase of the EDDA experiment, the luminosity was measured using two luminosity monitors, the secondary electron monitor SEM and the PIN diodes. The PIN diodes are silicon detectors, measuring the δ-electrons emitted from the target. The efficiency of the PIN diodes depends on the beam momentum. To correctly interpret the data taken with the PIN diodes, their efficiency must be determined using the simulation software. An important aspect of this application are the systematic errors, which are introduced by the simulation. Referring to the employed combination of two PIN diodes the systematic error of the simulation is less than 1.0% for the major part of the momentum range. Only for momenta below 1455 MeV/c the error increases to 3.1%. For one particular PIN diode the systematic error is even less than 0.6% for the full momentum range. These results permit the use of the PIN diodes to control the proper operation of the secondary electron monitor SEM.

Contents

Chapter 1

Introduction

This chapter shows the physical motivation which led to the design of the EDDA detector. The detector setup is explained. Of special interest are two methods implemented to measure the luminosity of the COSY beam. Finally, the simulation software developed for this thesis is introduced. It is an essential part of one of the methods to measure the luminosity.

1.1 Motivation

Quantumchromodynamics is the fundamental quantum field theory of strong interaction. Intermediate energy physics is the energy domain, where meson exchange models loose their validity and perturbative methods cannot yet be applied. It is the energy domain, where effective field theories become increasingly important.

The COSY accelerator (**CO**oler **Sy**nchroton, Figure 1.1) at the Forschungszentrum Jülich was designed and built to explore the intermediate energy range with high accuracy. It allows accelerating protons and light ions from 277 MeV/c up to a maximum beam momentum of 3300 MeV/c. Up to $1 \cdot 10^{11}$ particles per cycle can be accelerated leading to high beam intensities. The beam quality can be increased using electron cooling at low energies and stochastic cooling at high energies. In the beginning of 1994, an additional polarized ion source was installed and enabled experiments with a polarized beam.

The EDDA experiment at COSY was designed to measure proton-proton elastic scattering excitation functions ranging from 500 MeV to 2500 MeV of laboratory kinetic energy. Proton-proton elastic scattering excitation functions are essential to the understanding of the short range part of the NN interaction. The medium and long range part of the NN interaction are well known nowadays. Phase shift solutions [Sto93, Arn97] give a good representation of the low energy data (below 300 MeV), which are well understood in terms of meson exchange models

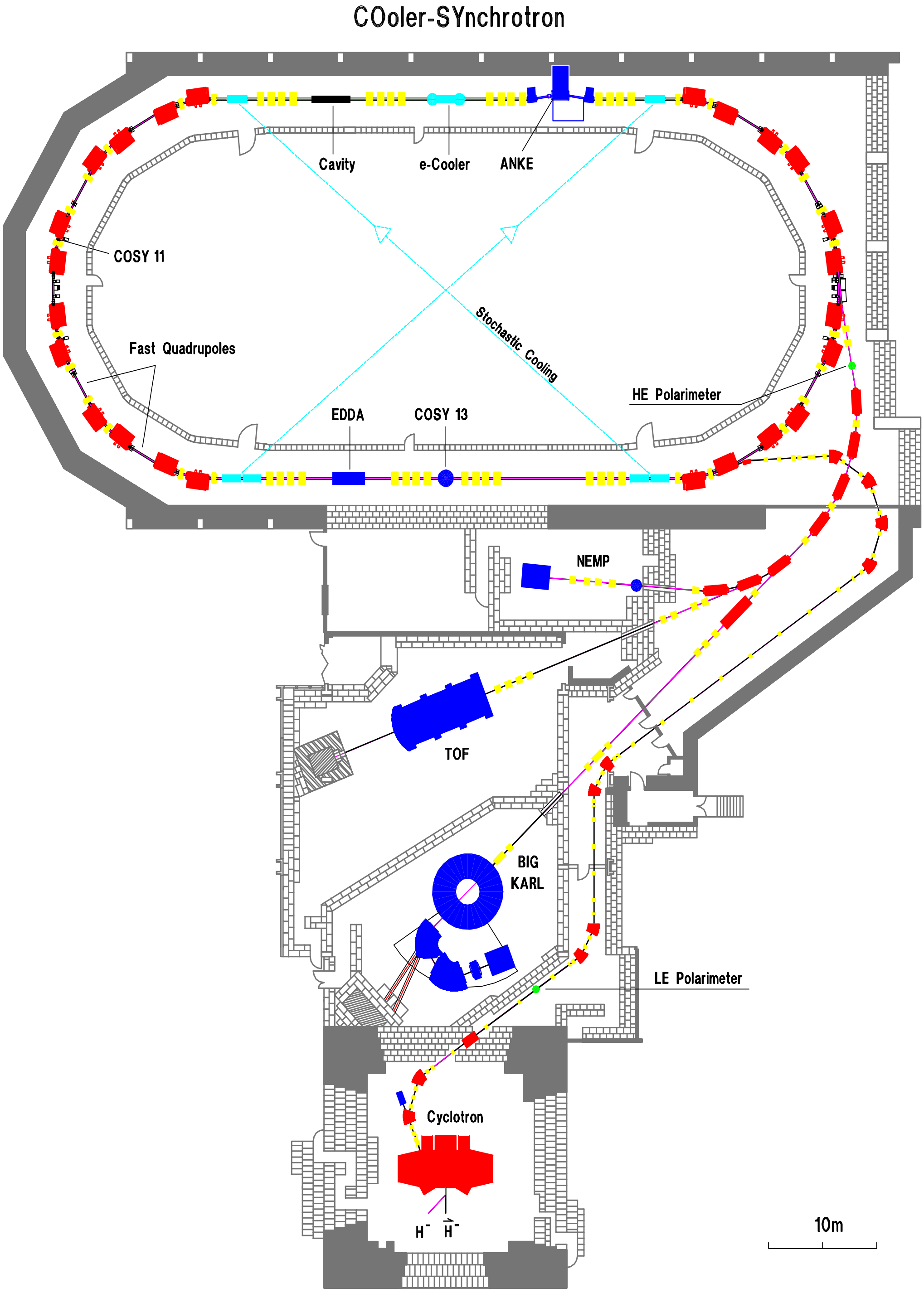

Figure 1.1: The COSY accelerator (**CO**oler **SY**nchroton) at the Forschungszentrum Jülich. The EDDA detector is positioned at the internal target position shown.

[Lac80, Mac87, Sto94]. At smaller distances (<0.8 fm), the interacting nucleons begin to overlap and meson exchange models become less adequate. The quark-gluon constituents play an increasingly important role, which may result in genuine new processes. A related problem is the nature of the repulsive core of the NN interaction. It prevents the interacting nucleons to come too close at low energies. Higher bombarding energies are needed to probe even smaller distances. In meson-theoretical models the repulsive core is due to the exchange of ω mesons. Hence, higher bombarding energies provide a means to focus on the role of the ω meson [Mac89]. Additionally, new quark-gluon processes might occur when two nucleons overlap. Also related to quark-gluon dynamics is the question of the existence or non-existence of dibaryons [Lec93]. Dibaryonic resonances with c.m. resonance energies ranging from 2.1 to 2.9 GeV are predicted by various QCD inspired models [Aer78, Won78, Won82, Laf86, Kal87, Kon87, Gol89]. No resonance at all has been confirmed so far. Excitation functions of spin correlation coefficients, i.e. cross sections depending on the relative spin orientation of the two incoming protons, provide an especially sensitive test for dibaryonic resonances. The high sensitivity is due to the interference between resonant and nonresonant amplitudes.

Therefore, a high precision measurement of elastic proton-proton excitation functions, unpolarized and polarized, should provide the means to answer some of these questions. This goal motivated design, construction and operation of the EDDA experiment at COSY.

1.2 Experimental Technique

The EDDA experiment is an internal target experiment at COSY. It takes advantage of the high quality of the COSY beam to measure elastic proton-proton scattering excitation functions with high precision at intermediate energies. Previous measurements of this reaction included only angular distributions at discrete energies or excitation functions at fixed scattering angles [Gar85, KEK94]. Consequently existing data were sparse and inconsistent, particularly above 1200 MeV incident proton kinetic energy. The EDDA experiment was designed to measure simultaneously differential cross sections covering about 85% of 4π in the c.m system with incident proton energies ranging from 500 to 2500 MeV in the laboratory frame. Data are taken repeatedly during the acceleration ramp in a multipass technique [Hin89]. This allows to eliminate systematic errors from long term effects, such as target degradation.

The EDDA experiment was scheduled to take place in two phases. During the first phase, differential cross sections were measured utilizing an unpolarized beam and an unpolarized target. Results from the analysis of $1.5 \cdot 10^7$ pp-elastic events were published in [Alb97], while additional $3{\cdot}10^7$ events were analyzed in [Wel98]. The results of the EDDA experiment so far provide consistent pp-elastic differential cross sections covering an incident proton momentum p_p from 1100 MeV/c to 3300 MeV/c and a scattering angle $\theta_{c.m.}$ from 35° to 90°. Figure 1.2 a) shows very nicely that the data subset published in [Alb97] enhances the data base in a consistent, complete manner.

For the second phase a polarized atomic beam was installed as target. Combined with the polarized beam of COSY a considerable amount of spin observables can be measured. First data measuring the analyzing power A_{00n0} were already taken in November 1998 and May 1999. According to plan, results from the second phase should considerably enhance the data of pp analyzing power A_{00n0} and spin correlation coefficients A_{00nn}, A_{00ss} and A_{00sk}, where current data today is especially sparse. Measurements of the spin correlation coefficient A_{00ss} above 600 MeV, for example, are virtually non existent, as shown in Figure 1.2 b).

A high degree of precision of differential pp-elastic cross section data, as well as analyzing powers and spin correlation coefficients, provide the data base for a consistent phase shift analysis, which in turn is the foundation of nucleon-nucleon potentials. By considerably enlarging the data base, the EDDA experiment will obviously have an impact on these analyses. The results published in [Alb97] already enabled Arndt et al. [Arn97] to extend their nucleon-nucleon elastic phase shift analysis from a projectile energy of 1.6 GeV up to 2.5 GeV.

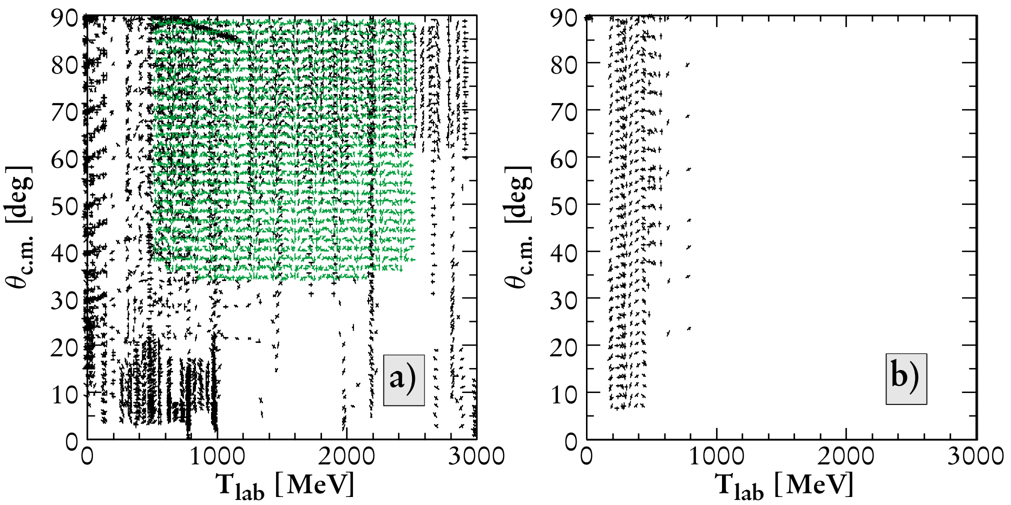

Figure 1.2: pp-elastic scattering data available today: a) spin averaged differential cross section (EDDA data published in 1997 are shown in light gray) b) spin correlation coefficient A_{00ss}. Pictures are from [Wel98] and show compiled data from SAID [Arn97].

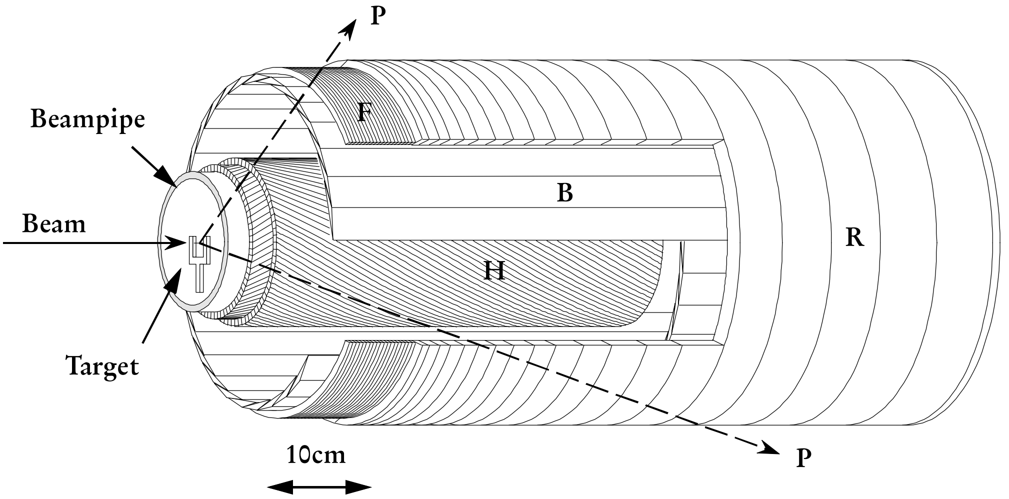

Figure 1.3: Schematic view of all elements of the EDDA detector. Presented are the inner layer (**H**), the outer layer consisting of the scintillating bars (**B**), the layer of scintillating semi-rings (**R**) and the fiber semi-rings (**F**). Unlike shown the inner detector (**H**) was not mounted during the first phase of the experiment. In the second phase the target is replaced by a polarized atomic hydrogen beam.

1.3 The EDDA Detector

The setup of the EDDA detector is presented. Figure 1.3 shows a schematic view of all detector elements, which will be presented in this section.

1.3.1 The Target

The EDDA experiment has been executed in two phases, as mentioned in the previous section.

For the first phase, a polypropylene fiber target (CH_2) of $4\,\mu\text{m} \times 5\,\mu\text{m}$ rectangular cross section was used. The CH_2-target was coated with a thin film of aluminum ($20\,\mu\text{g/cm}^2$), to allow electrons emitted from the target to be replaced by a small current from ground potential. Apart from avoiding build-up of electric charge, the measurement of the secondary electron current provides a good luminosity monitor (Subsection 1.2.5). Using the CH_2-target the reaction zone was confined to the relatively small overlap of the beam, having a width of 3 mm FWHM, and the target. The reaction vertex of an individual event is sufficiently well known. A kinematic reconstruction of each individual event using the outer layer alone is possible. To eliminate the carbon background from the CH_2-target in the offline analysis, additional data were taken with a carbon target.

During the second phase a beam of polarized hydrogen atoms is used as target. It has a diameter of about 13 mm FWHM and is surrounded by unpolarized hydrogen atoms. Therefore, the reaction vertex of each event has to be determined to allow an accurate kinematical reconstruction. In order to enable a vertex reconstruction the inner layer of the EDDA detector was designed and built [Lah92, Wie94, Jes95, Zie98, Eng98]. During the measurements of the unpolarized differential cross section data, the inner layer was not yet mounted.

1.3.2 The Outer Layer

The outer layer consists of 32 scintillator bars (**B**), surrounded by a double layer of 36 semi-rings made of scintillating fibers (**F**) and further downstream 20 solid scintillator semi-rings (**R**). It covers an angular range from $\theta_{lab} = 10°$ to $72°$, which corresponds to approximately 85% of the solid angle in the center of mass system. Seen from the target, at least two scintillator bars, as well as two semi-ring scintillators overlap. Accordingly, the spatial resolution can be increased by analyzing the fractional light output of two scintillators. This yields a resolution (FWHM) $\Delta\theta_{c.m.} = 1.0°$ and $\Delta\phi_{c.m.} = 1.9°$, which is by a factor of 5 better compared to the resolution due to the detector granularity alone.

1.3.3 The Inner Layer

The inner detector (**H**) consists of four layers of scintillating fibers. Each layer is constructed from 160 fibers of round cross section, which are helically wound around a supporting tube. Two layers are wound clockwise, the other two counter clockwise. Two layers are necessary to avoid gaps in the detection efficiency. As seen from the target two fibers of different revolution overlap, giving the inner detector its fine granularity. Monte Carlo simulation yield an angular resolution (FWHM) $\Delta\theta_{lab} = 0.53°$ and $\Delta\phi_{lab} = 0.81°$ [Tho96] due to the detector granularity.

1.3.4 Hardware Trigger

The first level trigger relies solely on the outer layer. The *coplanar trigger* requires coincident signals in two opposite scintillating bars (**B**). It takes advantage of the coplanarity of two protons in the final state, as expressed by the following relation between their azimuthal angles ϕ_{p1} and ϕ_{p2}:

$$|\phi_{p1} - \phi_{p2}| = \pi \tag{1.1}$$

In addition, the kinematic Relation (1.2) between the laboratory angles $\theta_{p1,lab}$ and $\theta_{p2,lab}$ is used for the so called *kinematic trigger*, which relies on signals from the scintillator semi-rings (**R**) and the semi-rings made from scintillating fibers (**F**).

$$\tan\theta_{p1,lab}\cdot\tan\theta_{p2,lab}=2m_p c^2/\left(T_p+2m_p c^2\right) \tag{1.2}$$

with: m_p: proton mass
T_p: kinetic beam energy

The kinematic Relation (1.2) obviously varies with the kinetic beam energy. To achieve sufficient background suppression, the kinematic trigger is adapted by reprogramming it at distinct beam energies during each acceleration cycle.

1.3.5 Luminosity Monitors

To calculate pp-elastic differential cross sections from the angular distributions measured with the outer detector during the first phase of the EDDA experiment, the luminosity has to be monitored. Two luminosity monitors are applied to this purpose, the secondary electron monitor (SEM) and the PIN diodes.

The secondary electron monitor (SEM) measures the secondary electron current emitted from the target. The electrons are from the electromagnetic cascade, which is initiated by elastic proton electron scattering in the target.

The PIN diodes are silicon detectors mounted into small windows in the beampipe. They count δ-electrons emitted from the target.

In the second phase of the experiment no direct luminosity monitoring is planned.

1.4 The PIN Diodes

Figure 1.4 shows a typical setup used to monitor the luminosity with four PIN diode detectors. They are mounted into beampipe windows at angles $\theta_{lab}=40°$ and $\phi_{lab}=0°$, 90°, 180° and 270° and in the following chapters will be referred to as left, top, right and bottom PIN diode, respectively. In April 1996, the top PIN diode was replaced by the *inner* PIN diode at $\phi_{lab}=90°$. Inside the windows the thickness of the beampipe is reduced from 2 mm to about 250 μm to minimize material between target and PIN diodes. Details of a measurement to determine the exact thickness of the beampipe windows are given in Appendix D.

PIN (or p-i-n) diodes are semiconductor diode detectors with an **i***ntrinsic* layer between **p**–type and **n**–type region of the semiconductor crystal [Kno79]. The intrinsic layer is a region of the crystal, where the concentration of donor and acceptor impurities compensate. In the fabrication process, one surface of e.g. a p–type crystal is brought into contact with donor atoms. At an elevated temperature, the donor atoms can be made to drift into the crystal, when a strong electric field is applied. Compensation of donor and acceptor impurities automatically takes place during the drifting process [Kno79]. Due to the impurities the intrin-

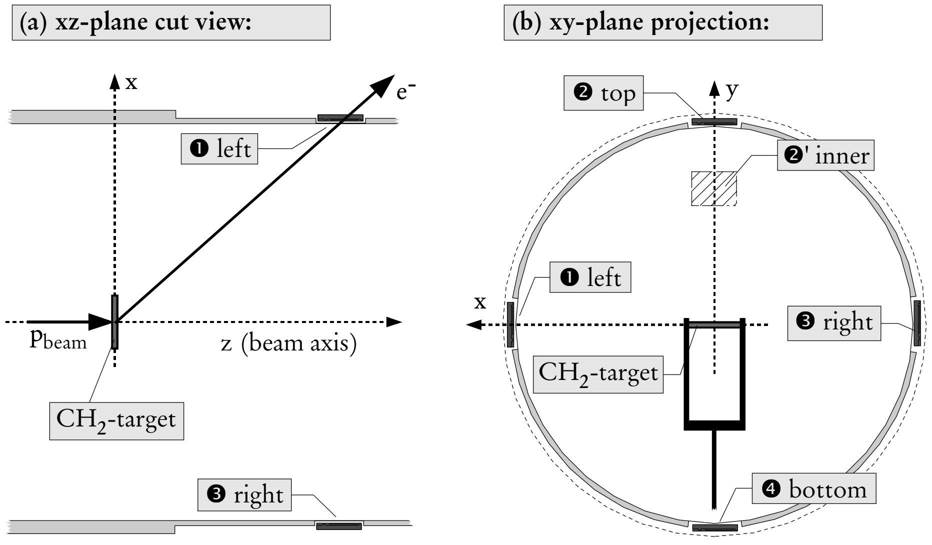

Figure 1.4: Setup of the four PIN diodes used as luminosity monitors: ❶ left PIN diode, ❷ top PIN diode, ❸ right PIN diode, ❹ bottom PIN diode. In April 1996, the top PIN diode was replaced by the inner PIN diode at position ❷'.

sic layer has a conductivity, which enables the transport of electric charge. Through the drifting process, it is possible to achieve intrinsic regions, which extend up 8-10 mm in the crystal. The intrinsic region determines the active volume of PIN diodes. For the PIN diodes used in the EDDA experiment, the active volume approximately covers an area of $10{\times}10\,\mathrm{mm}^2$ with a thickness of $339\,\mu$m. Typical charge collection times are small making PIN diodes suitable for high count rates as experienced in the EDDA experiment [Sch94]. PIN diodes made of silicon, like the ones used, are typically used for the detection and spectroscopy of X–rays, low-energy gamma rays or beta particles and slow electrons.

Early results from Monte Carlo simulations suggested that δ-electrons, emitted from the target, undergo considerable deflection in the beampipe window before hitting a PIN diode. Since the kinetic energy of the δ-electrons increases with beam momentum, the mean deflection angle decreases. This has a strong impact on the detection efficiency of the PIN diode as shown in Figure 1.5, which has to be accounted for.

The software SIGI, which is the general purpose simulation software developed for simulating the EDDA detector, was used to calculate the efficiency of the different PIN diode setups. When the results are used to correct luminosity measurements for the data taken in September 1995, PIN and SEM luminosity monitors agree on a 2.5% level. Additionally, SIGI reproduced energy loss

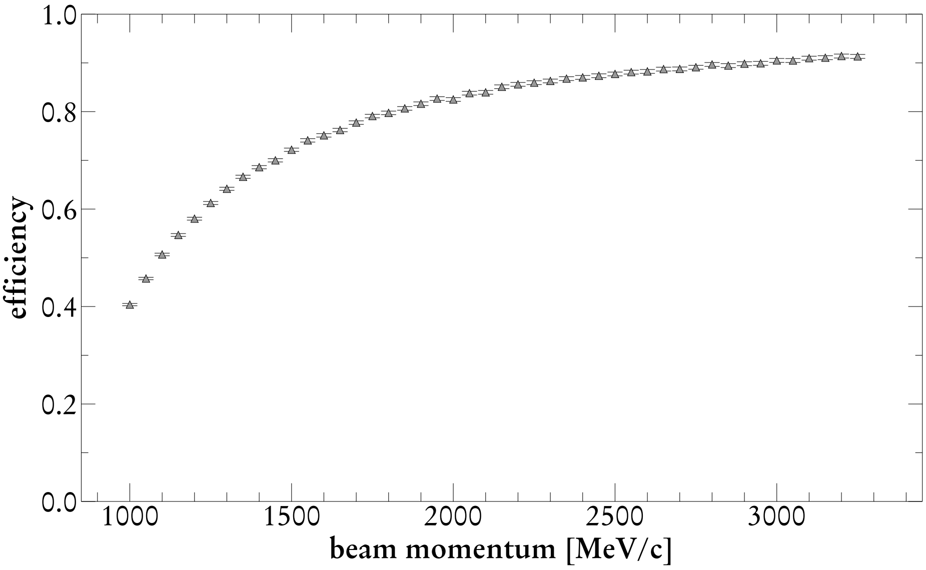

Figure 1.5: Typical electron detection efficiency of a PIN diode mounted inside a beampipe window. The example shows the efficiency of the left PIN diode and was determined using Monte Carlo simulation methods.

spectra in the PIN diodes with great precision. Still, the situation was not considered completely satisfying for several reasons:

- Typical efficiencies vary by more than a factor of 2 with beam momentum. Results rely heavily on the Monte Carlo method, while no cross-check was available to validate the method.
- The efficiency calculation requires the accurate knowledge of the beam properties.
- Apart from δ-electrons, hadronic particles are detected as well. The separation of δ-electrons from the hadronic background relies on the detection of these particles in the outer layer of the EDDA detector.

To overcome the first two problems, during the run period of April 1996 another PIN detector, called the *inner PIN diode*, was mounted inside the beampipe directly facing the target (see Figure 1.4). The inner PIN diode replaced the top PIN diode used in previous measurements. Since no additional material is positioned between target and detector, its efficiency should be constant with beam momentum. Indeed, the inner PIN diode efficiency is essentially independent of the beam momentum, as shown in Chapter 5.

In April 1996 the bottom PIN diode was mounted, but the electronic equipment to detect hadronic background in the outer layer was lacking. This inhibited background separation in the offline analysis. Consequently, the bottom PIN diode was not used as luminosity monitor. Simulating its efficiency was considered unnecessary.

To improve background separation, a new sandwich design consisting of two silicon detectors glued onto each other was successfully tested in November 1997, but never used for excitation function measurements[Hüs97].

1.5 Simulation Software

In this section several software packages used for detector simulations are introduced. The simulation software used for the EDDA detector and developed in the context of this thesis is based on the simulation toolkit Gismo. The reasons to use Gismo are presented.

1.5.1 EGS4

EGS (Electron-Gamma-Shower) was originally developed in the Mid-70's at the Stanford Linear Accelerator (SLAC) in MORTRAN[1]. The latest release is EGS4 from 1985 [Bie94, Nel85]. The primary purpose, as the name implies, was to simulate electron-gamma-showers. EGS4 never included a built-in geometry package or a hadronic shower code. For this reason it was considered inadequate as general purpose toolkit to simulate the EDDA detector.

1.5.2 GEANT III

GEANT III was an attempt to provide a package, which covered all aspects of simulating an elementary particles detector. Written in FORTRAN, it was developed at CERN from 1974 until 1994, the latest release being GEANT 3.21 [GEA95]. Due to the fact that it fulfilled most aspects it was designed for, it soon became a standard tool for detector simulation.

1.5.3 Geant 4

Geant 4 is a complete redesign of GEANT III written completely in C++. New requirements, set forth by the new detectors used e.g. at the LHC collider ring at CERN, sparked this effort, which was started in November 1994. The first production release was published in December 1998 [Gea98]. Benchmarks are very promising, showing a very fast, extensible framework suited for almost any type of particle detector and giving more accurate results than GEANT III. Geant 4 is mentioned here for completeness only, because the Geant 4 project had not even started, when development on the EDDA simulation began.

---

[1] MORTRAN is a Macro-processor, which enhances FORTRAN 77 by elements of a structured programming language

1.5.4 Gismo

Even before the Geant 4 project was launched, the need for a fast, extensible framework overcoming the shortcomings of other packages was conceived by the developers of Gismo. Gismo [Atw92, Atw93] was developed in 1993 until 1996 in a joint effort of The University of Washington, The University of Hawaii and Stanford University. It provides a C++-framework, covering all aspects of simulating a particle detector. In its original version it contained EGS4 as electromagnetic and GHEISHA as hadronic shower code.

1.5.5 The EDDA Simulation Program SIGI

When work on a simulation software for the EDDA detector was started in 1993, it soon became clear that it was impossible to extend GEANT III as to allow simulating all geometries used in the design of this detector. First simulations on trigger efficiencies restricted to the outer layer only were successfully carried out using a GEANT III based simulation package [Gro93]. However, modeling the inner layer in the framework of GEANT III posed problems, which were not easily overcome:

- The helical structure of the inner layer cannot be constructed from GEANT standard volumes.
- GEANT allows geometry extensions. Unfortunately, the interface to these extensions was not documented.
- Attempts to extract the necessary information from the source code were fruitless.

The Gismo toolkit provided a solution to these problems. Though the documentation of Gismo consists merely of an introductory tutorial, the source code is fairly self-explaining. Preliminary studies were very promising. A simulation program based on the Gismo toolkit was developed in only a month time, consisting of the essential detector elements, including the helix layer.

The hadronic shower code of both packages was found to be inappropriate for the simulation of hadrons in the intermediate energy range. It was decided to use the MICRES code [The92] as target event generator as well as hadronic shower code. At that time, MICRES was only available as hadronic shower code extension to GEANT 3.14. For GEANT as well as Gismo, this decision implied the extraction of the MICRES code from the GEANT sources [Roß94].

Based on these arguments, it was concluded in 1994 that only the Gismo package fulfilled the requirements set forth by the design of the EDDA detector.

1.6 Contents of the Thesis

Chapter 2 describes the software used to simulate the EDDA detector. Of special interest are properties of this software that allow the simulation of specific aspects of the EDDA detector. Finally, a method is presented, which solves numerical problems occurring in the original tracking algorithm, when two geometrical detector elements touch. A similar approach was developed independently in the framework of the Geant 4 project and is discussed in [Gea98b].

The simulation software SIGI was successfully applied to a variety of problems, of which the most important ones are listed here:

- calculations of the outer layer efficiency used for correction of pp-elastic angular distributions [Wei97]
- studies on the influence of the inner layer on the outer layer detection efficiency [Tho96]
- calculation of the inner layer angular resolution [Tho96]
- tests of inner layer reconstruction software [Tho96]
- initial studies of pp-inelastic background [Roh99]
- studies on the sandwich design for the PIN diodes, including effects of small magnetic fields in the target region [Hüs97]

An important application of the simulation software SIGI is to calculate the efficiencies of the different PIN diode setups mentioned in Section 1.4. This application of SIGI is introduced in the remaining chapters of this thesis.

The general method to determine these efficiencies using Monte Carlo techniques is presented in Chapter 3. Details of the simulated configuration and the analysis of the simulated data are given. Of special importance will be the concept of the *luminosity per count*, which allows describing the efficiency without referring to the specific solid angle covered by the PIN detectors.

Chapter 4 gives a detailed analysis of the errors of the luminosity measurement with PIN diodes. Of special interest are simulation related errors. The systematic error of the simulation for the combination of the left and right PIN diode is shown to be less than 1.0% for the major part of the momentum range. Only for beam momenta below 1455 MeV/c the error increases to 3.1%. For the inner PIN diode the systematic error is even less than 0.6% for the full momentum range.

In Chapter 5 the resulting efficiencies for the different beam settings of the run period of April 1996 are presented. The luminosity is calculated and compared to the luminosity measured with the secondary electron monitor SEM.

Chapter 2

Simulation Software

The following chapter describes the simulation software used in this thesis. The simulation software is based on the Gismo toolkit. Of particular interest is the way Gismo was extended to satisfy the requirements of the EDDA detector.

2.1 General Architecture

The simulation software consists of essentially two programs, one named SIGI, the other HISTO2YOD. SIGI simulates physical events, tracks the generated particles through the detector and records energy losses. These information are written to disk in a so-called history tape format. HISTO2YOD converts these information into detector signals and generates the TDAS-format, the input format for the EDDA analysis software.

2.1.1 Gismo[1]

Gismo [Atw92, Atw93] is a toolkit that enables the simulation of detectors used in medium and high energy experiments. It is mainly written in C++ and was originally developed at The University of Washington, The University of Hawaii and Stanford University. While the geometry routines and the particle tracking code were written from scratch, Gismo uses existing codes to simulate physical interactions. EGS4[2], a well established code for electromagnetic interactions originally written in Mortran3[3], was converted to C++ and included in Gismo. To simulate hadronic interactions, Gismo includes the GHEISHA [Fes85] shower code. GHEISHA was extracted from GEANT unmodified and fitted into the Gismo framework.

---

[1] Graphical Interface for Simulation and Monte Carlo with Objects

[2] Electron-Gamma-Shower Version 4

[3] Mortran3 is a Macro-processor, which enhances FORTRAN 77 by elements of a structured programming language

In 1994 T. H. Burnett from the University of Washington independently developed a version called HepGismo based on Gismo 0.4. While the geometry code was left unmodified, the particle tracking code was considerably simplified. HepGismo uses the general purpose class library CLHEP[1]. CLHEP contains codes for vector and matrix arithmetics as well as random number generation. HepGismo is the basis of our simulation software.

Gismo 2.0 combines HepGismo and Gismo 0.5, the successor to Gismo 0.4, while the geometry code was revised to remove inconsistencies (see Subsection 2.8.4). The latest release is Gismo 2.5 from April 1996. Unfortunately, the geometry code of Gismo 2.5 is not compatible with earlier versions. The use of Gismo 2.5 instead of HepGismo would have required major adjustments to our existing simulation software, yet would have delivered few benefits. Updating to Gismo 2.5 was postponed for this reason. In the rest of this text any references to Gismo will refer to HepGismo, since HepGismo is the toolkit used in our simulation software.

2.1.2 SIGI

The acronym SIGI stands for <u>S</u>imple <u>I</u>nterface to <u>G</u>ismo by <u>I</u>NI-File. As implied by its name the program SIGI is based on the Gismo toolkit. During the initialization phase SIGI reads the complete detector geometry and target event generator setup from a special initialization file (INI-file). This file is a text file in human readable format. It allows flexible access to the detector, event generator setup and most simulation parameters. After the initialization phase, SIGI enters the event generation and event tracking loop shown in Algorithm 2.1. During this loop, energy losses and other data can be stored on file or tape. SIGI uses for this purpose a special format called history tape format. It is described in detail in Subsection 2.1.4.

SIGI provides the following extensions to Gismo:

- support for several new geometries
- a method for solving the touching boundary problem (see Subsection 2.8.4)
- several new target event generators
- energy loss straggling
- MICRES[2] replaces GHEISHA as hadronic shower code [Roß94]

---

[1] <u>C</u>lass <u>L</u>ibrary for <u>H</u>igh <u>E</u>nergy <u>P</u>hysics: Unlike implied by the name CLHEP contains mostly general purpose code

[2] <u>MIC</u>roscopic <u>RES</u>onance: a hadronic shower code developed by D. Theis [The92]

- history tape format (see Subsection 2.1.4)

Since GHEISHA is not used in any simulation presented in this thesis it will not be described in this text.

2.1.3 HISTO2YOD[1]

The program HISTO2YOD reads the stored data in history tape format and converts it into 'detector signals'. For EDDA this includes energy loss and timing information in the outer layer, which are converted into digitized pulse heights and digitized time differences as well as hit patterns for the fiber rings and helix layers. This conversion takes into account light attenuation, thresholds and the trigger. The original simulation data and the simulated detector signals are stored in TDAS-format, the format used by the EDDA data acquisition and analysis software.

2.1.4 History Tape Format

The history tape format allows the complete history of an event to be stored for later analysis. This includes the following information:

1. For every generated particle:
    - type of particle (e.g. p, e^-, π^+, etc.)
    - space coordinates x,y,z where particle was generated
    - time t, when particle was generated
    - initial momentum p_x, p_y, p_z
2. After every tracking iteration moving the particle one step forward:
    - space coordinates x,y,z after step
    - time t after step
    - energy loss ΔE during last step
    - reasons for step (e.g. enter/exit a detector, stopped, etc.)

A restricted set of the above parameters, relevant to the simulation problem at hand, can be written - if the user wishes to restrict the amount of data. This selection can be made for every detector element. Unimportant detector elements, such as inactive areas, can be left out completely. Finally, SIGI permits the averaging and summation of all consecutive steps of a particle in one detector element, and the writing of only this averaged data to disk.

---

[1] The name stems from the typical file naming convention used for history tape files (.histo) and TDAS files (.yod)

2.2 General Remarks and Definitions

In order to understand the extensions made to Gismo, it is important to clarify the way the different Gismo concepts work together. To that end, the basic algorithms used in the Gismo toolkit are listed in the following sections. To ease the understanding for a reader not familiar with object oriented programming languages like C++, these algorithms are presented in a pseudo-code. To allow text references to specific lines of the pseudo-code, they are numbered. Empty lines are used to separate groups of code. Bold text denotes keywords related to control structures, such as loops and if-statements.

The approach to the architecture of the Gismo toolkit will be top-down, starting with general concepts, then filling in the details. Details of the Gismo code, deemed not essential to the understanding of how Gismo works, have been deliberately left out. This especially includes error-checking codes, and codes enabling the graceful retreat from error conditions.

Unfortunately, certain technical terms have to be used before they are properly defined. These terms are presented in the following paragraphs.

A *particle* is a particle in the classical sense, obeying the rules of special relativity. It has a well-defined position and momentum in four-dimensional space. It has a *particle type*, which determines its mass, electric charge, spin and decay width.

Tracking denotes the process of stepwise moving (propagating) a particle through the different elements of a detector setup.

A piece of code randomly generating a number of particles and their momenta at the same point in four-dimensional space is called an *event generator*. An event generator is typically part of the interaction code, which performs an interaction of a given particle with a given material, resulting in a number of secondary particles. As *target event generator* it creates the initial number of particles before tracking takes place. *Event generators* typically take the quantum mechanical nature of particles into account, when calculating the final state of an event.

Sampling is the process of selecting a (pseudo-) random number x, which is distributed according to a given probability density function $f(x)$. Two methods to sample a random number from a given probability density function, the *inverse transform* method and the *acceptance-rejection* method, are presented in [PDG94]. Both methods rely on a random generator to provide (pseudo-) random numbers equally distributed in the range $[0..1[$.

A *volume* denotes a compact subset of three-dimensional space of arbitrary shape, size and position. A volume is used to describe the geometrical aspects of detector elements. The Gismo toolkit provides several specific types of volumes, like boxes, tubes, tube segments, etc.

A *region* is a collection of parameters describing an associated volume, a magnetic field, the material filling the associated volume and the way tracking information is converted to detector signals. A *region* is used to describe all simulation related aspects of a detector element.

2.3 Setup of a Simulation Run

A simulation run consists of the geometrical setup and the setup of the target event generator. Then, as shown in Algorithm 2.1, the given number of events are generated and the particles are tracked through the detector. The data selected by the user is written to disk. SIGI also allows the user to individually switch off generation of secondary particles, multiple scattering and energy loss straggling for one complete run.

```
 1 read setup from disk
 2 for i=1 to nr. of events
 3     let event generator create beam particle and event particles
       (event particles are created as secondaries of beam particle)
 4
 5     find region inside which beam particle was created
 6     start in the region found
 7     propagate the secondary particles through all detector regions
 8
 9     clear stored energy loss, etc.
10     remove all generated particles
11 next i
```

Algorithm 2.1: Event Loop

2.4 Generating a Physical Event

The following overview shows the different target event generators used by SIGI to create the particles of a physical event (see Algorithm 2.1, line 3). This physical event typically takes place in the target. SIGI supports basically two types of event generators. The first type generates only a single particle, while the other type simulates situations in which a beam particle hits a target. Common to all generators is the code that randomly chooses the point in space, where all particles are created.

2.4.1 A Single Particle Generator

This generator, called **GunGenerator**, creates a single particle of given type, kinetic energy and direction. Its kinetic energy and direction can be sampled independently from different distributions.

2.4.2 FOWL

FOWL[1] is a phase space generator. It creates a fixed number of particles of given type in the final state with their momentum uniformly distributed in phase space. It can be used to simulate the detector response to specific reactions in the target, when the correct differential cross section is of no importance.

2.4.3 A Two Particle Final State Generator

This event generator, called **TwoParticles**, creates two particles in the final state. **TwoParticles** starts by generating a beam particle of given type, kinetic energy and randomly chosen direction. The beam particle and a target particle, of given type, which is assumed at rest in the laboratory frame, define a center of mass system. In this CM system two particles of given type are created. The magnitude of their momentum is given by energy and momentum conservation. The direction of the first particle given by (ϕ_1,θ_1) is sampled from the distributions listed in Table 2.1 in the intervals [$\theta_{1,min}$..$\theta_{1,max}$] and [$\phi_{1,min}$..$\phi_{1,max}$]. Finally, the generated particles are transformed back into the laboratory frame. SIGI can easily be enhanced by additional distributions. The **PolGen** distribution, for example, was added by E. Weise to simulate pp-elastic events given a polarized beam and target [Wei97].

Name	*Description*
ThetaGen	uniform in cos(θ_1) and ϕ_1
Rosenbluth	used to simulate $pe^- \rightarrow e^- p$ according to the Rosenbluth cross section at a given beam momentum (see Section 3.1)
PartialWave	used to simulate pp→pp at selected energies. The distribution is due to a parameterization of [Sim93]. Additional energies are possible, if appropriate parameters are found.
PolGen	used to simulate pp→pp given a polarized beam and target [Wei97]. The beam can be polarized along the y-axis, the target along all axes.

Table 2.1: Different random distributions supported by **TwoParticles**. The direction of the first generated particle is sampled from these distributions.

---

[1] This event generator was adapted from the CERN program FOWL [Jam77]

2.4.4 MICRES as Target Event Generator

The hadronic code MICRES, which simulates discrete interactions of hadrons with a given material, can also be used to generate target events. Unlike the interaction code the event generator code uses MICRES in a mode, where it is forced to create an event. It can be used to simulate inclusive reactions, where only projectile and target material are known. To adapt this generator to more specific reactions two filters can be used. A filter repeatedly lets MICRES create events until a given requirement is fulfilled. The events that are abandoned are not tracked through the detector. The first filter requires at least one particle to be emitted into a given spatial angle. It allows, for example, the examination of the effects of hadronic events in the PIN diodes without the overhead of tracking events through the detector, which would never hit a PIN diode. The other filter requires given types of particles in the final state. This filter enables examinations of specific reactions where the particles are generated according to the differential cross sections used in MICRES.

```
while particle has not stopped/interacted/decayed/left detector
    calc. $d_{phys}$, the step length restriction due to physical processes
    calc. $d_{geom}$, the distance to leave the current region
    if $d_{phys} > d_{geom}$ then
        cancel physical interaction, which led to $d_{phys}$
        perform step $d_{geom}$
        if charged particle then
            calculate energy loss, multiple scattering
        set current region to next region
    else
        cancel step into next region
        perform step $d_{phys}$
        if charged particle then
            calculate energy loss, multiple scattering
        perform selected physical interaction
end while

for i=1 to nr. of secondaries of current particle
    propagate secondary i
next i
```

Algorithm 2.2: propagate a particle and its secondaries, given the current subregion.

2.5 Tracking a Particle

The following section shows the way a particle is tracked in Gismo. Algorithm 2.2 describes the general tracking code without considering the details. Of special interest are the physical interactions supported.

2.5.1 Physical Interactions in Gismo

When tracking a particle stepwise through a detector, three principal classes of reactions are considered. There are material independent decays of unstable particles, as well as material dependent discrete and continuous interactions. The distinction between continuous and discrete interactions is artificial and made for practical reasons. Interactions of charged particles with matter like ionization or scattering off nuclei are far too numerous to simulate discretely. Instead, effective models like stopping power formulae for energy loss calculations and Molière scattering are used.

Gismo classifies the supported particles according to the model used to simulate discrete and continuous interactions, as presented in Table 2.2:

interaction model	*supported interactions*	*supported projectiles*
electromagnetic (EGS4)	*continuous interactions (charged particles):* • stopping power and Molière scattering *discrete interactions:* • e^-: Bremsstrahlung, Møller scattering • e^+: Annihilation, Bremsstrahlung, Bhabha scattering • γ: Pair production, Compton/photo effect	e^-, e^+, γ
hadronic (MICRES)	*continuous interactions (charged particles):* • stopping power from [PDG94b] • multiple scattering in Gaussian approximation from [PDG94c] *discrete interactions:* • supported particles as projectiles on target nucleus [The92]	$p, \bar{p}$ $n, \bar{n}$ π^+, π^-, π^0 K^+, K^-
default	*continuous interactions (charged particles):* • see hadronic interaction class *discrete interactions:* • none	other

Table 2.2: Gismo classification of particles according to the interaction model.

2.5.2 Step Length Restrictions due to Decays

Decays of unstable particles restrict the maximum distance a particle needs to be tracked. The time of decay τ_{decay} in the rest frame of the particle is sampled once from an exponential probability density function *f(τ)*, as soon as the particle is generated by the simulation code. The function *f(τ)* gives the probability that the particle decays in the interval $[\tau \mathinner{..} \tau+d\tau]$, where the proper time τ is measured relative to the time of creation of the particle:

$$f\left(\tau\right)=\frac{1}{\tau_{mean}}\cdot e^{-\tau/\tau_{mean}} \quad \text{with} \quad \tau_{mean}=\frac{\hbar}{\Gamma} \tag{2.1}$$

and: $\hbar$: 6.5821220 · 10^{-22} MeV s
Γ: the decay width of the particle

The time of decay τ_{decay} is only valid in the rest frame. Since charged particles constantly loose kinetic energy in matter, the rest frame slows down relative to the laboratory frame. The simulation takes this into account by updating the proper time τ of the particle after every step. Before a new step is performed the distance d_{decay} to the point of decay is calculated assuming an undisturbed flight. For charged particles the slow down due to continuous energy loss in one step is negligible and therefore ignored:

$$d_{decay}=\gamma\left(\tau_{decay}-\tau\right)\beta c \tag{2.2}$$

with: β: particle velocity in units of the speed of light
γ: Lorentz factor between rest and laboratory frame

If d_{decay} is smaller than any other step length restriction a decay of the particle is initiated. The final state particles are chosen according to the different branching ratios of the decaying particle. They are generated isotropically in the rest frame and then boosted into the laboratory frame.

2.5.3 Step Length Restrictions due to Interactions

The interaction models, which simulate particle interactions with the current material, must provide two types of information - the step length restriction set forth by the simulation of continuous processes, and the mean free path d_{mean} to the next discrete interaction. The particle momentum and the material parameters are taken into account. The mean free path d_{mean} is used to sample the distance to the next interaction $d_{interact}$ from an exponential probability density distribution *f(s)* before every step. The probability density function *f(s)* gives the probability that the particle interacts with the current material at a distance of $[s \mathinner{..} s+ds]$ relative to the current position of the particle:

$$f(s) = \frac{1}{d_{mean}} \cdot e^{-s/d_{mean}} \tag{2.3}$$

with: $d_{mean} = 1 / \sigma_{tot} \cdot N$: mean free path
σ_{tot}: total cross section
N: density of target particles / nuclei

If $d_{interact}$ is the limiting restriction to the next step, the interaction model that generated this limitation performs the interaction. The details of generating secondaries depends solely on the model used. For MICRES this is described in great detail in [Roß94] and [The92], whereas information on EGS4 can be found in [Nel85].

Sampling the distance to the next interaction $d_{interact}$ needs to be repeated before every new step, because the particle may have lost energy or stepped into a new material enforcing a recalculation of the mean free path d_{mean} by the interaction model.

2.5.4 Step Length Restrictions due to Continuous Processes

As mentioned in the last subsection, the code responsible for simulating particle / matter interactions must calculate the step length restriction set forth by the simulation of continuous processes. The hadronic and default interaction model try to limit the energy loss per step to 20% of the particle's kinetic energy:

$$d_{continuous} = f \cdot T_{kin} \ / \ \frac{dE}{dx} \tag{2.4}$$

with: T_{kin}: the particle's kinetic energy
dE/dx: stopping power of particle in current material
$f=0.2$: fractional energy loss

For charged particles both models calculate after every step the mean energy loss ΔE_{mean} using:

$$\Delta E_{mean} = s \cdot \frac{dE}{dx} \tag{2.5}$$

with: s: step length
dE/dx: stopping power of particle in current material from [PDG94b]

To enhance Gismo to support energy loss straggling the subroutine `GLANDO` and the subroutines called by `GLANDO` were extracted from GEANT 3.14. `GLANDO` calculates the deviation from the mean energy loss due to energy loss straggling. It supports automatic selection of the appropriate distribution from either Gaussian, Landau or Vavilov distributions [Bru87]. The calculated deviation is applied to the mean energy loss to give the energy loss ΔE.

To model multiple scattering the particle first looses half of ΔE. Then a scattering angle θ is sampled from the following distribution ([PDG94c]):

$$f(\theta)=\frac{\theta}{\theta_0^2}\cdot e^{-\theta^2/2\cdot\theta_0^2} \tag{2.6}$$

with: $\theta_0=\frac{13.6\,MeV}{\beta c p}\cdot z\cdot\sqrt{x/X_0}\cdot\left[1+0.038\ln\left(x/X_0\right)\right]$

θ_0: standard deviation of projected angular distribution
X_0: radiation length
$\beta c, p$: velocity and momentum of particle
z: charge number of particle
$x=s$: step length

In addition, an uniformly distributed angle ϕ is sampled from $[0..2\pi]$. Both angles are applied to find the new direction of the particle. Finally the rest of ΔE is lost.

For details on the way EGS4 simulates continuous processes the reader is referred to [Nel85] and the next section.

2.6 Electromagnetic Interactions in Gismo

To simulate electromagnetic interactions of electrons, positrons and photons Gismo uses EGS4 (Electron-Gamma-Shower version 4). Some important applications of the SIGI program, including the PIN-efficiency calculations, rely on EGS4 as electromagnetic interaction model. While in depth information on EGS4 can be found in [Nel85], this section gives an overview on the general concepts.

2.6.1 PEGS4

The EGS4 Code System is a widely used package to simulate all interactions of electrons, positrons and gammas with matter. It is written in Mortran3, a FORTRAN preprocessor package allowing structured programming and easy extendibility. The EGS4 code system consists of a preprocessor called PEGS4 (Preprocessor for EGS4) and the shower code. This separation was chosen to allow some time consuming tasks to be done ahead, resulting in faster particle tracking. To this purpose PEGS4 reads material definition files, then calculates energy dependent functions like cross sections and stopping powers. These functions are fitted by piecewise linear functions, whose parameters form a lookup table and are written to disk. The shower code then reads these lookup tables as needed.

2.6.2 Lookup Tables used for Continuous Processes

Table 2.3 shows the lookup tables used to simulate the continuous processes of charged particles: energy loss and multiple scattering. Molière scattering [Mol48, Bet53], used by EGS4 as multiple scattering model, is valid only for a limited range of Molière's parameter B [Nel85b]. For a given material this limitation can be converted into a step length restriction, which PEGS4 stores in the lookup table `TMXS`. Then the precalculated parameters χ_{r0}, t_{eff0}, b_c, χ_{cc} allow fast sampling of the scattering angle θ.

Table	*Contents*
`EDEDX`	electron stopping power
`PDEDX`	positron stopping power
`TMXS`	step length restrictions due to model dependent
`XR0,TEFF0,` `XCC,BLCC`	χ_{r0}, t_{eff0}, b_c, χ_{cc} : parameters of Molière scattering

Table 2.3: Kinetic energy dependent lookup tables generated by PEGS4 for (quasi) continuous interactions of electrons and positrons with matter.

2.6.3 Lookup Tables used for Discrete Processes

An overview of interactions supported by Gismo is given in Table 2.4. In order to sample the distance to the next discrete interaction using Equation 2.3, the mean free path d_{mean} of the given particle has to be calculated. The macroscopic cross sections listed in Table 2.5 allow an efficient calculation. For photons the mean free path d_{mean} is calculated from `GMFP`. The mean free path d_{mean} of electrons and positrons is derived from the total macroscopic cross section Σ_{total} using:

$$d_{mean} = \frac{1}{\Sigma_{total}} \tag{2.7}$$

with: $\Sigma_{total} = \sigma_{tot} \cdot N$: total macroscopic cross section
σ_{tot}: total cross section
N: density of target particles / nuclei

When a discrete electromagnetic interaction is performed, several final states can be selected. The branching ratios stored in the lookup tables listed in Table 2.6 allow a fast selection of the appropriate channel. For details of the methods used to generate angular distributions of final state particles, the reader is referred to [Nel85].

Interaction	*Cross Section*	*Physical Effect*
$e^- N \rightarrow e^- \gamma N$	Σ_{brems}	Bremstrahlung
$e^- \rightarrow e^- e^-$	$\Sigma_{møller}$	Møller scattering off atomic electrons
$e^+ N \rightarrow e^+ \gamma N$	Σ_{brems}	Bremstrahlung
$e^+ \rightarrow e^+ e^-$	Σ_{bhabha}	Bhabha scattering off atomic electrons
$e^+ e^- \rightarrow \gamma\ \gamma$	Σ_{annih}	Annihilation with atomic electrons
$\gamma \Leftrightarrow \gamma e^-$	$\Sigma_{compton}$	Compton scattering
$\gamma N \Leftrightarrow e^+ e^- N$	Σ_{pair}	Electron-positron pair production
$\gamma \Leftrightarrow e^-$	Σ_{photo}	Photo effect

Table 2.4: Overview of discrete electromagnetic interaction supported by Gismo. Interactions involving an atomic nucleus are simulated neglecting the nucleus momentum.

Table	*Contents*
`ESIG`	total macroscopic cross section $\Sigma_{total,e}$ for discrete interactions of electrons with matter
`PSIG`	total macroscopic cross section $\Sigma_{total,p}$ for discrete interactions of positrons with matter
`GMFP`	mean free path of gammas

Table 2.5: Energy dependent macroscopic cross section calculated by PEGS4. These cross sections are used by Gismo to sample the distance to the next discrete electromagnetic interaction.

Table	*Contents*
`EBR1`	electron branching ratio: $r_{br1,e} = \Sigma_{brems,e} / \Sigma_{total,e}$ $(\Sigma_{total,e} = \Sigma_{brems,e} + \Sigma_{møller})$
`PBR1`	First positron branching ratio: $r_{br1,p} = \Sigma_{brems,p} / \Sigma_{total,p}$ $(\Sigma_{total,p} = \Sigma_{brems,p} + \Sigma_{bhabha} + \Sigma_{annih})$
`PBR2`	Second positron branching ratio: $r_{br2,p} = (\Sigma_{brems,p} + \Sigma_{bhabha}) / \Sigma_{total,p}$
`GBR1`	First photon branching ratio: $r_{br1,\gamma} = \Sigma_{pair} / \Sigma_{total,\gamma}$ $(\Sigma_{total,\gamma} = \Sigma_{pair} + \Sigma_{compton} + \Sigma_{photo})$
`GBR2`	Second photon branching ratio: $r_{br2,\gamma} = (\Sigma_{pair} + \Sigma_{compton}) / \Sigma_{total,\gamma}$

Table 2.6: Table of energy dependent branching ratios. Once a discrete interaction takes place, Gismo selects the appropriate final state from these ratios.

Before incorporating the EGS4 shower code into Gismo the authors converted it to C++, in order to adapt it to the Gismo code architecture. Nevertheless, the original PEGS4-preprocessor is used to generate material data files. The macroscopic cross section in the data files are given in units of the radiation length.

2.6.4 Tracking Cuts

Apart from material parameters, the input files for PEGS4 include tracking parameters. These consist of low and high energy cuts for electrons, positrons and photons. Especially the low energy cuts are important for stopping power calculations. The production of photons below their low energy cut, for example, (soft bremstrahlung) is considered part of the stopping power for electrons. Care has to be taken to use identical cuts for PEGS4 and the simulation program. Otherwise reaction channels are double counted or missed.

2.7 Geometry

This section explains the purpose of the geometry modules of the Gismo toolkit during the tracking phase. The basic code supplied with the Gismo toolkit and its underlying concepts are presented. These concepts are crucial to understand some of the extensions made in the SIGI program to model all necessary elements of the EDDA detector.

2.7.1 Basic Considerations

The calculation of interactions like energy loss or multiple scattering is based on data of the material the particle is currently passing through. Additionally, it is essential to know the maximum distance d_{geom} the particle is allowed to propagate before it encounters a different material. This distance d_{geom} is a step length restriction due to the detector geometry. So, from the viewpoint of a particle to be propagated one step in the current material, the model of the detector geometry in the simulation code serves the following purpose:

- to calculate the distance to the boundary to a different material. This calculation must take into account the future path of the particle. The future path of the particle is given by its position and momentum and, where applicable, a magnetic field and its electric charge. This problem will be called *distance-to-boundary* problem
- to provide material data of the current material
- to convert energy loss and tracking information into 'detector signals'

To accomplish these tasks, three-dimensional space must be divided into unique *regions*. A *region* is tuple of parameters describing:

- the position and shape of a compact subset of points in three-dimensional space, called *volume*
- the properties of the material filling this subset of three-dimensional space
- the properties of the magnetic field in this *volume*, if applicable

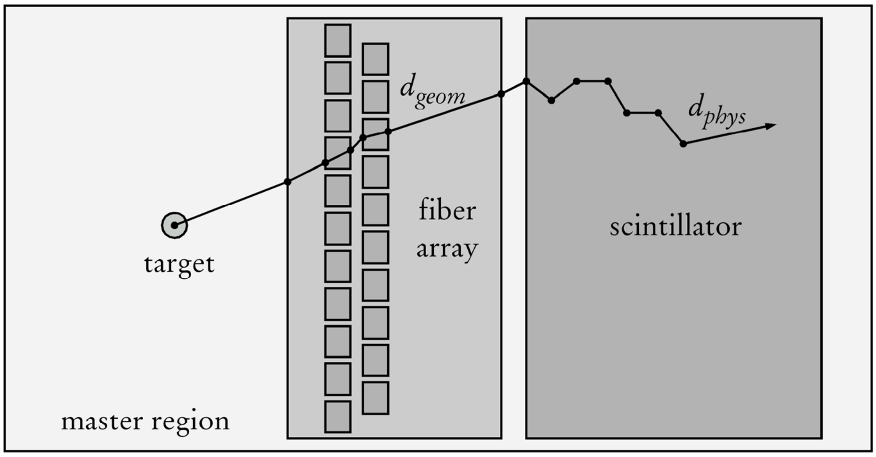

Figure 2.1: Fictitious example of single particle tracking through a Gismo hierarchy of regions with three levels. The master region contains three subregions (target, fiber array and scintillator), whereas the fiber array itself contains 21 subregions (fibers of rectangular cross section). In the scintillator stepping is restricted due to physical processes. In the previous steps tracking is interrupted at each intersection of a particle track with the boundary of a subregion.

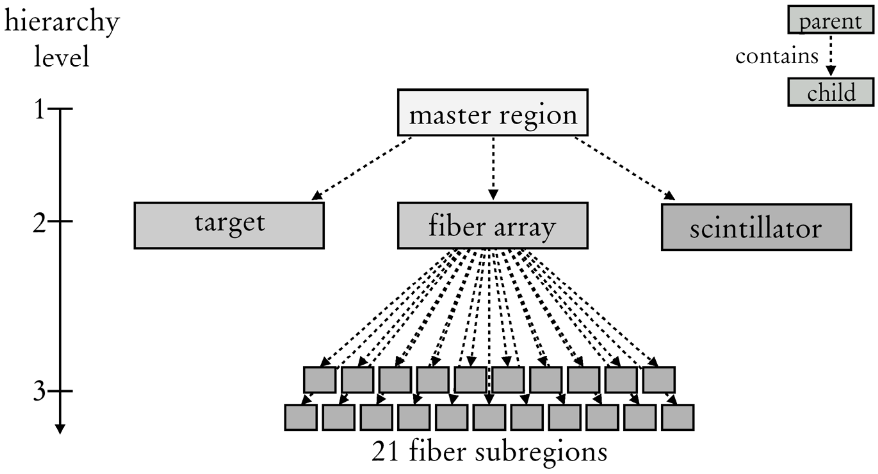

Figure 2.2: The Gismo hierarchy of Figure 2.1 presented as tree graph [Wei95]. The dashed arrows indicate the parent-child relationship between regions of different hierarchy levels. A subregion (child) is always contained in its parent region.

The division of three-dimensional space must be unique, so that each point of three-dimensional space is contained in one and only one region.

Since three-dimensional space is divided into regions, the geometry module must also permit finding the region, where tracking starts. This problem will be called the *inside* problem.

A simulation toolkit relying solely on this concept to model the detector geometry performs badly. Consider a particle leaving a given region. Because the toolkit has no other way of knowing, which region the particle passes into next, it has to check all regions defined in its setup. Toolkits like Gismo avoid this performance pitfall.

2.7.2 The Hierarchical Ansatz Of Gismo

The ansatz provided in Gismo uses a hierarchy of regions. On the first level of the hierarchy, three-dimensional space is divided into two regions, the *master region* and the rest of three-dimensional space. The *master region* is finite and contains the complete detector setup. The rest of three-dimensional space is implicitly defined by the fact that it is outside of the master region. For a particle leaving the master region tracking is stopped. The user defines shape, position and other properties of the master region during the setup of a simulation run.

On the second level of the hierarchy the master region is divided into subregions. The number of subregions, their shapes, positions and other properties are determined by the user. Each subregion itself can be divided into smaller subregions resulting in a new level in the hierarchy. There are no limits to the number of hierarchy levels except those given by practical considerations, like limited computer memory. For any region in this hierarchy the enclosing region is called *parent*, the subregions (if they exist) *children*. The master region has no parent. In computer science this data structure is called a *rooted tree* [Wei95]. Figure 2.1 and 2.2 show an example of a hierarchy with 3 levels.

The code provided by Gismo makes two assumptions:

Assumption 1: Each subregion is completely contained in its parent

Assumption 2: Different subregions of the same parent do not overlap

It should be mentioned that the union of all subregions of a region need not fill the complete volume taken up by their parent. Since the master region is finite and assumption 1 holds, the following conclusion must be satisfied:

Conclusion: All subregions must be finite

```
set $R_{next}$=R
calculate distance $d_R$ to boundary of R
if $d_R$<$d_{max}$ , set $d_{max}$=$d_R$, $R_{next}$=parent of R
for i = 1 to nr. of subregion of R
    calculate distance $d_i$ to enter subregion $S_i$
    if $d_i$<$d_{max}$ , set $d_{max}$=$d_i$ , $R_{next}$=$S_i$
next i
return distance $d_{max}$, next region $R_{next}$
```

Algorithm 2.3: Subroutine to calculate the distance to leave a given region R within a given step length restriction d_{max}, which is initially due to a physical interaction. This algorithm returns the distance found, as well as the next region the particle steps into, when leaving region R

```
 1 if p is not inside volume V then
 2     return that no region was found
 3
 4 if region R has subregions then
 5     for i=1 to nr. of subregions of region R
 6         given subregion $S_i$ call find region, inside which p lies
 7         if a region was found then
 8             return region, that was found
 9     next i
10
11 return region R
```

Algorithm 2.4: Subroutine to find the region, inside which point ***p*** lies. Given is a region R and the point ***p***, which is typically the current position of a particle. In line 6 the subroutine calls itself recursively continuing the search in subregion S_i.

Neither this conclusion nor the assumptions are directly enforced or checked, when the user sets up a detector geometry or programs a new geometrical shape. Mistakes violating one of these rules can easily be made by the user. Subsection 2.8.4 will outline an extension to Gismo, which will warn users when inconsistent tracking through the geometry due to violations of above rules occurs.

2.7.3 The Algorithms Provided By Gismo

Looking at Algorithm 2.1, line 5, the first task of the geometry code is to find the region inside which the beam particle was created. Algorithm 2.4 solves the *inside* problem for the hierarchical model of the detector geometry given in the previous subsection. Assuming that the given point $\boldsymbol{p}$, where the beam particle was created, is inside the detector, traversal of the hierarchical model of the detector geometry starts with the master region. The search continues with the first child containing the point $\boldsymbol{p}$ (Algorithm 2.4, line 6). This procedure is repeated by recursive calls to Algorithm 2.4, until a region R is found, which contains $\boldsymbol{p}$, but has no subregions containing $\boldsymbol{p}$. The subroutine, which determines, whether a given point $\boldsymbol{p}$ is contained in the volume V associated with the given region R (Algorithm 2.4, line 1), is discussed in the next subsection.

The second important problem (*distance-to-boundary* problem) during particle tracking arises, when the current step length restriction d_{max} due to physical processes has been calculated and the distance d_{geom} along the particle track to the next region boundary has to be determined (Algorithm 2.2, line 3). For Gismo's hierarchical model of the detector geometry a subregion of a given region R may have different material or other properties. Consequently, Algorithm 2.3 not only considers the *distance to leave* the given region R, but also the *distance to enter* any of its subregions. With every region examined, the step length restriction d_{max} is decreased, if an intersection of particle track and the region's surface is found and the distance to the intersection is closer than the previous step length restriction d_{max}. Calculation of the intersection (Algorithm 2.3, line 2 and 5) is related to the way Gismo models the shape of a region and is discussed in the next subsection. The step length restriction d_{max} is used by the algorithms presented in the next subsection to optimize calculations.

Algorithm 2.3 not only calculates the distance d_{next} to the next region (if it is smaller than d_{max}), but makes this next region the current one.

It is worth noting that Algorithm 2.3 makes no assumptions about the shapes or positions of the different subregions. The algorithm was designed to be independent of shape and position of the subregions and must be universally applicable to any setup satisfying assumptions 1 and 2. For periodic or uniform setups this very general solution might not be the fastest. Quite often the periodicity of a given setup allows the search for an intersection to be restricted to a small subset of all subregions. The general extendibility of the Gismo toolkit enables this approach. This was taken advantage of for the outer layer of the EDDA detector and will be shown in Subsection 2.8.3.

2.7.4 Volumes

Algorithm 2.3 leaves out the details of calculating the intersection of the particle track with a geometrical shape. To accomplish this task, Gismo again provides a general concept that can be extended to special cases. The concept described here is the one used in HepGismo. It has been simplified in Gismo 2.0 to avoid the use of finite surfaces.

In HepGismo a geometrical shape called *volume* consists of a number of several finite surfaces. These must be connected in such a way that a closed surface of the wanted shape is created. Each of the finite surfaces is embedded in an infinite sur-

```
for i=1 to nr. of finite surfaces of volume V
    calc. closest distance $d_{near}$ of point p to infinite surface $S_i$
    if abs($d_{near}$) > $d_{max}$ continue with next surface
    calc. distance $d_{intersect}$ of intersection with infinite surface $S_i$
    if point of intersection is outside finite part of surface $S_i$
        continue with next surface
    if $d_{intersect}$ < $d_{max}$ set $d_{max}$ = $d_{intersect}$
next i
return $d_{max}$
```

Algorithm 2.5: Subroutine to calculate the distance to enter a given volume V within a given step length restriction d_{max}. The distance is calculated relative to a given starting point ***p*** and direction ***d***. The point ***p*** is assumed to be outside the given volume V.

```
for i=1 to nr. of finite surfaces of volume V
    calc. closest distance $d_{near}$ of point p to infinite surface $S_i$
    if $d_{near}$ > $d_{max}$ continue with next surface
    calc. distance $d_{intersect}$ of intersection with infinite surface $S_i$
    if point of intersection lies outside finite part of surface $S_i$
        continue with next surface
    if $d_{intersect}$ < $d_{max}$ set $d_{max}$ = $d_{intersect}$
next i
return $d_{max}$
```

Algorithm 2.6: Subroutine to calculate the distance to leave a given volume V within a given step length restriction d_{max}. The distance is calculated relative to a given starting point ***p*** and direction ***d***. The point ***p*** is assumed to be inside the given volume V.

```
for i=1 to nr. of finite surfaces of volume V
    calc. closest distance $d_{near}$ of point p to infinite surface $S_i$
    if $d_{near}$ < 0 return p lies outside volume V
next i
return p lies inside volume V
```

Algorithm 2.7: Subroutine to check, whether a given point ***p*** is inside a given volume V face. Every point on this infinite surface has a normal vector, which defines an inside and outside for that infinite surface. By convention, normal vectors point to the outside of a surface. Additionally, a negative sign of d_{near}, the closest distance of a given point $\boldsymbol{p}$ to a given surface S_i, indicates that the point $\boldsymbol{p}$ is outside the surface S_i. Gismo 2.0, the successor of HepGismo, drops the concept of finite surfaces and defines a *volume* as that subset of three-dimensional space that is completely inside a given number of infinite surfaces.

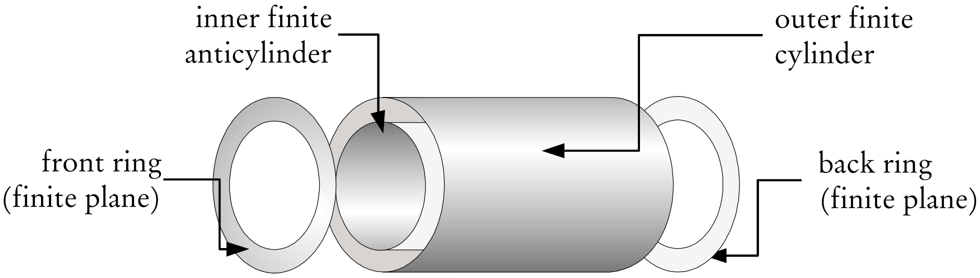

Figure 2.3: Exploded view of finite surfaces forming the volume **Tube**

A **Tube** is a good example of a *volume* provided by HepGismo. It is bounded by two rings for the front and back plane and an inner and outer cylinder of finite length (Figure 2.3). Both rings are embedded into an infinite plane, while each finite cylinder is embedded into an infinite cylinder.

Given the method of HepGismo to describe a geometric shape, Algorithms 2.5 and 2.6 provide a solution to finding the distance to enter or, respectively, the distance to leave for a given volume. Only intersections within the given step length restriction d_{max} need to be considered. The given step length restriction d_{max} is initially due to physical restrictions, but is decreased, whenever a valid intersection of the particle track and a geometric shape is found (Algorithm 2.3, lines 3 and 6, Algorithms 2.5/2.6, line 7). The basic idea of Algorithms 2.5 and 2.6 is to check all surfaces S_i defining the shape of the given volume for intersections with the particle track. Of all intersections of particle track and surfaces S_i found, the intersection closest to the particle position along the particle track is selected as the correct solution. If a correct solution is found, the distance from particle position to point of intersection is returned. For every surface S_i examined, the step length restriction d_{max} is taken advantage of to avoid unnecessary and time consuming calculations of intersections of particle track and surface S_i (Algorithms 2.5/2.6, lines 2 and 3). The idea is that a particle can never reach a surface S_i within a step length d_{max}, if its position is not closer to the surface S_i than the step length restriction d_{max}, regardless of the particle direction. Fortunately, the calculation of d_{near}, the closest distance of a given point $\boldsymbol{p}$ to a given surface S_i, is a simple task and does not introduce considerable performance penalties. Finally, if the particle position is closer to the considered surface S_i than the step length restriction d_{max}, the intersection of particle track and infinite surface S_i is computed. Algorithms 2.5/2.6 rely on the finiteness of a surface to determine, whether a calculated point of intersection with the infinite surface S_i is within the boundaries of the finite surface S_i and thus really a point of intersection with the volume surface (lines 4 and 5). This process is repeated for every surface S_i, which defines the shape of the given volume.

Algorithm 2.7, taken from the HepGismo source, tests whether a given point $\boldsymbol{p}$ in three-dimensional space is inside a given volume. It uses the Gismo 2.0 concept to define the inside of a volume. The point $\boldsymbol{p}$ is inside the given volume, if and only if the point $\boldsymbol{p}$ is inside of all surfaces S_i defining the given volume.

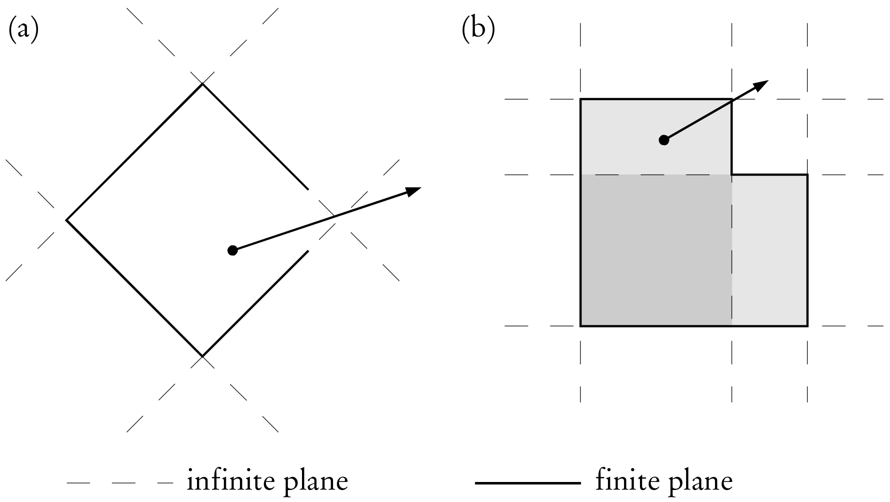

Figure 2.4: Two tracking problems resulting from inconsistent Volume definitions: (a) Finite surfaces do not connect properly → particle cannot find intersection, though it is inside the volume. (b) Particle can find distance to leave, though it is not inside all infinite surfaces

Unfortunately, the concepts of Gismo 2.0 and HepGismo to describe geometric shapes are not necessarily equivalent. An example of this inconsistency can be seen in Figure 2.4 (b). Only the dark gray area is within all infinite surfaces. Though the light gray areas are clearly within the volume defined by the finite surfaces, Algorithm 2.7 would consider them outside the given volume. In the example of Figure 2.4 this problem can be resolved by providing a different *inside* algorithm suited for the particular geometric shape. Fortunately, the volumes provided by HepGismo (**Box**, **Tube**, ..) do not suffer from this problem. Nevertheless, when programming a new volume and relying on the algorithms provided by HepGismo this should be kept in mind. The illustrated inconsistency is one of several reasons that the concept to define geometrical shapes was modified in Gismo 2.0.

Figure 2.4 (a) shows another pitfall of the HepGismo concept, when modeling user-defined shapes. The finite surfaces are not properly connected resulting in an open surface and an ill-defined volume. These inconsistencies can create tracking problems, not detected by the original HepGismo code. Again the problem is considerably eased by the concept used in Gismo 2.0. It is certainly more difficult to ensure that a number of finite surface are connected in such a way as to give a closed surface than to make certain that the inside of a number of infinite surfaces defines a valid, finite volume.

2.8 SIGI Extensions to the Gismo Toolkit

The following section presents the extensions to the Gismo toolkit, which were programmed in the framework of the SIGI program. Especially, one problem of the provided Gismo code and its solution in the framework of SIGI is described. It arises, when two detector elements need to be positioned so close to each other that their surfaces touch.

2.8.1 Beampipe and PIN Diodes

The beampipe and the PIN diodes are constructed from standard Gismo shapes. The beampipe is modeled as a tube with windows for pin diodes left out. The target support tube, through which the target is pushed upward into the beam during the accelerator ramp, is not included in the simulation setup. It cannot be modeled using predefined Gismo shapes. Fortunately it bears no importance on simulation problems considered so far. The PIN diodes have to be modeled as close as possible to the real setup (see Figure 2.5). Results of simulations of low energy δ-electrons are especially sensitive to the setup, because these particles are easily scattered. The active area of the PIN diodes is quadratic and covers 10×10 mm^2.

The PIN diode, as shown in Figure 2.5, is modeled from several **BOX** volumes. To improve tracking performance a new volume called **FASTBOX** was programmed by replacing the volume related Algorithms 2.5, 2.6 and 2.7 for box shapes. The underlying concept of the new algorithms is to convert particle position and direction into a local coordinate system relative to the **FASTBOX** volume. The origin of the local coordinate system is given by the center of the **FASTBOX** volume and the axes by the box axes. The equations of the original code computing the intersection of particle track and an infinite, planar surface involve several scalar products with the surface's normal vector. Since all planes defining the **FASTBOX** volume are aligned with the axes of the local coordinate system, the scalar product with a normal vector only selects one of the coordinate values of the other vector. All computations are then considerably simplified. Additionally, a simple check

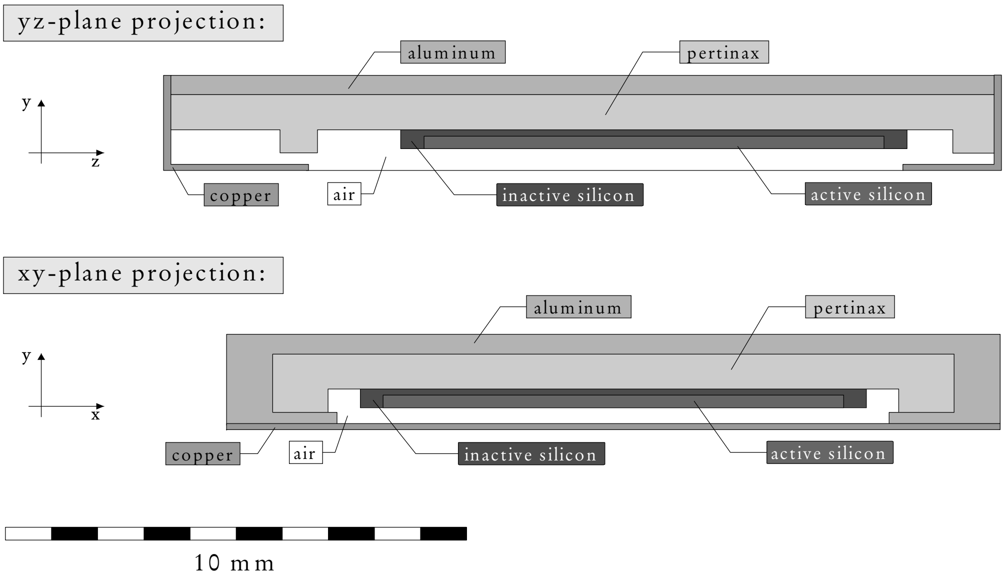

Figure 2.5: The model of the top PIN diode used in SIGI

of the sign of the coordinates of the particle direction allows restricting intersection calculation to only three of the six planes defining the box volume. Consider e.g. the planes x=-dx/2 and x=dx/2 with the box length dx along the local x-axis. A positive sign of the x-coordinate of the particle direction vector indicates for the *distance to leave* problem that only the plane x=dx/2 can have a valid intersection with the particle track. The simulation performance due to all these improvements increased up to a factor two for setups involving many hits in the PIN diodes. Simulations of the PIN diode efficiency, as presented in Chapter 3, gained most.

2.8.2 The Helix Layer: Programming a new Gismo Volume

The inner layer consists of four layers, each having a supporting tube onto which 160 scintillating fibers of circular cross section are glued [Wie94]. The fibers are helically wound around the supporting tube and read out in the backward region of the detector. The following simplifications are made, when modeling this setup:

- the readout hardware is not included in the simulation setup.
- the periodical setup of fibers and fiber supporting tubes is extrapolated to angles θ_{lab} = 72°..90°. This is possible, because the target support tube is not present in the simulation setup.
- the grooves, which are mill-cut into the supporting tubes, touch the fibers. In the real setup they are of trapezoidal cross section (Figure 2.7).

Modeling a helix layer of the EDDA detector poses two problems; how to program a helically wound shape of circular cross section, and how to model the fiber supporting tube. The following subsections illustrate the solution used in the SIGI program.

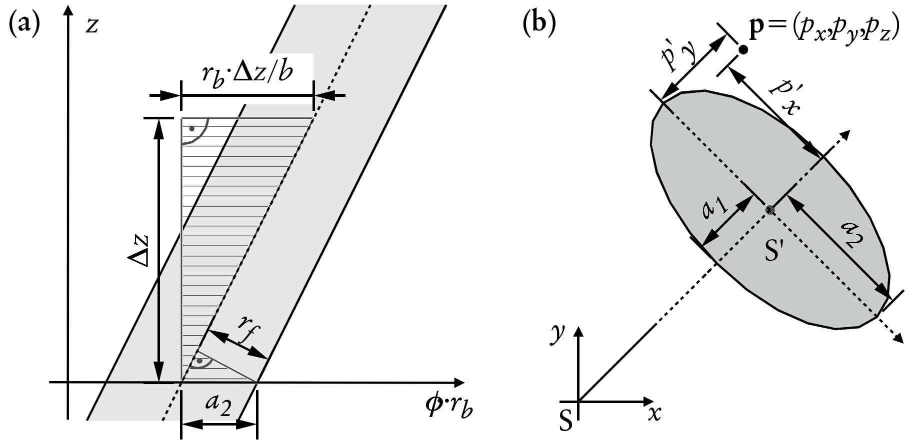

Figure 2.6: a) Cross section of helix fiber with cylinder of radius r_b. The hatched triangles are equivalent and allow calculating a_2. b) Approximation of cross section of fiber with plane $z=p_z$ by the dark gray elliptical area. The local coordinate system S' is defined by the semi-axes a_1, a_2 and the center of the ellipse.

Modeling a Fiber Layer

When programming a new Gismo volume, it is possible to provide new versions of Algorithms 2.5, 2.6 and 2.7 for the specific volume. This requires a good model of the shape to be defined. A fiber is usually defined as the the set of points whose distance from the fiber axis is smaller than the fiber radius r_f. This distance is measured in a plane perpendicular to the fiber axis. For a fiber axis, helically wound around a tube with constant radius r_b and axis identical to the z-axis, the following relations (in cylinder coordinates r,ϕ,z) hold:

$$r=r_b \ \wedge \ z=b \cdot \phi+\phi_0 \tag{2.8}$$

with: b: factor of proportion, identical for all fibers of one layer
ϕ_0: angle of fiber axis at z=0 (xy-plane)

Though this model is appropriate for arbitrary, helically wound fibers it is very difficult to solve even the *inside* problem. Fortunately the cross section of a typical fiber of the helix layers of the EDDA detector with a plane perpendicular to the z-axis is almost of elliptical shape. This is due to the fact that the fiber radius r_f is small compared to the helix radius r_b and the factor b is sufficiently large.

Using an elliptical shape as approximation for the correct cross section is certainly valid for the fibers of the helix layers, because the difference of approximation to correct cross section is small compared to normal production inaccuracies of the fibers. Some simple geometrical considerations (Figure 2.6 a) show the length a_1 and a_2 of the semi-axes of the ellipse to be:

$$a_1 = r_f \ \wedge \ a_2 = \sqrt{r_b^2 + b^2} \cdot \frac{r_f}{b} \tag{2.9}$$

The replacement for Algorithm 2.7 tests, whether a given point $\boldsymbol{p} = (p_x, p_y, p_z)$ is within the fiber volume, by first computing the elliptical approximation of the cross section of fiber and plane $z = p_z$. Then the coordinates p'_x and p'_y of $\boldsymbol{p}$ are determined relative to a local coordinate system S' with origin in the center of the ellipse and the axes of the ellipse according to Figure 2.6 b. The point $\boldsymbol{p}$ is outside the fiber volume, if the following value v is larger than the fiber radius r_f:

$$v = \sqrt{p'^2_x \cdot f^2 + p'^2_y} \tag{2.10}$$

with: f: quotient of a_1 over a_2

The replacement for Algorithm 2.6 calculates the distance to leave the fiber volume, by iterating the point $\boldsymbol{p}$ with fixed step length s_{fix} along the direction given by the particle momentum starting with the current particle position $\boldsymbol{p}_{current}$ inside the fiber volume. If the point $\boldsymbol{p}$ is outside the fiber volume after an iteration step the accumulated distance is returned. The equivalent method is used to calculate the distance to enter a fiber (replacing Algorithm 2.5). The fixed step length s_{fix} determines the accuracy of this algorithm and is typically chosen to be $50\,\mu m$. This allows a good approximation of the fiber geometry.

Modeling the Fiber Supporting Tubes

When a subregion is added to a region, the volume of the subregion is effectively removed from the volume of the parent region. Consequently, setting up the fibers of one helix layer as subregion of the fiber supporting tubes would be equivalent to mill-cutting the grooves into the fiber supporting tubes. This leaves no gap between fibers and supporting tube (Figure 2.7). Unfortunately, the fibers are only partially embedded in the supporting tube. They are also embedded in the surrounding region of air. So in the SIGI program they are set up as subregion of the support tube as well as the surrounding region of air. Obviously, this setup violates assumption 1 of Subsection 2.7.2. For this reason a modified version of Algorithm 2.3 had to be provided for the fiber region. Given a particle leaving a fiber, this new algorithm tests into which of the two parent regions the particle enters. Tracking is then continued in the correct parent.

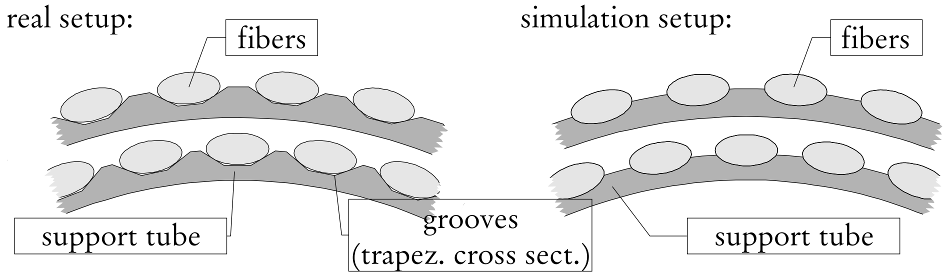

Figure 2.7: Setup of helix layers. For simplicity the figure is restricted to two layers and a smaller number of fibers.

2.8.3 The Outer Layer: Optimizing Gismo-Tracking

As mentioned earlier, Gismo treats all subregions of a given region alike. Thus, when calculating the intersection to the next geometry boundary, Gismo has to check each subregion for intersections with the particle track. This can be inefficient for periodical or simple geometries with many subregions. Two examples are the semi-ring and the bar layer of the EDDA detector.

Optimizing the Bar Layer Tracking

The bar layer consists of 32 scintillating bars, which are positioned inside a tube. This implies that Algorithm 2.3 has to check 32 subregions when calculating the distance to leave for the surrounding tube. A method restricting this large number of subregions to only those few, which could possibly be hit, would have a large impact on tracking performance. The first step in Algorithm 2.3 calculates the point in space, where the particle leaves the tube. Any bar which could possibly be hit, must overlap with the particle's track between its current position and this point of exit. Figure 2.8 illustrates this situation. In the example of Figure 2.8 only bars B_{30} and B_{31} are possible candidates for an intersection with the particle track beginning at $\boldsymbol{p}_{current}$. In general the current point $\boldsymbol{p}_{current}$ and the point of exit $\boldsymbol{p}_{exit}$ correspond to two angles $\phi_{current}$ and ϕ_{exit}, while the bar B_i covers an azimuthal interval from $\phi_{i,min}$ to $\phi_{i,max}$. Due to the periodic setup of the bars B_i the following relation holds:

$$\phi_{i+1,min}=\phi_{i,min}+\frac{2\pi}{32} \quad \wedge \quad \phi_{i+1,max}=\phi_{i,max}+\frac{2\pi}{32} \tag{2.11}$$

The following equations calculate the indices i_1 and i_2 of the bars, such that $[\phi_{current} \,..\, \phi_{exit}] \subseteq [\phi_{i1,min} \,..\, \phi_{i2,max}]$:

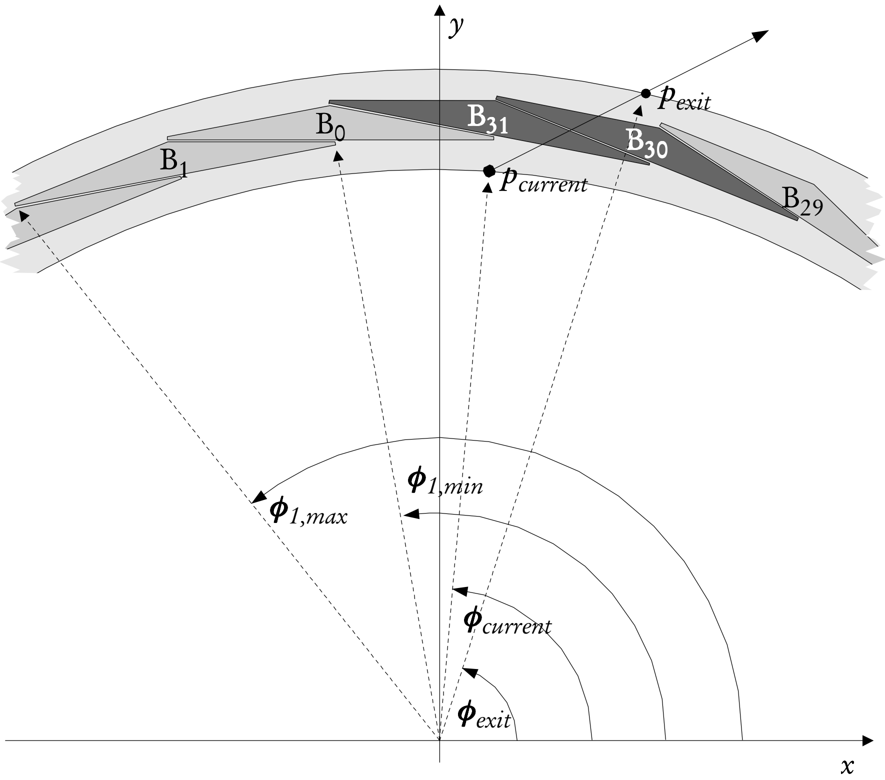

Figure 2.8: Cross section of bar layer with xy-plane. The light shaded tube is the parent region of the 32 scintillating bars of the outer layer. Tracking through the bar layer could be considerably improved, if the search for subregions in Algorithm 2.3, line 4 could be restricted to bars B_{30} and B_{31}. A method allowing this kind of optimization is presented in the text.

$$\begin{aligned} i_1 &= floor\left(\left(\phi_{current} - \phi_{0,min}\right) \cdot \frac{32}{2\pi}\right) \\ i_2 &= ceil\left(\left(\phi_{exit} - \phi_{0,max}\right) \cdot \frac{32}{2\pi}\right) \end{aligned} \tag{2.12}$$

with: *floor*(x): the function calculating the largest integer smaller than or equal to x
ceil(x): the function calculating the smallest integer larger than or equal to x

The search for intersections of the particle track with one of the 32 subregions can then be restricted to the scintillating bars B_{i1} to B_{i2}.

Optimizing the Ring Layer Tracking

Each half of the ring layer consists of 9 fiber semi-rings and 20 solid scintillator semi-rings. The 9 fiber semi-rings themselves consist of an inner and outer layer of 36 scintillating fibers of quadratic profile. When organized as three tubes, each containing 20 (or 36 respectively) semi-rings S_i with identical inner and outer radius, the layer of scintillator semi-rings and the inner and outer layer of fibers have a simple, uniform geometry. Figure 2.9 illustrates the situation for the layer of scintillating semi-rings of the EDDA detector. The identical approach can be applied to the scintillating fiber rings of the outer layer.

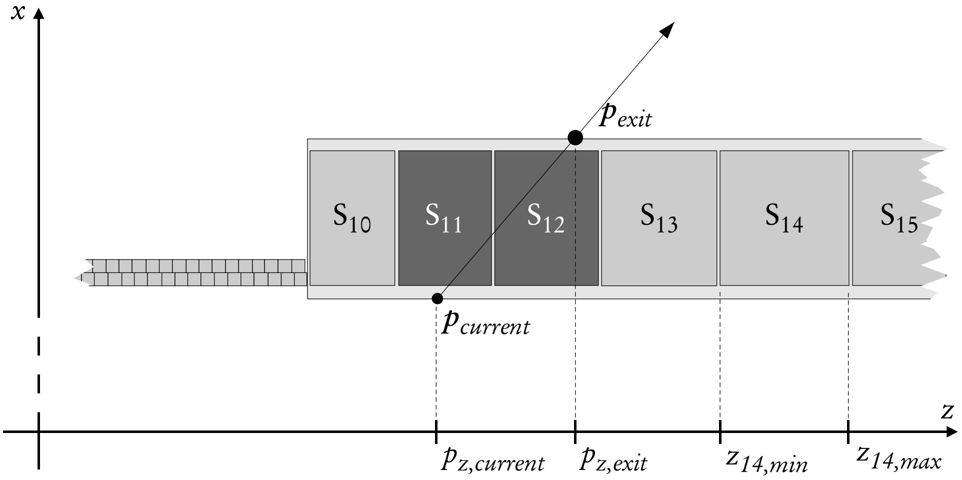

Figure 2.9: Cross section of semi-ring layer with xz-plane. The light shaded tube is set up as parent region of the 20 scintillating semi-rings of the outer layer. Again, tracking through the semi-ring layer could be considerably improved, if the search for subregions in Algorithm 2.3, line 4, could be restricted to the dark grey semi-rings S_{11} and S_{12}, which overlap with the particle track

Again, when the search for an intersection with a subregion (Algorithm 2.3, lines 3..6) can be restricted to those semi-rings S_i which could possibly be hit, tracking performance can be increased. The extent of a semi-ring S_i along the z-axis is given by the interval $[z_{i,min} .. z_{i,max}]$. Since the current point $\boldsymbol{p}_{current}$ with coordinates $(p_{x,current}, p_{y,current}, p_{z,current})$ and the point of exit $\boldsymbol{p}_{exit}$ with coordinates $(p_{x,exit}, p_{y,exit}, p_{z,exit})$ are known, only those semi-rings S_i, which overlap with $[p_{z,current} .. p_{z,exit}]$, can possibly be hit. The semi-rings used in the EDDA detector are not periodical along the z-axis. This implies that there is no simple formula, which allows determining the correct subset of semi-rings directly. Instead the indices i_{min} and i_{max} of semi-rings S_i satisfying the following condition are determined by a binary search algorithm [Wei95b]:

$$\begin{aligned} i_{min} &= min\left\{ i \,\middle|\, \left[z_{i,min} \dots z_{i,max} \right] \cap \left[p_{z,current} \dots p_{z,exit} \right] \neq \{\ \} \right\} \\ i_{max} &= max\left\{ i \,\middle|\, \left[z_{i,min} \dots z_{i,max} \right] \cap \left[p_{z,current} \dots p_{z,exit} \right] \neq \{\ \} \right\} \end{aligned} \tag{2.13}$$

with: $z_{i,min}$: minimum extent of semi-rings S_i in z
$z_{i,max}$: maximum extent of semi-rings S_i in z

The SIGI program replaces Algorithm 2.3 by a specific version for the ring elements of the outer layer, which takes advantage of the optimization described and considers only semi-rings S_{imin} to S_{imax} for the calculation of an intersection of the particle track with a subregion.

2.8.4 A Solution to the Touching Boundaries Problem

The following subsection describes a problem of the original Gismo code, which introduces tracking errors for specific detector setups. Unfortunately, the EDDA detector requires a setup, which leads to these problems. The solution in the framework of HepGismo and the SIGI program will be presented. This solution can easily be modified and applied to the concepts of the Gismo 2.0 toolkit. In fact, it was implemented in Gismo 2.0 in collaboration with T. Burnett and W. Atwood, two of the authors of the Gismo toolkit.

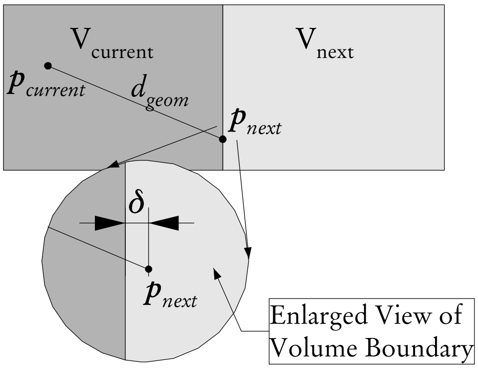

Figure 2.10: Numerical inaccuracies leading to the touching boundaries problem

The Touching Boundaries Problem

Consider the example of Figure 2.10. The particle is propagated by the calculated distance d_{geom}. Due to numerical inaccuracies the end point $\boldsymbol{p}_{next}$ of the step will not always be exactly on the given surface. Usually, this is of no particular consequence, unless the next volume V_{next} shares a part of its surface with the current volume $V_{current}$. Figure 2.10 shows an example, where $\boldsymbol{p}_{next}$ even lies *inside* the next volume V_{next}. Algorithm 2.5 then fails to find the correct solution, when calculating the distance to the next intersection with volume V_{next}. The correct solution is rejected, because it is a small, negative number. This type of problem will from now on be called the *touching boundaries problem*. It will always occur, when the geometry setup requires, that two volumes are positioned so close, that their surfaces touch. In fact, given a touching boundaries setup, there are several numerical inaccuracies which leave the particle slightly inside the next volume after performing a step. SIGI extends Gismo in such a way that this problem is solved.

Proposed Solution

The basic idea is to introduce the concept of the particle being *on surface* by defining a small distance ε around the mathematical surface. Whenever the starting point for the next step is within the distance ε of the mathematical surface of a volume, the distance to enter (or distance to leave) will be zero. This gives the calling code a hint that the correct volume has been found and no further volumes need to be considered. It also allows the particle to be propagated into the next region without any unnecessary energy loss or multiple scattering calculations.

The proposed solution involves altering the volume related Algorithms 2.5 and 2.6 as well as Algorithm 2.3, which must act upon the additional information conveyed by Algorithms 2.5 and 2.6.

Modifications to Algorithms 2.5 and 2.6

While checking for a point of intersection, Algorithms 2.5 and 2.6 calculate for every surface defining the volume the closest distance d_{near} of the current point to that surface (see line 2). This distance is checked against any already given step length restriction d_{max}. If the step length restriction d_{max} is smaller than the distance d_{near} (see line 3), the particle cannot reach the considered surface S_i within the given maximum step length of d_{max}. These lines of code were initially intended to avoid unnecessary and time-consuming calculations of intersections between particle track and surface S_i (see line 4). But by some slightly more elaborate code the distance d_{near} can easily be used to test the current point to be inside of, on or outside of the surface S_i:

$$\begin{aligned} &d_{near} \in \left[-\infty \ldots -\varepsilon\right], p_{current}\, \textit{is outside} \\ &d_{near} \in \left[-\varepsilon \ldots +\varepsilon\right], p_{current}\, \textit{is on surface} \\ &d_{near} \in \left[+\varepsilon \ldots +\infty\right], p_{current}\, \textit{is inside} \end{aligned} \tag{2.14}$$

with: ε: surface thickness, typically ~2.2 nm

If the current point $\boldsymbol{p}_{current}$ is on the infinite surface S_i examined, then the particle is really entering (or leaving), if two additional requirements are met:

Particle position	*Algorithm 2.6: calculate the distance to leave*	*Algorithm 2.5: calculate the distance to enter*
inside volume	Intersection within d_{max} exists: return $d_{intersect}$, else return `FLT_MIN`	return `FLT_MIN` (error condition)
on surface (entering volume)	Intersection within d_{max} exists: return $d_{intersect}$, else return `FLT_MIN`	return `0`
on surface (leaving volume)	return `0`	Intersection within d_{max} exists: return $d_{intersect}$, else return `FLT_MAX`
outside volume	return `FLT_MAX` (error condition)	Intersection within d_{max} exists: return $d_{intersect}$, else return `FLT_MAX`

Table 2.7: Return values of modified Algorithms 2.5 and 2.6. The distance d_{max} is a given step length restriction, the distance $d_{intersect}$ the distance to the next intersection of the particle track with the given volume surface

- the current point is inside the boundaries of the finite surface, which is embedded into S_i (see Subsection 2.7.4)
- the particle is entering (or leaving) the surface in the right direction. Given the particle's direction vector ***d*** and the surface normal ***n***, the particle is entering (or leaving), if the scalar product ***d·n*** is negative (or positive respectively)

When the particle is really entering (or leaving), no further surfaces need to be checked for intersections, and a *distance to enter* (or *distance to leave*) $d_{intersect}$ of zero is immediately returned.

Since the particle's position relative to each surface S_i (inside, on or outside) is already available in the modified versions of Algorithms 2.5 and 2.6, it is a simple task to combine these facts to give the position relative to the complete volume. If the position is within all surfaces S_i, it is also within the complete volume. If the position is outside of at least one surface S_i, it is outside of the volume. Computing this information has almost no impact on tracking performance, but is useful to detect tracking errors. Table 2.7 lists the different situations detected by the modified versions of Algorithms 2.5 and 2.6 and the values returned.

Modifications to Algorithm 2.3

Under certain circumstances the modified versions of Algorithms 2.5 and 2.6 return values, which are out of the range expected by any unmodified code calling these algorithms. The light shaded cells of Table 2.7 show the new return values introduced by the modified Algorithms 2.5 and 2.6. Algorithm 2.3, which calls these algorithms, had to be modified to react properly to these new return values.

The new return value `FLT_MIN` (or `FLT_MAX` respectively)[1] of the *distance-to-leave* (*distance-to-enter*) calculation indicates that, though the calling code assumes the particle's position to be inside (outside) of the considered volume, it is really not. This error condition only appears in erroneous setups, which have overlapping subregions or subregions not completely contained in their parent region. Such erroneous setups clearly violate the assumptions of Subsection 2.7.2. Algorithm 2.3 reacts to this error condition by warning the user. Then a search for the region, inside which the particle currently resides, is initiated. Tracking is continued in the region found.

If the *distance-to-leave* calculation for the parent region or the *distance-to-enter* calculation for one of the subregions returns zero, the modified version of Algorithm 2.3 returns immediately making the region found the current one.

Comparing Modified to Provided Algorithms

The modifications to the algorithms provided by Gismo involve a slightly more elaborate test. The test itself has only a small impact on the tracking performance, because it merely consists of three floating point comparisons. Only when the position of the particle relative to the considered volume is on surface or incorrect, the added code involves some lengthy calculations. For setups consisting partly of touching volumes this is compensated by the faster search in Algorithm 2.3. For erroneous setups on the other hand the advantage of detecting them proves more important than performance losses, which disappear when the error is corrected. Above all, setups, which rely heavily on volumes sharing a part of their surface (such as the EDDA detector setup), and use the original Gismo code cannot be simulated without introducing tracking errors, which leads to complete detector elements being missed during the tracking phase.

2.9 Digitizing Energy Losses: HISTO2YOD

The program HISTO2YOD reads the simulated data and converts it into 'detector signals'. The converted data as well as the original energy losses and timing information is written in TDAS-format for analysis with YODA, the EDDA analysis software. Details of this conversion are the topic of this section.

---

[1] `FLT_MIN`/`FLT_MAX` is the C++ symbolic name for the smallest/largest single precision number

2.9.1 The Ring Layer

The ring layer consists of two halves. Each half itself consists of an inner and outer row of 36 fiber semi-rings as well as 20 scintillator semi-rings. The energy loss ΔE of every single particle hit in a fiber or scintillator ring is individually converted into light and attenuated along the fiber or scintillator ring to give the attenuated light L_{att}. The light attenuation length λ can be individually chosen by the user for each fiber or scintillator ring:

$$L_{att} = c_1 \cdot \Delta E \cdot e^{-s/\lambda} \tag{2.15}$$

with:
L_{att}: attenuated light
s: arc length from energy deposit region to readout
λ: light attenuation length
c_1: conversion factor
ΔE: energy loss

To simulate the statistic effects of a photomultiplier converting the readout light into electric signals the resulting signal S_{PM} can be modified by a Gaussian distribution.

$$S_{PM} = c_2 \cdot \left(L_{att} + g\left(\sigma_0 \sqrt{L_{att}} \right) \right) \tag{2.16}$$

with:
g(σ): random number from Gaussian distribution
with standard deviation $\sigma = \sigma_0 \sqrt{L_{att}}$
c_2: conversion factor

The resulting signals S_{PM} are accumulated over all particle hits before further processing.

For the fiber rings the accumulated signals of an inner and an outer fiber are combined into one digital signal. These form a 36 bit hit-pattern. Additionally four inner and four outer fibers are combined into one ring by summing their signals. The accumulated signals are converted into digitized pulse heights simulating the behavior of an analog-to-digital converter (ADC). The conversion also clips signals, which overflow, and subtracts pedestals.

The accumulated signals of the scintillator semi-rings are simply converted into digitized pulse heights. Again the signals are clipped, if they overflow, and finally pedestals are subtracted.

The ring signals are discriminated and form the input of the simulated kinematic trigger.

2.9.2 The Bar Layer

The bar layer consists of 32 scintillating bars. Again the energy loss resulting from a single particle hit in a bar is individually converted into light. This light is split and attenuated along its path to the front and back readout region (see Equation (2.15)). All signals arriving at a readout region are accumulated. The accumulated signals of each readout are then converted into digitized pulse heights.

The accumulated bar signals are discriminated at each readout region. If either readout is above threshold it is input into the coplanar trigger.

The time of a particle hitting a bar is also recorded. The light transport to the readout region results in a delay, which is also considered. The first signal arriving at a readout region is routed onto one of eight simulated time-to-digital converters (TDCs). The time of arrival of the first signal in a TDC is converted into digitized time differences simulating the behavior of a TDC.

2.9.3 The Helix Layers

There are four helix layers each consisting of 160 helically wound fibers of round cross section. Each recorded energy loss is converted into light, which is attenuated along the fiber. To simulate the photomultiplier readout a Gaussian distribution can be applied. At readout the signals are accumulated. If the accumulated signal is above threshold for the given fiber, a hit is generated. The parameters for this conversion (light attenuation, distribution width, threshold) can be individually set for each fiber.

The fibers of two helix layers winding in the same direction are combined and numbered alternately. For the clockwise and anti-clockwise winding helix layers the number of the fibers hit are individually recorded and passed on to the analysis software.

2.9.4 The PIN Diodes

The energy loss per particle hit recorded in the PIN diodes is simply passed on to the analysis software. It is the responsibility of the analyzing program to use this information correctly. Chapter 3 shows an example how the energy losses are accumulated and analyzed to simulate the PIN diode efficiency.

Chapter 3

Efficiency of PIN Diodes

The SIGI simulation software is applied to the efficiency calculation of the PIN diode luminosity monitor. The details of the simulation method applied, especially the chosen configuration, and the analysis of the simulated data are presented. To motivate the method chosen, the concept of the EDDA luminosity monitors and some important equations are given.

3.1 EDDA Luminosity Monitors

The EDDA detector measures a count rate dN_p/dt of proton-proton elastic scattering events. To convert this count rate into cross sections the following equation is used:

$$\sigma_p = \frac{dN_p/dt}{L_p} \tag{3.1}$$

with: L_p: luminosity for pp-elastic scattering

Obviously the luminosity L_p of the pp-elastic scattering must be known to measure the cross section. It can be calculated using:

$$L_p = \frac{dN_{beam}}{dt} \cdot \frac{N_{protons}}{A_{target}} \tag{3.2}$$

with: dN_{beam}/dt: number of beam particles penetrating the target per second

N_{proton}/A_{target}: number of target protons per unit area

Unfortunately, none of the necessary parameters is precisely known. Especially the number of beam particles penetrating the target largely varies with beam momentum due to beam losses and changes in beam position and profile during an accelerator ramp. Two reasons make it impractical to derive the luminosity from the parameters of Equation (3.2):

- Only a small fraction of the beam and the target do overlap. The number of beam particles penetrating the target does not only depend on the number of particles circulating in the accelerator, but also on the precise shape, size and cross section of the fraction of the beam profile, which overlaps with the target.
- The number of target protons decreases over a long period of time due to radiation damage.

These reasons enforce luminosity monitoring at the EDDA detector. It is not sufficient to know the number of particles circulating in COSY to calculate the luminosity in the EDDA experiment. In the EDDA experiment two independent methods are used to monitor the luminosity:

- the secondary electron monitor (SEM)
- the PIN diodes

Both methods rely on the interaction of beam particles with atomic electrons in the target.

3.1.1 The Secondary Electron Monitor (SEM)

When the protons of the beam hit the target, they loose energy due to numerous interactions with atomic electrons (atomic excitation and ionization processes). For a fraction of the electrons the transferred kinetic energy allows them to reach the surface of the target and leave it. Passing through the target these primary δ-electrons knock out secondary electrons, a fraction of which also evaporates from the its surface. This leakage of electric charge results in an electric current. The target is covered with a thin layer of aluminum to conduct this current. The leakage current I_{SEM} is amplified and measured [Sch94]. It is proportional to the energy ΔE_{dep} deposited in the target:

$$I_{SEM} = C \cdot \Delta E_{dep} \tag{3.3}$$

The factor C can be determined theoretically [Ste57] but is afflicted with large uncertainties due to surface effects in the case of the EDDA detector [Mos94]. Nevertheless, the SEM signal I_{SEM} can be used for relative normalization of count rates at different beam momenta relative to a fixed beam momentum.

The deposited energy is linked to the number of beam particles passing through the target and the mean energy deposited per particle:

$$\Delta E_{dep} = N_{beam} \cdot \frac{dE}{dx}\left[T < T_{cut} \right] \cdot \Delta x \tag{3.4}$$

with: $dE/dx\ [T<T_{cut}]$: restricted energy loss rate
T: kinetic energy of the electron
T_{cut}: cutoff energy
Δx: target thickness

It should be mentioned that the mean energy *deposited* per particle is calculated from the *restricted* energy loss. The small dimension of the target allow energetic knock-on electrons to carry away part of the energy lost by the incident beam particle. This effect is taken into account by the restricted stopping power [PDG98]. For details of finding the correct cutoff energy T_{cut} = 20 keV the reader is referred to [Wel98]. Inserting this result into the luminosity Equation (3.2), the luminosity is proportional to the measured current I_{SEM} corrected by the restricted mean energy loss:

$$L_{SEM} = C_2 \cdot \frac{I_{SEM}}{dE/dx_{T<T_{cut}}} \tag{3.5}$$

with: L_{SEM}: luminosity of elastic proton-electron scattering measured with the SEM

This method does not allow absolute measurement of the luminosity. Only the relative change of luminosity with beam momentum during an accelerator ramp can be extracted. The factor C_2 is fixed by normalizing EDDA cross section data measured at p_{beam} = 1455 MeV/c with high precision cross section data from [Sim93] and [Sim96], measured at the same beam momentum.

3.1.2 PIN Diodes

As a result of beam protons interacting with atomic electrons in the target, δ-electrons are emitted from the target. The atomic electrons can be considered free, because their binding energy is small compared to the beam energy. The differential cross section of elastic electron-proton scattering is well known and given by the Rosenbluth cross section ([Käl64], Equation 8.31).

$$\frac{d}{dt}\sigma = \frac{(hc)^2 \alpha^2}{2\pi t^2} \cdot \frac{t^2 + 2st + 2\left(s - m_e^2 - m_p^2\right)^2}{s^2 + m_e^4 + m_p^4 - 2s\,m_e^2 - 2s\,m_p^2 - 2m_e^2 m_p^2} \tag{3.6}$$

with: $\alpha = 1/137$
$(hc)^2 = 15.372\ \mathrm{GeV}^2\ \mathrm{mb}$
s,t: Mandelstam variables of the proton-electron kinematics

Detecting δ-electrons emitted into a given solid angle Ω_0 allows calculating the luminosity L_{PIN} of the elastic electron-proton scattering:

$$L_{PIN} = N_e\left(\Omega_0\right) / \int_{\Omega_0} \frac{d\sigma}{d\Omega} \cdot d\Omega \tag{3.7}$$

with: $N_e(\Omega_0)$: number of electrons emitted into solid angle Ω_0
$d\sigma/d\Omega$: Rosenbluth cross section
L_{PIN}: luminosity of elastic proton-electron scattering measured with PIN diodes

The δ-electrons emitted from the target are detected by means of special semiconductor counters called PIN diodes. Their setup and mode of operation allows them to be used as detectors suitable for high count rates as experienced in the EDDA experiment [Sch94]. They are positioned into the beampipe in a special window of rectangular shape, where the thickness of the beampipe is reduced from 2 mm to 250 μm (Figure 1.4). The active area of the PIN diode of 10 × 10 mm^2 covers a solid angle of $\Omega_0 = 3.8 \cdot 10^{-3}$ sr, its center being at $\theta_{lab} = 39.6°$.

The δ-electrons emitted are considerably deflected by the aluminum between target and PIN diodes, especially at low beam energies. The number of electrons detected depends on the efficiency of the PIN diode setup:

$$\varepsilon\left(\Omega_0\right) = N_{det} / N_e\left(\Omega_0\right) \tag{3.8}$$

with: $N_e(\Omega_0)$: number of electrons emitted into solid angle Ω_0
N_{det}: number of electrons detected

Inserting this into Equation (3.7) we define the **luminosity per count** L_{count}:

$$\begin{aligned} L_{PIN} &= N_{det} \cdot L_{count} \\ L_{count} &= \frac{1}{\varepsilon\left(\Omega_0\right) \cdot \int_{\Omega_0} \frac{d\sigma}{d\Omega} \cdot d\Omega} \end{aligned} \tag{3.9}$$

This quantity has the advantage of being very convenient when converting the number of detected electrons N_{det} into the luminosity L_{PIN}. Unlike the efficiency ε the luminosity per count is also independent of the solid angle Ω_0, if the solid angle Ω_0 is chosen large enough to cover the active volume of the PIN diode completely. A Monte Carlo method to determine the PIN diode efficiency and the luminosity per count is given in Section 3.2.

Determining the Luminosity L_p

Both luminosity monitors, SEM and PIN diodes, measure the luminosity L_e of beam particles interacting with atomic electrons. Dividing Equation (3.2) by the equivalent equation for the electron luminosity L_e the proton luminosity L_p is given by:

$$L_p = \frac{N_p}{N_e} \cdot L_e \tag{3.10}$$

with: N_e : number of target electrons
N_p : number of free target protons

For the EDDA fiber target made of CH_2 the number of electrons per molecule is eight, the number of protons per molecule is two, resulting in a factor N_p/N_e of 0.25 for a fresh target. Due to radiation damage induced by the beam the number of target protons N_p decreases over a long period of time. For the short period of an acceleration ramp the number of target protons is practically constant.

Since the ratio N_p/N_e is not constant over a long period of time, the measured luminosity L_e cannot be used for an absolute normalization of pp-elastic angular distributions.

3.1.3 Conclusion

Both methods give a good *relative* normalization of angular distributions at different beam energies. Absolute normalization is achieved with reference to the high precision measurement of cross sections by Simon et al. [Sim96] at a beam momentum of p_{beam} = 1455 MeV/c.

3.2 Simulation Method

The following section describes the methods employed to simulate the efficiency of the inner, left and right PIN diode. Top and bottom PIN diode are not considered, since the top PIN diode was not mounted in April 1996 and the bottom PIN diode lacked the equipment for background separation. The section contains details of the generation of electrons in the target, the specific geometry setup and the way the simulated data are processed to calculate the luminosity per count.

3.2.1 Target Event Generator

The target event generator **`TwoParticles`** is initialized to generate electron-proton events with angular distributions corresponding to the Rosenbluth cross section (see Equation (3.6)). **`TwoParticles`** allows restricting the generated direction of electrons to an interval in θ and ϕ in the c.m. frame. The interval chosen should be as small as possible to avoid unnecessary tracking. A large solid angle also results in a smaller fraction of hits relative to the number of events generated and an increased statistical error. At the same time, care must be taken that a too restrictive solid angle does not cut into possible hits in the PIN diode examined. Finally, the method to minimize the solid angle chosen has to consider the slight variation of the c.m. frame with each event due to the phase space distribution of the beam particles.

Restricting the Solid Angle

For the inner PIN diode a special program called **`calcMinMax`** minimizes the solid angle. **`CalcMinMax`** assumes a straight, unperturbed flight of the electrons from

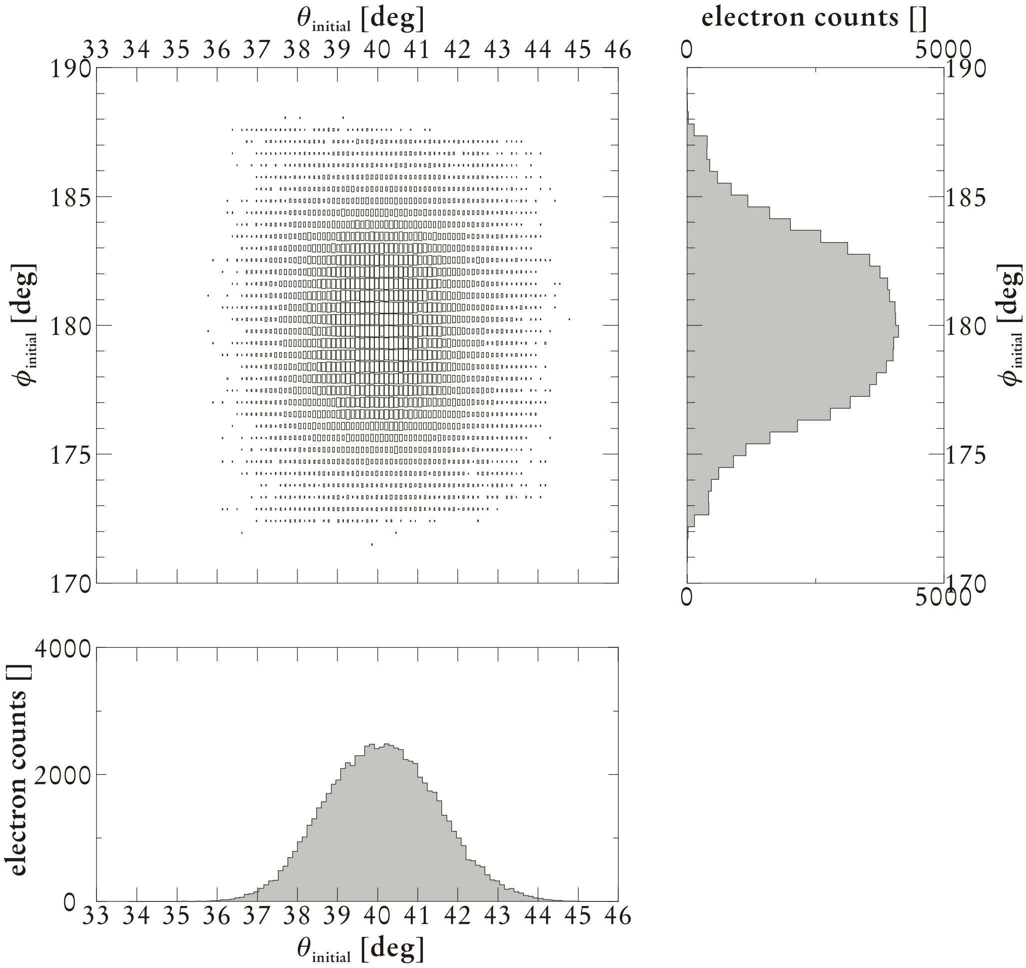

Figure 3.1: Typical coverage plot for the right PIN diode. Shown are the number of electron counts in the PIN diode versus the initial laboratory direction angles.

the target to the PIN diode examined. By varying all parameters given by the simulation problem at hand the minimum and maximum angles are determined. A safety margin of 40% is added to the resulting interval to allow for multiple scattering effects.

For the left and right PIN diodes the minimization problem is solved by performing an initial simulation with small statistics and large solid angle. The initial direction angles (θ_{lab},ϕ_{lab}) of electrons detected in the PIN diode are filled into a two-dimensional histogram. Figure 3.1 shows an example of such a *coverage plot*. From these plots the minimum and maximum angles are extracted manually. By projecting the histogram onto both axes two one-dimensional histograms are generated. Then the minimum and maximum histogram bins without counts are determined for both histograms. The lower or upper bin boundaries plus a safety margin of one degree are used to deduce the minimum or maximum angle respectively. In the example of Figure 3.1 the solid angle selected covers a range for θ_{lab} from 33.8° to 45.8° and for ϕ_{lab} from 170.8° to 189.2°.

Independent of the method used to select the solid angle, the coverage plot is studied again for every final efficiency simulation to guarantee a correct selection.

Selection of Monte Carlo Beam Properties

The luminosity per count of a particular PIN diode varies largely with different beam properties, such as beam position, width and direction. These properties have already been determined for all runs of previous run periods [Roh95]. The results are stored in special databases. To simulate the luminosity per count for a specific run of a run period, the position, width and direction of the beam can be automatically extracted from these databases. The random number generators are initialized accordingly. To enable systematic studies (see Chapter 4), the beam parameters can also be set explicitly.

3.2.2 Geometry Setup

Efficiency calculations are performed with a restricted setup, where only detector elements influencing the PIN diode efficiency are considered.

Due to their low kinetic energy, the electrons are submitted to large deflections from their original direction. A precise model of the PIN diode geometry itself and its position must be used (see Subsection 2.6.2). Especially the thickness of the active volume inside a PIN diode is essential for efficiency simulations.

Since the mounting of the inner PIN diode is not very accurate, the precise position of the inner PIN diode was determined from experimental data.

Restricted Geometry Setup

For the left and right PIN diodes, only the beampipe, the examined PIN diode and the corresponding beampipe window were included. In the geometry setup of the inner PIN diode the beampipe was not included, since it had no impact on the efficiency. Simulations with complete setups, especially including the outer layer, showed no significant effect on the efficiency within statistical limits, while the simulation time increased by a factor of two.

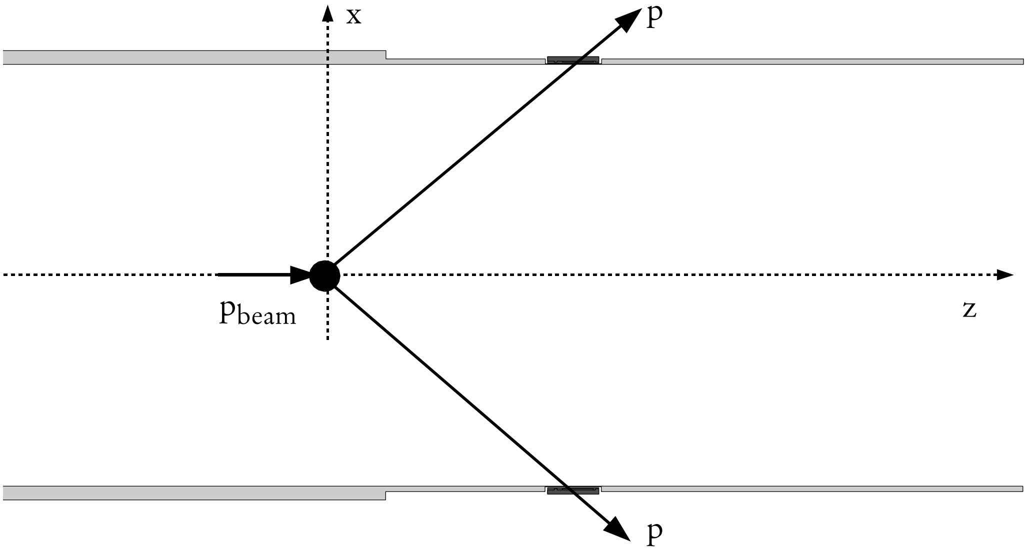

Figure 3.2: Setup for measuring the thickness of the active volume of the PIN diode detectors

Thickness of the Active PIN Diode Volume

The emitted protons of a pp-elastic scattering event have a defined kinetic energy, which solely depends on the beam momentum and scattering angle. The PIN diodes cover only a small interval in θ. Given a constant beam momentum the protons passing through the active volume of a PIN diode consequently have a narrowly defined kinetic energy. Given this kinetic energy and the deposited energy the thickness of the active volume can be calculated from the stopping power of protons.

To suppress other background processes two opposite PIN diodes are triggered in coincidence. Figure 3.2 shows the setup used to determine the thickness of the active volume of the PIN diodes. If two protons of a pp-elastic scattering event are detected in the final state, they fulfill the kinematic Relation (1.2). For the given position of $\theta_{lab1} = \theta_{lab2} = 40^\circ$ of two opposite PIN diodes this relation holds only for a beam momentum of 1455 MeV/c. Analyzing data taken at a beam momentum of 1455 MeV/c in April 1996, the thickness d of the active volume becomes [Hei95]:

$$d = (339 \pm 10)\,\mu\text{m} \tag{3.11}$$

In simulations performed for this thesis, the thickness d of 339 μm was used, unless noted otherwise.

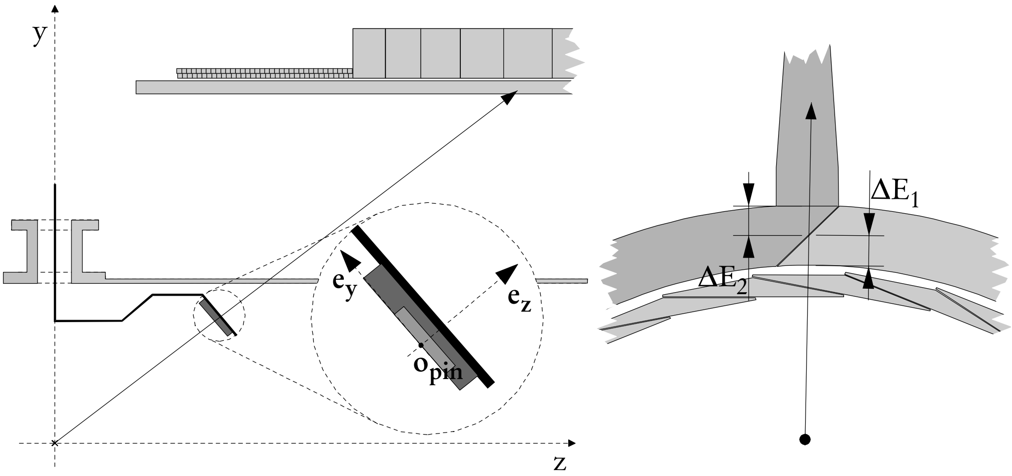

Figure 3.3: Setup for measuring the inner PIN diode position. Energy losses ΔE_1 and ΔE_2 are added before being used for θ-reconstruction

Position of the Inner PIN Diode

To determine the position of the inner PIN diode, pp-elastic events detected in the outer layer in coincidence with the inner PIN diode are analyzed [Die96]. Given a proton detected in the outer layer after passing through the inner diode, the emission angles can be reconstructed using the regular reconstruction algorithm with a slight modification. Since the proton is typically detected in the readout region of the semi-ring layer, the resulting signals are too small for the regular analysis of the light fraction output. To compensate this effect, the signals of two semi-rings are added before being used for reconstruction (see Figure 3.3).

The reconstructed angles θ and ϕ are filled into histograms (see Figure 3.4). Analyzing the flat top runs 752..771 measured in April 1996 at a beam momentum of 1455 MeV/c, the center of the inner PIN diode corresponds to elastic proton scattering at:

$$\begin{aligned} \theta &= 37.5^\circ \pm 0.5^\circ \\ \phi &= 91.0^\circ \pm 0.5^\circ \end{aligned} \tag{3.12}$$

The vertex position of the beam at (-2.3 mm, 0.5 mm, 0 mm) is given by the standard analysis of the beam properties. The z-position of the inner diode at 74.3 ± 0.5 mm is fixed by design and is relatively accurate (unlike the x- and y-

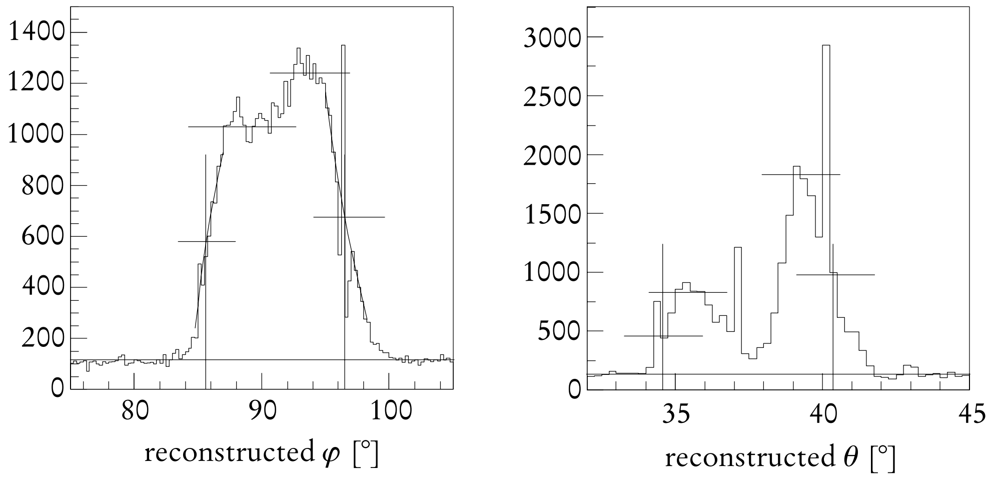

Figure 3.4: Histograms showing reconstructed angles of proton hits in the inner PIN diode. Crosses show position of FWHM used to determine the edge of the active PIN volume. The center of the active volume is calculated from the arithmetic mean. Reconstruction of events at $\theta = 37.5°$ is particularly difficult, because it corresponds to an angle between semi-rings S_{14} and S_{15} in the readout region of the semi-ring layer and threshold effects play a role.

position). The center of the active volume can then be deduced:

$$\begin{aligned} x &= -3.3 \pm 0.5\,\text{mm} \\ y &= 57.5 \pm 1.0\,\text{mm} \\ z &= 74.4 \pm 0.5\,\text{mm} \end{aligned} \tag{3.13}$$

Since construction and mode of operation of the inner PIN diode is essentially identical to the other PIN diodes, the thickness d of the active volume is assumed to be (339 ± 10) μm.

Special Setup of the Right PIN diode

In April 1996, the right PIN diode had to be replaced. The new PIN diode did not fit into the beampipe window due to mechanical problems. Therefore, it was mounted on top instead of inside the beampipe window, leaving a gap of 1.75 mm. Figure 3.5 shows this setup.

3.2.3 Material Data

The trigger thresholds of the PIN diodes correspond to an energy deposition of approximately 30 keV. To be counted as hit, the particle's energy deposition must be above threshold. The low energy tracking cuts should be set accordingly in order to achieve an appropriate accuracy. Though they are not directly correlated to the deposited energy, they determine to a certain extent the accuracy of the

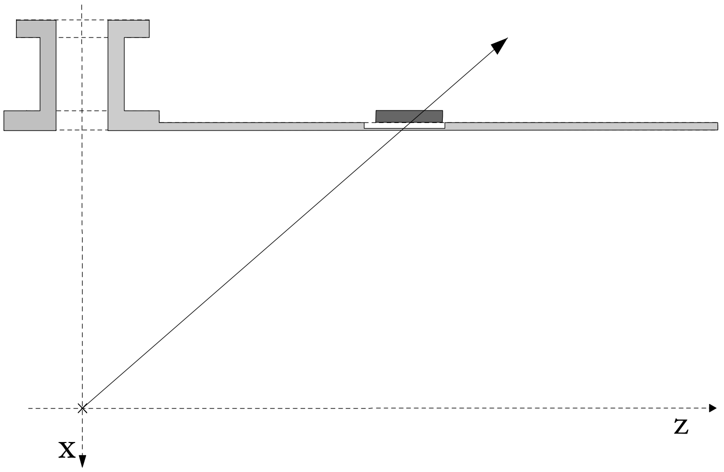

Figure 3.5: Setup of right PIN diode in April 1996.

energy loss calculation. Particles with energies below the low energy cut are considered as stopped and loose their kinetic energy without further tracking. This introduces errors, if their remaining energy allows them to leave the PIN diode, thus depositing only a fraction of their kinetic energy. To minimize this effect, kinetic energy cuts for electrons, positrons and photons were chosen to be:

$$T_{\text{cut,low}} = 10\ \text{keV} \tag{3.14}$$

The material data files of all materials employed in efficiency simulations were generated with the program PEGS4 using these tracking cuts.

3.2.4 Processing the Simulated Data

The simulation software writes the following data into the history tape format for each event simulated:

- position (x,y,z) and momentum (p_x,p_y,p_z) of the incident beam particle
- position (x,y,z) and momentum (p_x,p_y,p_z) of the generated electron
- all energy losses ΔE of the electron and its secondary particles in the active volume of the PIN diode

The program HISTO2YOD converts these data into TDAS format without any further processing. The analysis program YODA calculates some derived quantities and fills them into various histograms along with the original data. The histograms containing quantities related to beam properties are checked against the input parameters to ensure proper operation.

The position $\boldsymbol{o}_{el}$ and direction $\boldsymbol{d}_{el}$ of a generated electron define a straight line. Its intersection with the entry plane of the active PIN volume is determined and calculated relative to a PIN diode coordinate system with origin $\boldsymbol{o}_{pin}$ and unit vectors $\boldsymbol{e}_x$, $\boldsymbol{e}_y$ and $\boldsymbol{e}_z$ (see Figure 3.3):

$$\begin{aligned} x &= e_x \cdot \left(o_{el} + \lambda \cdot d_{el} - o_{pin}\right) \\ y &= e_y \cdot \left(o_{el} + \lambda \cdot d_{el} - o_{pin}\right) \end{aligned} \tag{3.15}$$

with:

$$\lambda = \frac{\left(o_{pin} - o_{el}\right) \cdot e_z}{d_{el} \cdot e_z}$$

If this intersection point lies within the active PIN diode volume, the event is counted as **geometrical hit**.

All energy losses of one event which occur in the active volume are accumulated into $\Sigma\Delta E_i$. If any energy loss occurred in the active volume, the event is counted as **physical hit**. If the accumulated energy loss $\Sigma\Delta E_i$ is above threshold, the event is said to be a **detected hit**. Nevertheless, thresholds are ignored at this stage of the analysis. This allows studying the influence of thresholds on efficiencies. For all physical hits, the accumulated energy loss $\Sigma\Delta E_i$ as well as the initial direction angles (θ,ϕ) of the generated electron are statistically analyzed. The histogram of physical hit counts versus initial direction angles allows confirming that the PIN diodes were properly illuminated with generated electrons (coverage plot, see Subsection 3.2.1).

3.2.5 Analysis of the Energy Loss Spectrum

In the offline analysis of measured spectra additional cuts are applied to discriminate baseline counts. The method to determine these thresholds is described in [Hei95]. One typical source of baseline counts in the spectrum of a PIN diode is due to the readout of the associated ADC, when a hit in another PIN diode triggered the readout. This random process is extremely difficult to simulate. Fortunately, simulating baseline counts is unnecessary. It is sufficient to compare energy loss spectra above the thresholds given. For simulation purposes the thresholds from the offline analysis of measured data must be applied. The following thresholds of April 1996 are used throughout the rest of this thesis, unless noted otherwise:

$$\begin{aligned} E_{thresh,left} &= 86\text{ keV} \\ E_{thresh,right} &= 82\text{ keV} \\ E_{thresh,inner} &= 144\text{ keV} \end{aligned} \tag{3.16}$$

The simulated efficiency $\varepsilon(\Omega_{sim})$ is extracted from the simulated energy loss spectra by integrating the channel contents $h_{i,simul}$ above the threshold E_{thresh}:

$$\varepsilon\left(\Omega_{sim}\right)=\frac{1}{N_{events}}\cdot\int_{E_{thresh}}^{E_{max}}\mathrm{h}\left(E\right)dE \tag{3.17}$$

with: N_{events}: number of simulated events
$\mathrm{h}(E) = \{ h_{i,simul}/\Delta E$, for $E_{i-1} \leq E < E_i$ (step function with values $h_{i,simul}/\Delta E$ in the interval $[E_{i-1}..E_i[$)
ΔE: bin width of energy loss channel
E_{max}: upper bin limit of largest energy loss channel
Ω_{sim}: the solid angle

The number of detected electrons above threshold is binomially distributed. The error of the efficiency is calculated accordingly [Wei97]. The resulting efficiency ε and the Rosenbluth cross section (integrated over the solid angle Ω_{sim}) are used to compute the luminosity per count L_{count} from Equation (3.9).

Signal Noise and the Energy Loss Spectrum

It is worthwhile mentioning that the spectrum used for efficiency calculations has not been convoluted with a gaussian to model signal noise. The following argument will show that modeling signal noise would systematically underestimate the number of counts above threshold.

Including the effects of signal noise in the simulated spectrum extends the spectrum to lower energies, resulting in less counts above threshold. This was proven for every beam momentum by convoluting the spectrum with a gaussian of increasing width and integrating counts above threshold.

In the measured spectra this effect is, to a certain extent, counterbalanced by baseline counts, which are seen above threshold due to signal noise. Since the threshold is chosen in the minimum of the peak of baseline counts and the physical spectrum, the number of counts, which are seen below threshold due to signal noise, is of the same order as the number of baseline counts seen above threshold. Unfortunately, it is not feasible to include baseline counts in the simulated spectrum due to their statistical nature.

Consequently, for efficiency calculations using the unmodified spectrum and ignoring the effects of signal noise provides a better estimate of the real efficiency than a convoluted spectrum, which includes noise effects, but ignores baseline counts.

On the other hand, when comparing measured and simulated spectra, signal noise effects have to be taken into account (see Subsection 3.3.2and Appendix A).

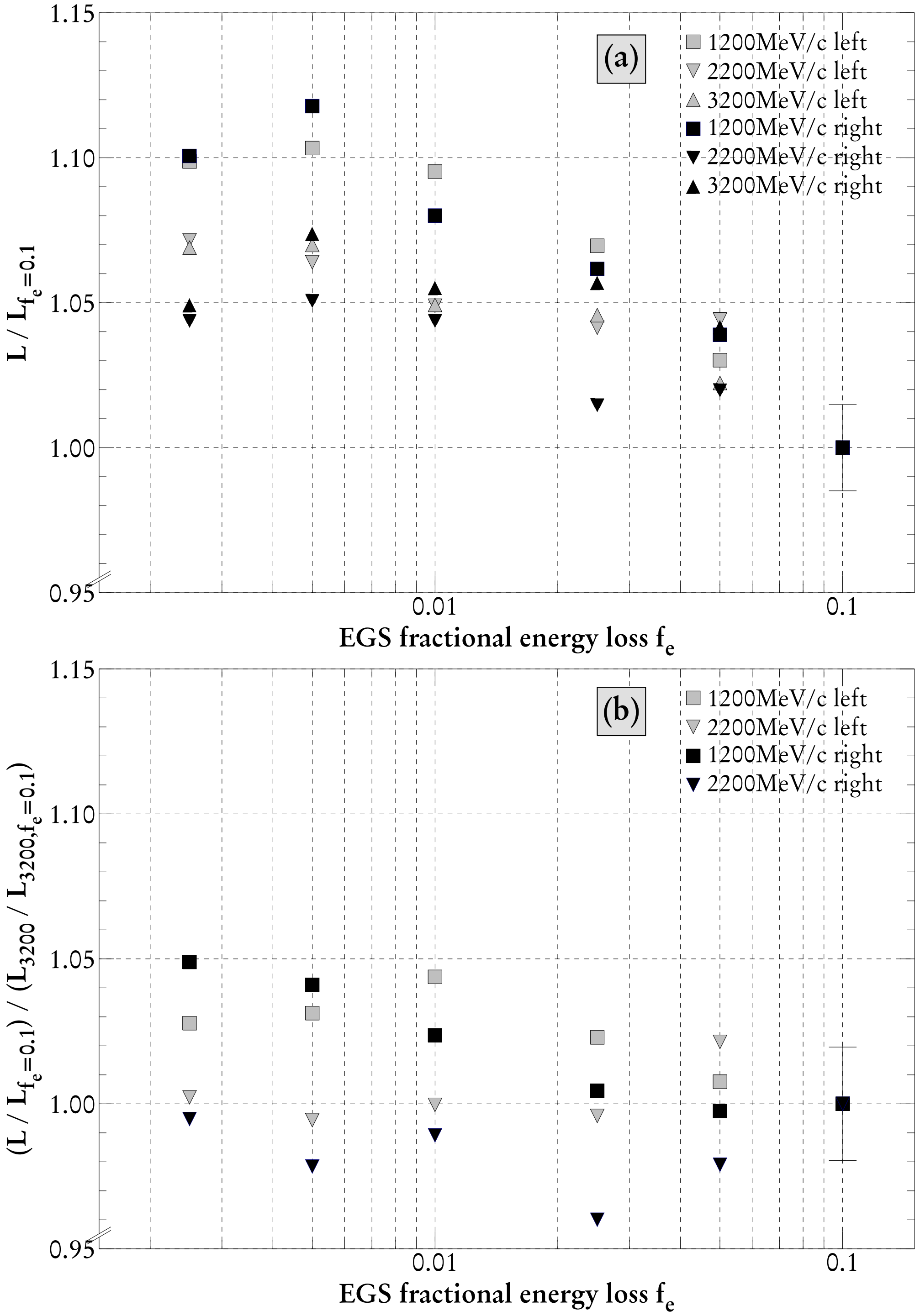

Figure 3.6: Systematic study of fractional energy loss parameter f_e. Shown is the luminosity per count L versus the fractional energy loss: a) relative to f_e=0.1 b) relative to f_e=0.1 and L(3200 MeV/c). For simplicity error bars are plotted at f_e=0.1 only.

3.3 Cross Checks

This section describes important cross checks, which were performed to insure proper operation of the simulation software.

3.3.1 The Fractional Energy Loss Parameter

As mentioned earlier, typical δ-electron energies in efficiency simulations are close to the limits of validity of the EGS4 shower code. When comparing experimental with simulated data, it turns out that the fractional energy loss parameter has to be set with extreme care to give good results.

The fractional energy loss f_e determines the maximum energy loss of an electron or positron per tracking step in terms of its kinetic energy. The fractional energy loss indirectly restricts the maximum step length an electron or positron is allowed to take during particle tracking. Obviously, a smaller fractional energy loss increases computation time.

A systematic study to find the correct fractional energy loss f_e was performed [Roh96]. For three different beam momenta (1200, 2200 and 3200 MeV/c) f_e was varied over six values from 0.25 % to 10 %. The results are shown in Figure 3.6. For simplicity error limits are shown at $f_e = 10\%$ only. To permit all data to be presented in one plot, data are scaled to their value at $f_e = 10\%$. Since only relative changes with the fractional energy loss f_e are of importance, the scaling of the data has no impact on the questions studied.

Based on the results presented in Figure 3.6, the fractional energy loss f_e was chosen to be 0.5 % for all efficiency calculation [Roh96]. This choice is sufficiently accurate, while being acceptable as far as computation time is concerned. It is in accordance with recommendations of the authors of EGS4 [Nel85c].

3.3.2 Comparing Simulated to Measured Energy Loss Spectra

The comparison of simulated and measured energy loss spectra is another important cross check. Figure 3.7 shows a typical example: simulated and measured energy loss spectra of the right PIN diode versus beam momentum for four beam momenta. The measured data were taken during acceleration cycles of runs 965..994 and runs 997..1001 of April 1996. Figure 3.8 shows the same spectra as two-dimensional plot for all beam momenta.

The simulated spectrum accurately reproduces the features of the data. For low beam momenta the δ-electrons are slow and can be stopped with a certain probability within the PIN diode. The stop peak is seen very clearly for beam momenta below 1500 MeV/c. With increasing beam momentum and increasing kinetic energy of the δ-electrons, the stop peak vanishes and the typical Landau distribution appears. The Landau distribution is due to high energy electrons passing through the thin active volume of the PIN diode without stopping.

For low beam momenta and the left and right PIN diode setup, the stop peak is relatively broad due to energy loss straggling and multiple scattering in the beampipe window. The stop peak seen in the inner diode is only broadened by the incident kinetic energy distribution of the δ-electrons and thus relatively narrow. With increasing beam momentum and increasing kinetic energy of electrons detected in the PIN diodes, the mean value of the stop peak shifts to higher energy losses. To demonstrate this effect, Figure 3.8 shows the kinetic energy of a δ-electron emitted from the target at an laboratory angle θ_{lab} of 40° as a function

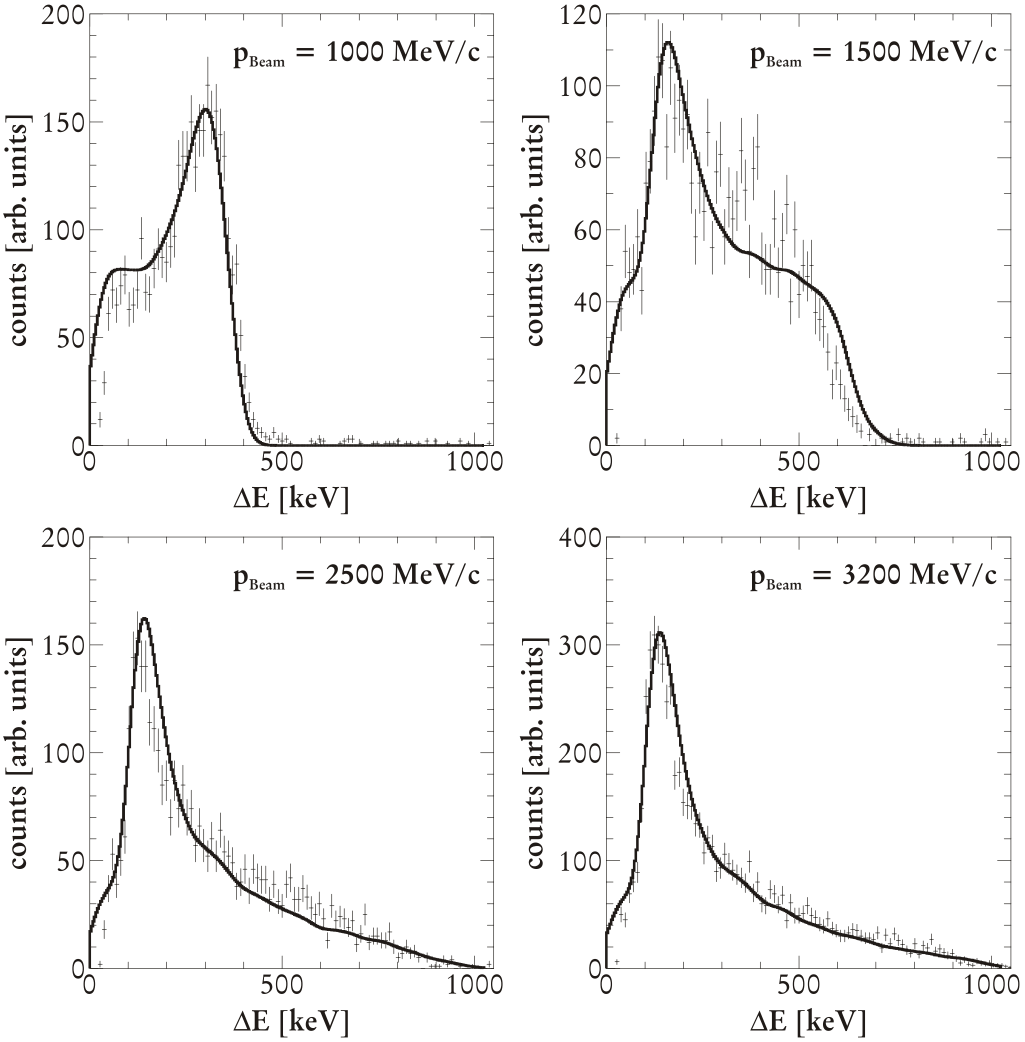

Figure 3.7: Energy loss spectra of δ-electrons at 4 typical beam momenta. Continuous lines shows simulated spectra; error bars show data taken with the right PIN diode during runs 965..994 and 997..1001 of April 1996.

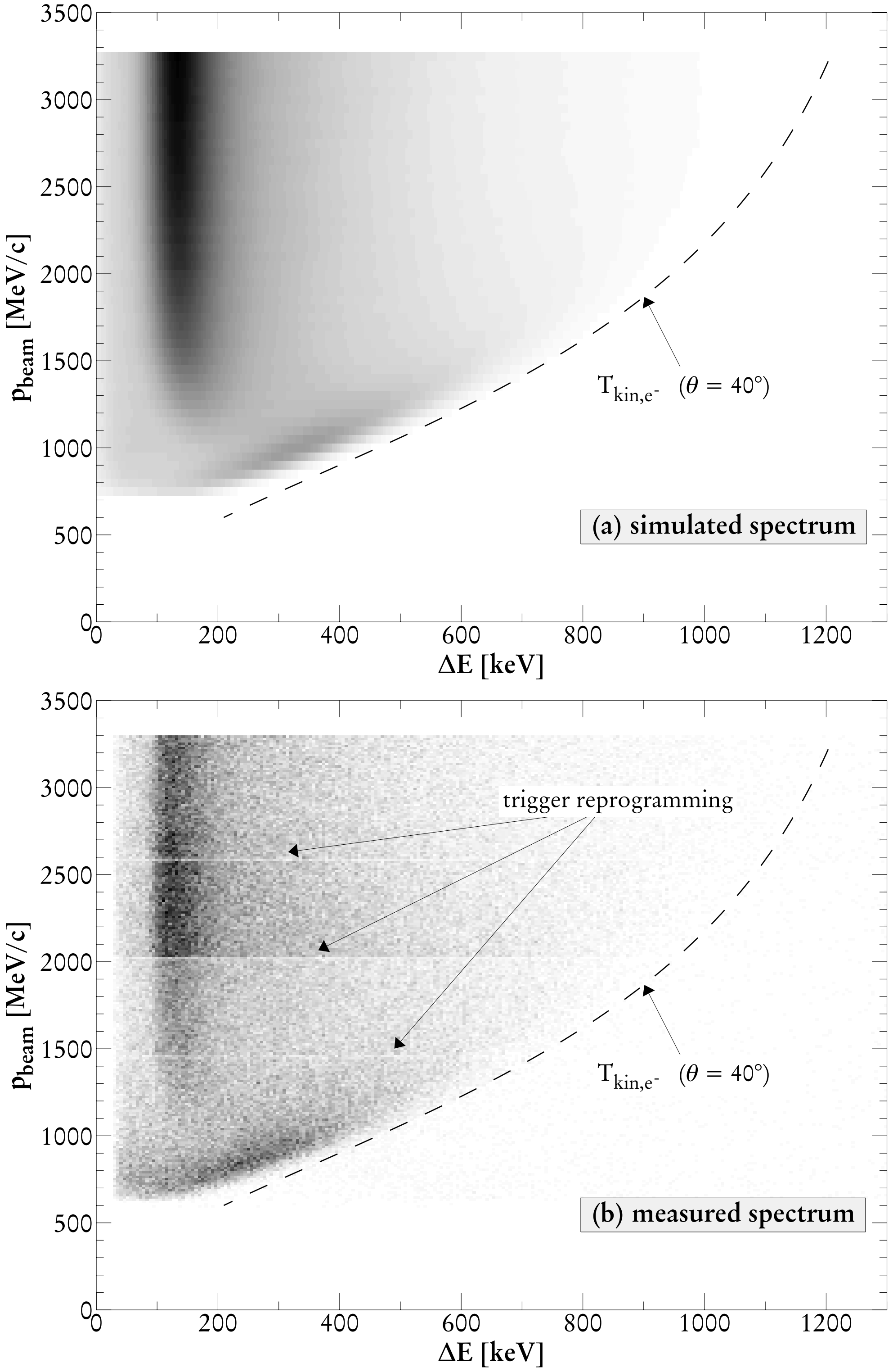

Figure 3.8: Typical energy loss spectrum of δ-electrons in the right PIN diode during an accelerator cycle for the beam-setup of run #965 of April 1996: a) simulated spectrum b) measured spectrum.

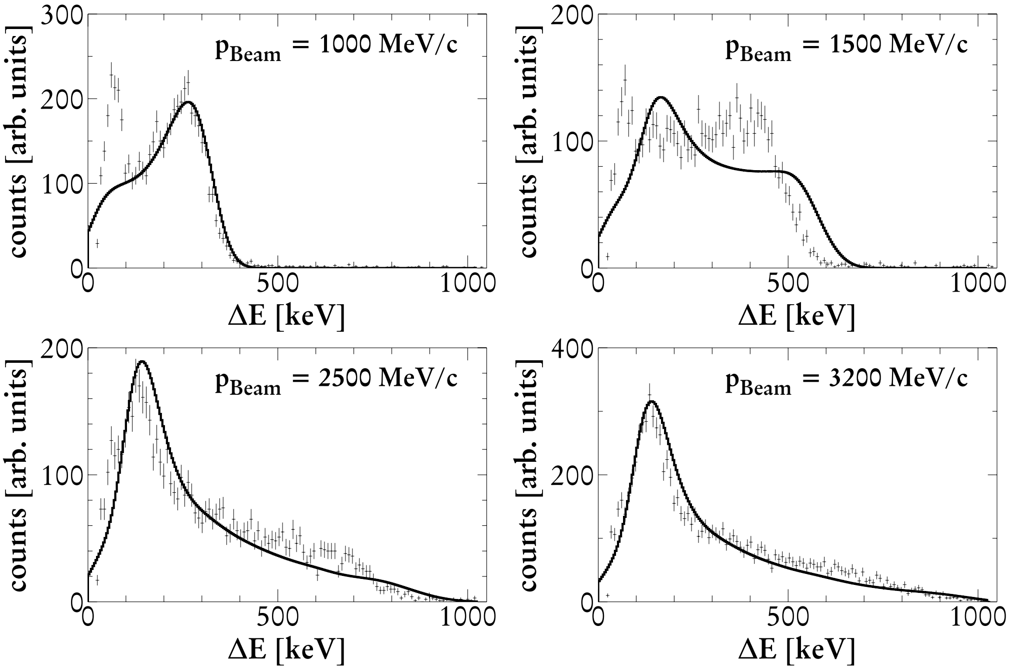

Figure 3.9: Energy loss spectra of δ-electrons at 4 typical beam momenta for the left PIN diode. Continuous lines shows simulated spectra; error bars show data taken during runs 965..994 and 997..1001 of April 1996.

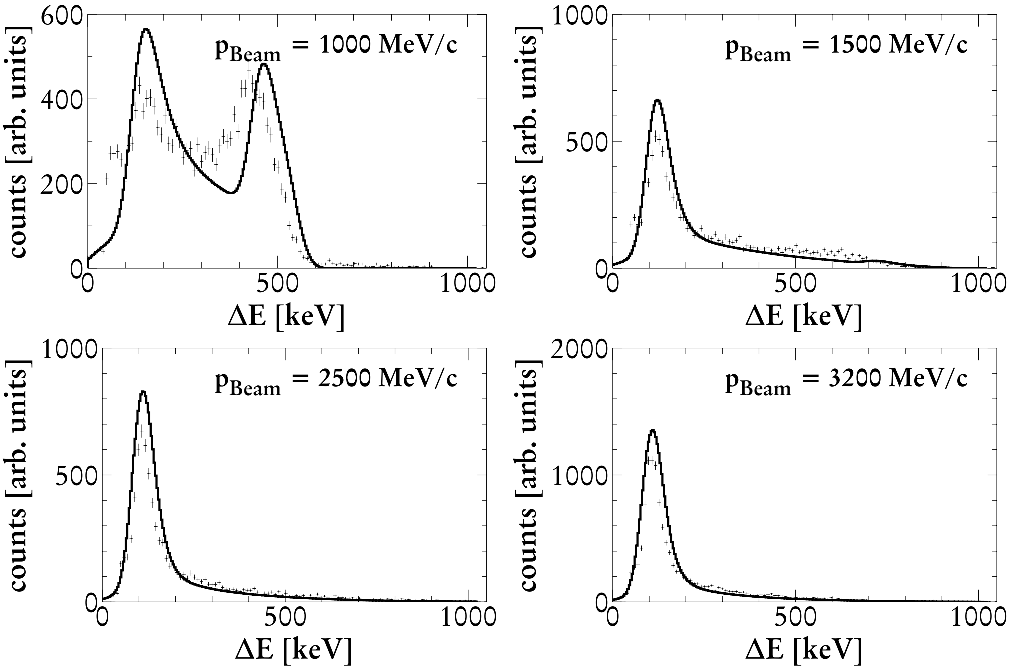

Figure 3.10: Energy loss spectra of δ-electrons at 4 typical beam momenta for the inner PIN diode. Continuous lines shows simulated spectra; error bars show data taken during runs 965..994 and 997..1001 of April 1996.

of the beam momentum. Above a beam momentum of 1500 MeV/c, stopping of δ-electrons in the PIN diodes becomes negligible.

For completeness, Figure 3.9 and 3.10 present simulated and measured energy loss spectra of the left and inner PIN diode versus beam momentum for four beam momenta.

The measured spectra of the left PIN diode include an additional noise peak below an energy loss of 100 keV, which is not seen in the simulated spectrum. This extra peak is a strong indication of a hardware problem, especially because it was not seen in previous data taking periods. Chapter 5 includes more details on this specific problem. For a beam momentum of 1500 MeV/c, the typical Landau distribution and the stop peak in the measured spectrum overlap and the two distributions cannot be separated. In the simulated spectrum the peak of the Landau distribution is clearly visible. This effect is typical for a small deviation of the simulated from the real geometry of the PIN diodes, beam and beampipe. The form of the spectrum of the left PIN diode at 1500 MeV/c is especially sensitive to small offsets of the PIN diode position relative to the beam and target. These type of systematic errors are studied in great detail in the next chapter.

For the inner PIN diode and a beam momentum of 1000 MeV/c, the peak of the Landau distribution and the stop peak are more pronounced in the simulated than in the measured spectrum. This indicates that the measured spectrum includes counts of other particles than δ-electrons. The inner PIN diode is mounted inside the beampipe. Due to this position it is sensitive to background not emitted from the target. This type of background cannot be corrected. In Chapter 5 this effect is discussed in detail. In addition, other evidence for this background will be presented.

Chapter 4

Simulation Method and Errors

This chapter will show that, when combining results of the left and right PIN diode, the simulation software allows to determine the relative luminosity (change in luminosity with beam momentum) with a systematic error of less than 3.0%, for the major part of the momentum range even less than 0.9%. For the inner PIN diode the systematic error is even less than 0.5%. To achieve this goal, possible sources of errors are listed and their influence on the luminosity measurement with the PIN diodes is examined. Using these results, the systematic error of this method to normalize pp-elastic count rates is estimated.

4.1 General Considerations

Studying the possible sources of error it is important to realize that both luminosity monitors, secondary electron monitor SEM and the PIN diodes, are only used for relative normalization of cross section data with respect to a fixed beam momentum. In addition, the error analysis has to take into account that typically the arithmetic mean of the luminosity measurements with the left and right PIN diode is used for normalization, which results in a considerable reduction of the overall systematic uncertainty.

4.1.1 Normalization of Cross Section Data

The EDDA detector was designed to provide simultaneous measurements of differential cross sections over a large range of scattering angles and beam momenta. This method provides a highly accurate relative normalization of the results. In order to calculate absolute cross sections, EDDA data are normalized at a fixed beam momentum to published data from experiments with high *absolute* normalization accuracy. To this end, the angular distribution measured by Simon et al. [Sim93, Sim96] at the fixed beam momentum of 1455 MeV/c was chosen for the EDDA experiment [Alb97].

Due to way the data are normalized, it is important to distinguish between errors of the absolute normalization and errors of the relative normalization. The error of the absolute normalization, i.e. the error of the overall normalization factor, contributes for all beam momenta simultaneously. Errors of the relative normalization apply only to the measurement at a specific beam momentum. In order to determine for each quantity, which class of errors it contributes to, all quantities used to calculate the luminosity measured with PIN diodes are presented in this subsection. Unfortunately, for the luminosity per count L_{count}, which is the relevant quantity determined by simulations, this classification is not straightforward. Certain systematic errors (due to *momentum independent* sources of error, which are defined later) simultaneously affect the luminosity per count at the beam momentum studied $L_{count}(p)$ and at the normalization momentum $L_{count}(1455)$; the systematic errors for the two luminosities per count are correlated. To study these systematic errors, it is convenient to introduce the ratio Q:

$$Q = Q(p) = \frac{L_{count}(p)}{L_{count}(1455)} \tag{4.1}$$

with: $L_{count}(p)$: luminosity per count at beam momentum p
$L_{count}(1455)$: luminosity per count at 1455 MeV/c

In addition, the ratio Q serves the purpose of combining all simulation related quantities into one quantity. Studying the sources of error of the ratio Q allows determining all simulation related errors.

4.1.2 Determining the Luminosity with PIN Diodes

This subsection presents in detail all quantities needed to calculate the luminosity $L(p)$ for pp-elastic scattering using PIN diodes as luminosity monitors and corresponding simulations to determine the luminosity per count L_{count}.

For a given beam momentum p, the following equation is used to calculate the pp-elastic scattering luminosity L from the luminosity per count L_{count} and the electron count rate N_e in a PIN diode:

$$L(p) = C_{norm} \cdot L_{count}(p) \cdot N_e(p) \tag{4.2}$$

with: C_{norm}: normalization factor
p: beam momentum

From the cross section data measured by Simon et al. the luminosity $L(1455)$ at a beam momentum of 1455 MeV/c is determined by the following equation:

$$L(1455) = \frac{N_{pp}(1455)}{\sigma_{Simon}(1455)} \tag{4.3}$$

with: $N_{pp}(1455)$: count rate of pp-elastic events in the angular range 39° < θ_{cm} < 89° [Wel98]
$\sigma_{Simon}(1455)$: integrated cross section from Simon et al. [Sim93]

Evaluating Equation (4.2) at a beam momentum of 1455 MeV/c and inserting the result into Equation (4.3), the normalization factor C_{norm} is given by:

$$C_{norm} = \frac{1}{L_{count}(1455) \cdot N_e(1455)} \cdot \frac{N_{pp}(1455)}{\sigma_{Simon}(1455)} \tag{4.4}$$

with: $L_{count}(1455)$: luminosity per count determined at a beam momentum of 1455 MeV/c
$N_e(1455)$: count rate of electrons detected at a beam momentum of 1455 MeV/c

This result can be inserted into Equation (4.2):

$$L = \frac{N_{pp}(1455)}{\sigma_{Simon}(1455)} \cdot \frac{N_e(p)}{N_e(1455)} \cdot Q(p) \tag{4.5}$$

We note that the errors of the different factors are statistically independent. Assuming gaussian distributions, the error ΔL of the luminosity measurement with PIN diodes can be determined from the rules of error propagation:

$$\begin{aligned}\left(\frac{\Delta L}{L}\right)^2 = {} & \left(\frac{\Delta N_{pp}(1455)}{N_{pp}(1455)}\right)^2 + \left(\frac{\Delta \sigma_{Simon}(1455)}{\sigma_{Simon}(1455)}\right)^2 + \left(\frac{\Delta N_e(1455)}{N_e(1455)}\right)^2 \\ & + \left(\frac{\Delta N_e(p)}{N_e(p)}\right)^2 + \left(\frac{\Delta Q\ (p)}{Q\ (p)}\right)^2\end{aligned} \tag{4.6}$$

with: $\Delta N_e(p)$: error of electron count rate $N_e(p)$
$\Delta N_e(1455)$: error of electron count rate $N_e(1455)$
$\Delta N_{pp}(1455)$: error of proton count rate
$\Delta\sigma_{Simon}(1455)$: statistical and systematic errors of the cross section measurement by [Sim93, Sim96]
$\Delta Q(p)$: error of $Q(p) = L_{count}(p) \,/\, L_{count}(1455)$

The following errors contribute to the error of the absolute normalization, i.e. the error of the overall normalization constant C_{norm}:

- the statistical error $\Delta N_e(1455)$ of the electron count rate at a beam momentum of 1455 MeV/c
- the statistical error $\Delta N_{pp}(1455)$ of the proton count rate
- the statistical and systematic errors $\Delta\sigma_{Simon}(1455)$ of the cross section measurement by Simon et al. [Sim93, Sim96]

The following error contributes to the errors of the relative normalization. It depends on the beam momentum p:

- the statistical error $\Delta N_e(p)$ of the electron count rate at the beam momentum studied

The simulation related errors of the ratio Q contribute to both classes of errors and will be studied in the next subsection.

4.1.3 Simulation Related Errors of the Luminosity

The ratio Q is calculated from the luminosities per count L_p and L_{1455}[1], which are individually simulated. This subsection presents the different statistical and systematic errors to the simulation of the luminosity. Especially correlations of errors have to be carefully taken into account.

Statistical Errors

The statistical errors of the luminosities per count L_p and L_{1455} are determined by two independent simulations. Consequently, the statistical errors of L_p and L_{1455} are uncorrelated and calculated individually according to Subsection 3.2.5. The statistical error of L_{1455} contributes to the error of the absolute normalization while the statistical errors of L_p add to the errors of the relative normalization.

For the simulations outlined in Chapter 5 with a statistic of 800000 simulated events, typical statistical errors of the luminosity per count L_p or L_{1455} vary little with beam momentum and are less than 0.5 % for the left and right PIN diode and less than 0.24 % for the inner PIN diode. In principle, these errors can be made arbitrarily small by increasing the number of simulated events.

---

[1] To simplify matters for the following considerations, the functional dependence of the ratio Q and other quantities on the beam momentum p will no longer be expressed explicitly. Especially, the luminosities per count $L_{count}(p)$ and $L_{count}(1455)$ will be abbreviated to L_p and L_{1455}.

Systematic Errors

The ratio Q is not only a function of the beam momentum p, but also depends on several input parameters of the simulation, especially the exact geometry and the relative positions of beam, target and PIN diodes. Each input parameter of the simulation can be afflicted with errors. The errors of the input parameters are systematic errors. The rest of this chapter will present an analysis of the different systematic errors of Q. To evaluate the influence of a specific source of error on the ratio Q, two important cases have to be distinguished:

- a given parameter a with error Δa takes on identical values for all beam momenta during an acceleration cycle. Hence, the systematic errors of the luminosities per count L_p and L_{1455} are correlated. These sources of error will be named *momentum independent*:

  $$Q(.., a, ..) = L_p(.., a, ..) \,/\, L_{1455}(.., a, ..) \tag{4.7}$$

  Momentum independent sources of error are the target position, misalignments between outer layer and beampipe, or beampipe and PIN diode, shape of the active volume of the PIN diode, and the thickness of the beampipe window.

  Hence, momentum independent sources of error do only contribute to the error of the relative normalization.

- the errors Δb_p and Δb_{1455} of the parameter b at independent beam momenta are uncorrelated. These sources of error will be named *momentum dependent*:

  $$Q(.., b_p, b_{1455}, ..) = L_p(.., b_p, ..) \,/\, L_{1455}(.., b_{1455}, ..) \tag{4.8}$$

  Momentum dependent sources of error are the horizontal beam position and width, as well as the beam direction. All these parameters are a function of the beam momentum. To illustrate the meaning of a momentum dependent source of error, consider e.g. the measured horizontal beam position (see Subsection 3.2.1 and Figure 5.2) as a source of error. It will probably deviate from the real beam position. The sign and magnitude of this deviation at two different beam momenta can be completely different. Consequently, the errors at the different beam momenta are uncorrelated.

  Therefore, momentum dependent sources of error contribute to the error of the relative normalization *and* to the error of the absolute normalization.

This distinction is necessary, because error propagation for momentum independent and momentum dependent sources of errors is different.

Propagation of Momentum Independent Sources of Error

To propagate momentum independent sources of error, $Q(a) = L_p(a) / L_{1455}(a)$ must be considered. Applying standard rules of error propagation and differentiation to $Q(a)$ gives the following equation:

$$\frac{\Delta Q}{Q}(a) = \left| \frac{\partial L_p}{\partial a} \cdot \frac{1}{L_p} - \frac{\partial L_{1455}}{\partial a} \cdot \frac{1}{L_{1455}} \right| \cdot \Delta a \tag{4.9}$$

with: Δa: error of parameter a

$\Delta Q / Q$: relative error of ratio Q

For beam momenta p close to 1455 MeV/c, the luminosities per count L_p and L_{1455} should behave very similar with respect to the parameter a. As a result the two terms of Equation (4.9) almost cancel and the error of Q becomes negligible. In fact, at a beam momentum of exactly 1455 MeV/c the ratio Q equals one, because $L_p = L_{1455}$. The ratio Q becomes independent of any parameters and the error of Q vanishes completely.

Propagation of Momentum Dependent Sources of Error

For momentum dependent sources of error, the ratio Q merely serves the purpose to combine all simulation related quantities. The luminosities per count L_p and L_{1455} can be examined independently. The errors propagate like two independent sources of error. In fact, the values b_p and b_{1455} of the parameter b at beam momenta $p_{beam} = p$ and $p_{beam} = 1455$ MeV/c can be thought of as results of two independent measurements of the parameter b at the respective beam momenta. The error of the luminosity per count L_p with respect to the parameter b at a beam momentum p can be calculated from:

$$\frac{\Delta L_p}{L_p}(b_p) = \left| \frac{\partial L_p}{\partial b_p} \cdot \frac{1}{L_p} \right| \cdot \Delta b_p \tag{4.10}$$

with: L_p: luminosity per count simulated at a beam momentum p

Δb_p: error of parameter b at a beam momentum p

The error ΔL_p of the luminosity per count at an arbitrary beam momentum p contributes to the error of the relative normalization.

The error ΔL_{1455} of the luminosity per count at the normalization energy contributes to the error of the absolute normalization. It is calculated by evaluating Equation (4.10) at $p = 1455$ MeV/c.

For small momentum intervals around 1455 MeV/c, e.g. 1400 .. 1500 MeV/c, the luminosities per count L_p and L_{1455} should behave very similar with respect to the parameter b. Hence, the error ΔL_{1455} can be interpreted as contribution to the error of the relative normalization for beam momenta close to 1455 MeV/c.

Combining Systematic Errors

The following equations show how to combine the different systematic errors due to the momentum independent parameters a_i and momentum dependent parameters b_j of the simulation. The equations distinguish between simulation related errors ΔQ_p of the relative normalization, which are a function of the beam momentum, and the simulation related error ΔQ_{norm} of the absolute normalization.

Simulation related errors ΔQ_p of the relative normalization are evaluated from momentum independent errors and from contributions of momentum dependent errors according to the following equation:

$$\left(\frac{\Delta Q_p}{Q_p}\right)^2 = \sum_i \left|\frac{\partial L_p}{\partial a_i}\cdot\frac{1}{L_p} - \frac{\partial L_{1455}}{\partial a_i}\cdot\frac{1}{L_{1455}}\right|^2 \cdot \Delta a_i^2 + \sum_j \left|\frac{\partial L_p}{\partial b_j}\cdot\frac{1}{L_p}\right|^2 \cdot \Delta b_j^2 \tag{4.11}$$

Simulation related errors ΔQ_{norm} of the absolute normalization are only deduced from momentum dependent errors according to:

$$\left(\frac{\Delta Q_{norm}}{Q_{norm}}\right)^2 = \sum_j \left|\frac{\partial L_{1455}}{\partial b_j}\cdot\frac{1}{L_{1455}}\right|^2 \cdot \Delta b_j^2 \tag{4.12}$$

In the following sections, the simulation related contributions to the error of the relative normalization will be denoted ΔQ_{1000}, ΔQ_{1455} and ΔQ_{2500}, since the error of the relative normalization is a function of the beam momentum, the index indicating the momentum examined.

4.1.4 Combining Luminosity Measurements for Left and Right PIN Diodes

Using the left and right PIN diodes as luminosity monitors introduces momentum dependent asymmetries due to varying horizontal beam positions during the acceleration ramp. To minimize this effect, the arithmetic mean L_{mean} of both luminosity measurements is used, when normalizing cross sections:

$$L_{mean} = \frac{1}{2} \cdot C_{norm} \cdot \left(L_{count,left} \cdot N_{e,left} + L_{count,right} \cdot N_{e,right} \right) \tag{4.13}$$

with: $L_{count,left/right}$: luminosity per count from simulation of left/right PIN diode
$N_{e,left/right}$: electron count rate in left/right PIN diode

Unfortunately, L_{mean} is not well suited to study the influence of different error sources, since $L_{count,left}$ and $L_{count,right}$ are multiplied with PIN diode count rates. The count rates depend on the specific runs during which PIN diode data were taken in April 1996. An error analysis of L_{mean} would give results depending on the runs studied. To get more general results, we rewrite Equation (4.13):

$$L_{mean} = C_{norm} \cdot \left(L_{count,mean} \cdot N_{e,mean} + \frac{1}{4} \cdot \Delta L_{count} \cdot \Delta N_{e} \right) \tag{4.14}$$

with: $L_{count,mean}$: arithmetic mean of luminosity per count
$N_{e,mean}$: arithmetic mean of electron count rates
ΔL_{count}: difference of luminosity per count
ΔN_e: difference of electron count rates

The second term involves differences of almost identical values. Typical count rates $N_{e,left}$ and $N_{e,right}$ of the left and right PIN diode measured in April 1996 differ less than 20%. The same is true for the corresponding luminosities per count $L_{count,left}$ and $L_{count,right}$. Error propagation due to the second term is suppressed by a factor of 0.01. For the error analysis of the luminosity L_{mean}, which results from combining the measurements with left and right PIN diode, it is sufficient to study the mean luminosity per count $L_{count,mean}$.

4.2 Sources of Error

In this section possible sources of error are presented. Their properties are discussed and their magnitude estimated. Basically, the systematic errors are determined by the uncertainties of the relative position of the PIN diodes to the overlap of target and beam, uncertainties of the exact geometry of the PIN diodes and, for the left and right PIN diode, uncertainties in the thickness of the beampipe window. It is shown that several sources of error contribute to these uncertainties and can be studied simultaneously.

4.2.1 Beam and Target Properties

The δ-electrons are emitted from the region where beam and target overlap. Thus, beam and target properties have to be considered, when discussing sources of errors.

While being accelerated the beam slightly changes its position, width and direction. The target does not move during the acceleration cycle. It is a fiber of small cross section mounted parallel to the x-axis. During the acceleration cycle the overlapping volume of beam and target can change position only along the x-axis, while staying fixed along the y- and z-axis. The overlapping volume is determined by beam position x_{beam} and width $\sigma_{x,beam}$ and the target position y_{target} and z_{target}. The beam directions x'_{beam} and y'_{beam} also vary during the acceleration cycle.

These parameters were fitted for individual data taking periods from pp-elastic scattering data taken with the outer layer [Roh95]. They are relative to the position of the outer layer.

Momentum Dependent Properties

The horizontal mean beam position x_{beam}, beam width $\sigma_{x,beam}$ and beam direction x'_{beam}, and the vertical beam direction y'_{beam} are fitted for each individual beam momentum bin. As far as their magnitude relative to the outer layer is concerned, these parameters are momentum dependent and their error (one standard deviation) is determined by the quality of the fit [Roh95]:

$$\begin{aligned} \Delta x_{beam} &= 1 \text{ mm} \\ \Delta\sigma_{x,beam} &= 0.5 \text{ mm} \\ \Delta x'_{beam} &= 0.5 \text{ mrad} \\ \Delta y'_{beam} &= 0.5 \text{ mrad} \end{aligned} \tag{4.15}$$

Momentum Independent Properties

Unlike the parameters of the previous paragraph, the target position parameters y_{target} and z_{target} are fitted for all beam momenta simultaneously. Their errors are momentum independent and are due to the quality of the fit:

$$\begin{aligned} \Delta y_{target} &= 1 \text{ mm} \\ \Delta z_{target} &= 1 \text{ mm} \end{aligned} \tag{4.16}$$

4.2.2 Misalignments between Outer Layer and Beampipe

Measurements of the position of outer layer and beampipe showed that they were not exactly aligned [Wei99]. Beam and target properties are determined relative to the outer layer as mentioned in Subsection 4.2.1. The misalignment of outer layer and beampipe contributes to the overall position error of PIN diodes mounted onto the beampipe. Consequently, these sources of error apply to the left and right PIN diode only.

The misalignment includes a small shift of the beampipe relative to the outer layer (x_{pipe}, y_{pipe}, z_{pipe}) as well as a rotation of the beampipe axis in relation to the axis of the outer layer (x'_{pipe}, y'_{pipe}). The misalignment is momentum independent and the error of the misalignment measurement is [Wei99]:

$$\begin{aligned}\Delta x_{pipe} &= 0.4\ \text{mm}\\ \Delta y_{pipe} &= 0.5\ \text{mm}\\ \Delta z_{pipe} &= 0.5\ \text{mm}\\ \Delta x'_{pipe} &= 0.7\ \text{mrad}\\ \Delta y'_{pipe} &= 0.8\ \text{mrad}\end{aligned} \tag{4.17}$$

The position of the inner PIN diode is determined from data measured with the outer layer of the EDDA detector. The misalignment of outer layer and beampipe does not contribute to the overall position error of the inner PIN diode.

4.2.3 Geometry of the PIN Diodes

The geometry of the PIN diodes was modeled with great care. Fortunately, the correct dimension of the inactive parts of these silicon detectors are accurately known from their data sheets. Nevertheless, the shape and size of the active silicon volume is a function of the applied voltage. The dimensions of the active silicon volume are a source of errors.

As additional sources of errors, the overall position and alignment of the PIN diodes relative to the beampipe have to be considered.

Misalignment between Left/Right PIN Diode and Beampipe

A misalignment between PIN diodes and beampipe only contributes to the position errors of PIN diodes mounted onto the beampipe. A translation of the PIN diode relative to the beampipe adds to the overall systematic error due to misalignment and is momentum independent. This error is larger for the right PIN diode setup used in April 1996, because the right PIN diode was mounted on top rather than inside the beampipe window and its positioning was less precise.

An estimate of the errors due to the misalignment between left or right PIN diode and the beampipe are given in the following table:

Error	**Left PIN**	**Right PIN**
Δx_{PIN}	0.3 mm	0.3 mm
Δy_{PIN}	0.5 mm	1.0 mm
Δz_{PIN}	0.5 mm	1.0 mm

(4.18)

The next argument will show that errors due to a rotation of the PIN diode relative to the beampipe are small. Consider small rotations of e.g. the right PIN diode. Rotations around its y- and z-axis are negligible, because the right PIN diode touches the beampipe leaving little room for misalignments. When mounting the PIN diodes, rotations around the x-axis of more than one degree are obvious. So only small rotations of less than one degree need to be considered as source of error. Figure 4.1 shows a rotation of the right PIN diode around the x-axis by five degrees, which exaggerates expected rotation errors for demonstration purposes. Count rates in the two gray areas are approximately identical, because they cover almost the same solid angle and the variation of the differential cross section is small. When rotating the right PIN diode, the count rate detected increases by the count rate in area A and decreases by the count rate in area B. These effects cancel and the change in count rate is negligible. This argument can be repeated for the remaining areas of the rotated PIN diode. Hence, the error introduced due to rotations of the PIN diodes relative to the beampipe can be neglected and will not be discussed further in this chapter.

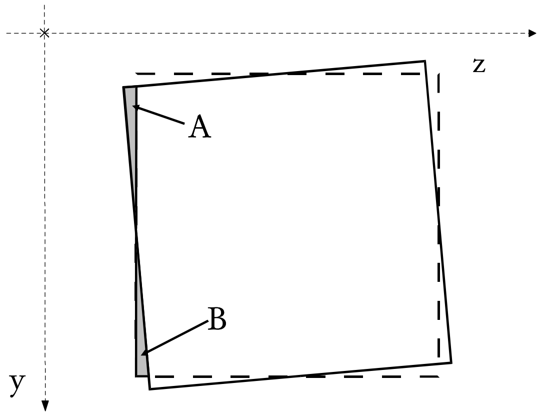

Figure 4.1: Errors due to small rotations of the right PIN diode around its x-axis.

Position Errors of the Inner PIN Diode

The mounting mechanism used to position the inner PIN diode inside the beampipe is inaccurate. The method to determine the position of the inner PIN diode from data introduces specific errors as described in Subsection 3.2.2. The following table lists these specific errors:

Error	Inner PIN
Δx_{PIN}	0.5 mm
Δy_{PIN}	1.0 mm
Δz_{PIN}	0.5 mm

(4.19)

Shape of the Active PIN Volume

The shape and size of the active volume of a PIN diode is determined by the applied voltage and the resulting electric field. The precise shape of this volume is only approximately known, so a box of quadratic cross section $l_{active} \times l_{active}$ and thickness d_{active} was assumed. The value of l_{active} is from the data sheets, its error is estimated. A correctly determined thickness d_{active} of the box turned out to be essential to an accurate simulation of energy loss spectra. In April 1996, the method described in Subsection 3.2.2 was used to determine the thickness d_{active} from data, the error of the method is given in [Hei95].

$$\begin{aligned} \Delta d_{active} &= 10\,\mu\text{m} \\ \Delta l_{active} &= 0.5\text{ mm} \end{aligned} \tag{4.20}$$

4.2.4 Geometry of the Beampipe

Before electrons emitted from the target are detected in the left or right PIN diode, they pass the beampipe window. For the windows the thickness of the beampipe is reduced to a thickness d_{Al} of approximately 250 μm (left PIN diode) or 229 μm (right PIN diode). The window thickness was measured using the magnetic induction method according to ISO 2178 [Fis01]. Details of the measurement are presented in Appendix D. The error of this measurement is given by:

$$\Delta d_{Al} = 5\,\mu\text{m} \tag{4.21}$$

4.2.5 Combining Related Sources of Error

Errors in the relative position of the PIN diode to the target result from several sources of error. But studying each source of error independently is unnecessary, since the luminosity per count basically depends on the relative position of target and PIN diode. It is sufficient to define proper input parameters for the simulation, which combine related sources of error into one parameter. Consider e.g. misalignments of the right PIN diode along the x-axis. The luminosity per count basically depends on the total misalignment x_{total}:

$$x_{total} = -x_{beam} + x_{pipe} + x_{PIN} - x_{0,right} \tag{4.22}$$

with:
$x_{0,right} = 80$ mm: basic offset of PIN diode rel. to origin
x_{beam}: mean position of beam relative to outer layer
x_{pipe}: position of beampipe origin relative to outer layer
x_{PIN}: position of PIN diode relative to beampipe origin

For convenience the basic offset $x_{0,right}$ of the right PIN diode relative to the origin is introduced to set $x_{total} = 0$ for the typical setup of Chapter 3 with beam on the z-axis. The errors add up quadratically, e.g.:

$$(\Delta x_{total})^2 = (\Delta x_{beam})^2 + (\Delta x_{pipe})^2 + (\Delta x_{PIN})^2 \tag{4.23}$$

Using Monte Carlo calculations, the influence of the total misalignment x_{total} on the luminosity per count can be studied by varying the vertex in the target from which δ-electrons are emitted. The following table shows, which sources of error contribute to the different input parameters of the simulation.

Parameter	*Left PIN Diode*	*Right PIN Diode*	*Inner PIN Diode*
x_{total}	Δx_{beam}, Δx_{pipe}, Δx_{PIN}	Δx_{beam}, Δx_{pipe}, Δx_{PIN}	Δx_{beam}, Δx_{PIN}
y_{total}	Δy_{target}, Δy_{pipe}, Δy_{PIN}	Δy_{target}, Δy_{pipe}, Δy_{PIN}	Δy_{target}, Δy_{PIN}
z_{total}	Δz_{target}, Δz_{pipe}, Δz_{PIN}	Δz_{target}, Δz_{pipe}, Δz_{PIN}	Δz_{target}, Δz_{PIN}
x'_{total}	$\Delta x'_{beam}$, $\Delta x'_{pipe}$	$\Delta x'_{beam}$, $\Delta x'_{pipe}$	$\Delta x'_{beam}$
y'_{total}	$\Delta y'_{beam}$, $\Delta y'_{pipe}$	$\Delta y'_{beam}$, $\Delta y'_{pipe}$	$\Delta y'_{beam}$

Table 4.1: Errors of input parameters in the simulation, and the sources of errors which contribute to the different PIN diodes.

The previous argument is based on the assumption that the luminosity per count depends only on the relative position of target and PIN diode. But the misalignment of left and right PIN diode relative to the beampipe does not only influence the relative position of target and PIN diode. It also changes the position of the PIN diode relative to the walls of the beampipe window. To study the influence of the window walls on the luminosity per count, simulations with the following detector setups were performed:

- a PIN diode mounted on top of a beampipe of 250 μm thickness. No beampipe window was used. No window walls could deflect δ-electrons back into the PIN diode.
- the standard setup

The luminosity per count changed by 0.4 %, which was beyond statistical errors. This can be considered the upper limit of the influence of the window walls on the luminosity per count. Hence, a small deviation of a PIN diode relative to its window walls are a negligible source of error.

4.2.6 Combining Left and Right PIN Diode

For the combination of left and right PIN diode care has to be taken, when combining related sources of errors. The errors due to a misalignment of each PIN diodes to the beampipe are independent for each PIN diode and the quadratic sum of errors must be considered. On the other hand, errors due to the misalignment of beampipe and outer layer as well as errors of the beam or target properties are common to both PIN diodes and strongly correlated, such that they may add up or, as it is more often the case, cancel.

4.3 Simulations

The Monte Carlo simulations for calculating the functional dependence of the luminosity per count on different input parameters are presented.

4.3.1 Simulation Setup

The easiest way to perform systematic studies of errors in the relative position of PIN diode and target is letting the target event generator do all variations of the relative position. To enable the systematic studies proposed, the target generator was initialized to generate events at a vertex of $(x_{total}, y_{total}, z_{total})$, the simulated beam particles moving in the direction (x'_{total}, y'_{total}), while assuming a beam width of σ_x=0. In the basic setup, all input parameter x_{total}, y_{total}, z_{total}, x'_{total} and y'_{total} were zero. The box shape of the simulated active volume inside a PIN diode was chosen to be of thickness d_{active}= 340 μm and of length and width l_{active}= 10 mm. The thickness of the beampipe window was d_{Al} = 250 μm. Apart from these settings, according to the systematic studies of this chapter, the simulation method described in Sections 3.2 and 3.3 was used.

Starting with the basic setup described one parameter was individually varied for each set of simulations while the other parameters were left unmodified. All simulations were performed with a pencil beam of width σ_x=0. Subsection 4.3.3 shows a method to derive results for extended beams with a width σ_x>0.

4.3.2 List of Performed Simulations

The parameters listed in Table 4.2 were varied to study their influence on the luminosity per count. Each parameter was varied in the range given and after each simulation increased by the increment listed in Table 4.2. Since the basic setup described in Subsection 4.3.1 is included in each set of simulations, it is performed only once. Each set of simulations was carried out for the three PIN diode setups

Parameter	**Range**	**Increment**	**Simulated Events**
x_{total}	-10 mm .. 10 mm	2 mm	200000 [800000]
y_{total}	-10 mm .. 10 mm	2 mm	800000 [200000]
z_{total}	-10 mm .. 10 mm	2 mm	200000
x'_{total}	-10 mrad .. 10 mrad	2 mrad	200000 [800000]
y'_{total}	-10 mrad .. 10 mrad	2 mrad	800000 [200000]
d_{active}	300 μm .. 400 μm	20 μm	200000
l_{active}	9.5 mm .. 10.25 mm	250 μm	200000
d_{Al}	210 μm .. 280 μm	10 μm	200000 [0]

Table 4.2: Input parameters of the simulation at beam momenta p_{beam} of 1000 MeV/c, 1500 MeV/c and 2500 MeV/c. If the number of events simulated for the inner PIN diode differs from those for the left/right PIN diode it is shown in brackets.

	Symmetry properties	
Parameter	**Left/Right PIN Diode**	**Inner PIN Diode**
x_{total}	none	$L(x_{total}\text{-}3.3\text{mm})=L(\text{-}x_{total}+3.3\text{mm})$
y_{total}	$L(y_{total}) = L(-y_{total})$	none
z_{total}	none	none
x'_{total}	none	$L(x'_{total}) = L(-x'_{total})$
y'_{total}	$L(y'_{total}) = L(-y'_{total})$	none
d_{active}	none	none
l_{active}	none	none
d_{Al}	none	none

Table 4.3: Symmetries of luminosity per count $L=L_{count}$ with respect to the parameters examined.

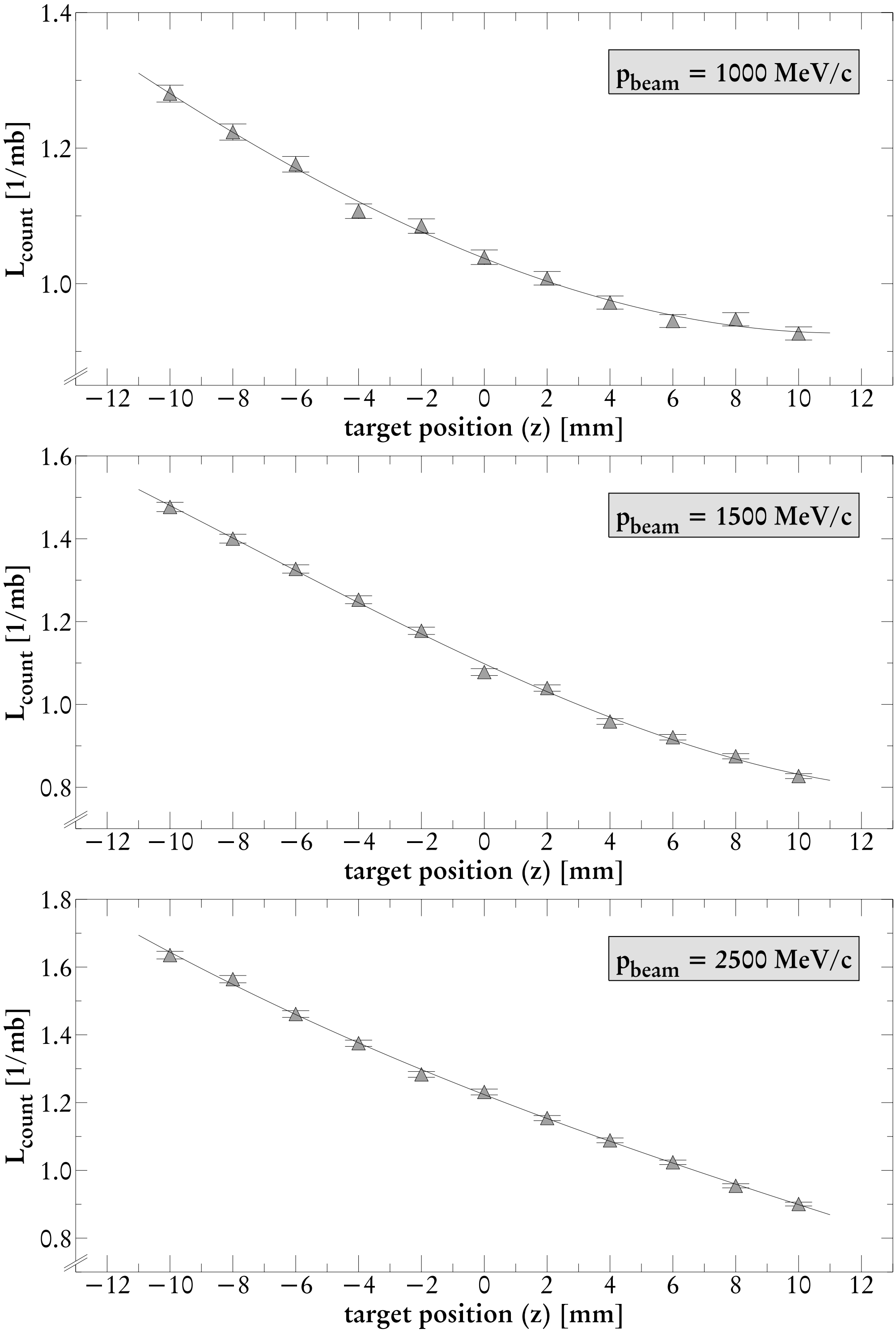

Figure 4.2: Example of a systematic study on parameter dependence. Shown is the luminosity per count (left PIN diode) for three beam momenta as a function of different target positions z_{total}. The large range of z-positions was chosen to allow for the application of results to the atomic beam target of the second phase of the experiment.

mentioned before. The beam momentum was chosen to be 1000 MeV/c, 1455 MeV/c and 2500 MeV/c for each PIN diode and parameter setup. Since the luminosity per count varies only slightly for large momenta, other large momenta were not simulated.

A total of 531 simulations were performed, each typically lasting 1.5 hours for 200000 events on a PC workstation using a Pentium II-CPU at 266 MHz. The total computation time for all simulations was 67 days. To achieve results in a reasonable time, the tasks were distributed among several PC workstations.

Table 4.3 lists symmetries of the luminosity per count $L=L_{count}$ with respect to the parameters examined for the different PIN diode setups. They result from the particular positions of each PIN diode relative to the z-axis. The symmetries were taken advantage of, when fitting polynomials to the simulated data to find an analytic description. For most symmetries listed, the luminosity per count L_{count} is an even function of the parameter examined. When fitting polynomials, only coefficients of even order had to be considered.

Due to the symmetries presented, the variation of the luminosity per count L_{count} with respect to the examined parameter is typically small. To allow proper fitting of polynomials to simulated data, statistics had to be increased. This is the reason for the large number of events simulated for certain combinations of examined parameter and PIN diode listed in Table 4.2. For practical reasons, the symmetries were not taken advantage of to skip calculation of L_{count} for the symmetric partner of an already given parameter value. E.g. for the left PIN diode results of the luminosity per count $L_{count}(y_{total})$ for y_{total}=-2mm are (within statistical limits) identical to the results for y_{total}=2mm. Instead, the extra effort was used as a means to increase statistics and, indirectly, the quality of the fit.

A typical result of the systematic study of the luminosity per count L_{count} and its dependence on a parameter is shown in Figure 4.2. For the left PIN diode the luminosity per count is plotted versus the z-coordinate of the target position for a beam momentum of 1000 MeV/c, 1500 MeV/c and 2500 MeV/c. The continuous line shows the polynomial fitted to the simulation data. Obviously, the variation of L_{count} with z_{total} is relatively large resulting in a large error. Indeed, sources of errors related to the input parameter z_{total} are a major contribution to the overall error (see next section and Appendix B). The range from -10 mm to 10 mm for the z-position of the target is larger than the range of typical values for the CH_2-target used in April 1996. For studying the systematic errors related to the beam and target position a large range of values was chosen in order to allow the application of the results to the atomic beam target of the second phase of the EDDA experiment.

4.3.3 Calculating the Effects of an Extended Beam

Once the functional dependence of the luminosity per count on the horizontal beam position is established, the dependence on the beam width $\sigma_{x,beam}$ can be deduced by calculating the convolution of the position dependence with the intensity distribution of the beam. The δ-electrons generated by a beam of width $\sigma_{x,beam}$ can be considered as superposition of δ-electrons knocked out of the target by a distribution of beams with zero width. The efficiency is proportional to the number of δ-electrons detected. Then, given a beam of non-vanishing width, the efficiency $\varepsilon(\sigma_{x,beam}, x_{beam})$ can be calculated using the convolution of $\varepsilon(0, x_{beam})$ with the intensity distribution $G(\sigma_{x,beam}, x_{beam})$ of the beam. For fixed solid angles, $\varepsilon(x)$ is proportional to the inverse of the luminosity per count $1/L_{count}(x)$ (see Subsection 3.1.2). The following equation gives the functional dependence of the luminosity per count on the position x_{beam} and width $\sigma_{x,beam}$ of the beam:

$$\frac{1}{L_{count}\left(\sigma_{x,beam}, x_{beam}\right)} = \int G\left(\sigma_{x,beam}, x_{beam} - x\right) \cdot \frac{1}{L_{count}\left(0, x\right)} \, dx \tag{4.24}$$

with: L_{count}: luminosity per count
$G(\sigma_{x,beam}, x_{beam})$: normalized gaussian distribution with standard deviation $\sigma_{x,beam}$ and mean value x_{beam}

The analogue procedure can be applied to calculating the distribution of the directions x'_{beam} and y'_{beam} of the beam.

4.4 Results

The simulated results of the last section are used to determine the systematic errors of the ratio Q due to the parameters examined. A given set of parameters reflects only a specific fixed combination of beam, target and other properties. An error estimate for all valid combinations of parameters (i.e. all valid combinations of beam, target and other properties) is calculated to give an overall systematic error of this method. The error estimates are discussed.

4.4.1 Finding the Overall Systematic Error

The simulated dependencies of the luminosity per count on the parameters of Table 4.3 are fitted with polynomials, reflecting their respective symmetries. In addition, Equation (4.24) permits calculating the luminosity per count with respect to the beam position and width. Now, the luminosity per count is available as function of the parameters examined. For each parameter these functions can be inserted either into Equation (4.11) to calculate the systematic errors ΔQ_p of the relative normalization or into Equation (4.12) to calculate the systematic error ΔQ_{norm} of the absolute normalization.

Applying Equations (4.11) and (4.12) determines the errors of the ratio Q only for a given, fixed set of values of the parameters, i.e. a specific beam and target setup. In order to find a good estimate for the error $\Delta Q/Q$ independent of beam and target setups, Equations (4.11) and (4.12) were numerically maximized over the range of valid values for the input parameters of the simulation. The range of valid values is given, e.g. for the x-coordinate of the beam position, by the typical range of values for the beam position measured in April 1996 and a small safety margin. For the x-coordinate of the beam position the range of valid values used is -5 mm .. 5 mm.

4.4.2 Overall Systematic Errors for Different PIN Diodes

For each PIN diode setup Table 4.4 lists the overall error estimates. It has to be kept in mind that this is the overall error for any valid combination of simulation parameters. For a simulation with a specific combination of input parameters the resulting error can be smaller. The full listing of all sources of error for all beam momenta and PIN diode setups is condensed in Appendix B.

PIN diode	ΔQ_{1000}	ΔQ_{1455}	ΔQ_{2500}	ΔQ_{norm}
inner	0.4 %	0.2 %	0.5 %	0.2 %
left+right	3.0 %	0.5 %	0.9 %	0.5 %
right	4.0 %	1.5 %	1.9 %	1.5 %
left	3.5 %	1.4 %	1.5 %	1.4 %

Table 4.4: Overall error estimates for different PIN diode setups and beam momenta. ΔQ_{1000}, ΔQ_{1455} and ΔQ_{2500} denote simulation related contributions to the error of the relative normalization, ΔQ_{norm} shows contributions to the error of the absolute normalization.

To interpret the different results some general consideration are appropriate:

- the efficiency is basically determined by the kinetic energy of the δ-electrons emitted into the solid angle of the PIN diodes. The smaller the kinetic energy the smaller is the range of the δ-electrons and the larger is the multiple scattering (including backscattering) in the beampipe window and in the PIN diodes.
- the efficiency decreases rapidly for small beam momenta (see Figure 1.4). A variation of the beam momentum typically results in a shift of the energy distribution of δ-electrons detected in the PIN diodes.

- the luminosity per count is very sensitive to changes in the PIN diode's position relative to the target. A shift of the target typically has two effects:
    - the size of the solid angle covered by the PIN diode changes:
      A variation in the size of solid angle covered by the PIN diode mostly affects the luminosity per count through the integrated Rosenbluth cross section. A simple calculation shows the effect to be almost independent of the beam energy. For momentum independent sources of error this effect typically cancels, since numerator and denominator of Q are affected simultaneously.
    - the mean scattering angle of δ-electrons detected in the PIN diode shifts:
      The luminosity per count is affected via the integrated Rosenbluth cross section. The effect on the cross section can be calculated using Equation (3.6). The relative variation of the cross section with a shift of the scattering angle depends only slightly on the beam momentum.
      The luminosity per count is affected via the efficiency. A shift of the mean scattering angle results in a shift of the energy distribution of δ-electrons detected. Consequently, results of a shift of the mean scattering angle and a variation of the beam momentum are similar. For the left and right PIN diode the effect on the luminosity per count via the efficiency will be large for small beam momenta while decreasing with increasing beam energies.

The error estimates ΔQ_{1455} for errors of the ratio Q for beam momenta close to 1455 MeV/c are generally smaller than the errors for other beam momenta. Close to beam momenta of 1455 MeV/c momentum independent errors vanish. Q becomes the ratio of two functions L_p and L_{1455}, which behave almost identical with respect to the parameter examined. The partial derivatives of Equation (4.9) will cancel each other and only momentum dependent errors survive.

The following subsections will discuss the major contributions of different sources of errors to the overall error of Q. Complete results are given in Appendix B.

The Left PIN Diode

For the left PIN diode, the contribution of Δx_{total}, Δz_{total} and Δd_{Al} to the overall error ΔQ is typically larger than 98% for all beam energies. Other sources of error can be neglected. The contribution of the errors mentioned is determined by calculating ΔQ with all other sources of error set to zero.

The Right PIN Diode

The right PIN diode is more sensitive to the input parameters than the other PIN diodes. This is due to the fact that it is mounted on top of the beampipe window.

Electrons passing the 229 μm thick beampipe window are considerably scattered, especially at low beam momenta. The drift distance of 1.75 mm between beampipe window and PIN diode enhances the efficiency losses introduced by this effect.

Another consequence is the increased contribution of the error Δl_{active} to the overall error of Q. The contribution of Δl_{active} is almost equal to the contribution of Δx_{total}, Δz_{total} or Δd_{Al}. For the right PIN diode, the relative increase in detected δ-electrons with respect to an increased size of the active silicon volume depends on the beam energy. For high beam momenta, the number of detected δ-electrons will be proportional to the size of the active silicon volume, multiple scattering will not play an important role. For low beam momenta, the number of detected δ-electrons will largely depend on the angular distribution of δ-electrons leaving the beampipe. The influence of l_{active} on the luminosity per count is highly dependent on the beam momentum. Consequently, the influence of l_{active} on the nominator and denominator of the ratio Q differs substantially and leads to a non-vanishing error ΔQ in Equation (4.9), even though deviations of l_{active} are applied to nominator and denominator simultaneously.

The Combination of Right and Left PIN Diode

The combination of left and right PIN diode is not as sensitive to errors as the left or right PIN diode alone. The dependence of this setup on the x-position of the beam is reduced to second order effects due to its symmetry. Since this dependence is one of the major contributions to the overall error, the overall error is considerably reduced.

The symmetry of this setup is broken, because the right PIN diode is mounted on top of the beampipe window. Optimal results can be expected, if the right PIN diode is also mounted inside its beampipe window. Such a setup was used for data taking in September 1995.

The Inner PIN Diode

For the inner PIN diode the maximum overall error of Q is 0.6%. Errors for beam momenta of 1000 MeV/c and 2500 MeV/c are approximately identical.

Each contribution of the errors Δx_{total}, Δy_{total}, $\Delta y'_{total}$, Δz_{total} and Δl_{active} is on the level of about 0.2% to 0.3% and varies only slightly with beam momentum. There are several reasons for this effect. The efficiency of the inner PIN diode is almost independent of the beam momentum. Consequently, the influence of parameters on the efficiency is suppressed. Only the influence of these parameters on the cross section via the solid angle affects the luminosity per count. But this influence is relatively independent of beam momentum. Accordingly, the error of Q due to momentum independent errors, like Δy_{total}, Δz_{total}, Δl_{active} and the momentum independent parts of Δx_{total}, is suppressed.

Additionally, the influence of the errors in $\Delta x'_{total}$ and in the momentum independent parts of Δx_{total} is suppressed due to the symmetries affecting the inner PIN diode (see Table 4.3). As a result, the errors mentioned contribute all on the same level as $\Delta y'_{total}$.

4.4.3 Conclusion

The inner PIN diode is a preferred tool for an accurate measurement of the luminosity. It allows to determine the relative luminosity with a systematic error of less than 0.5%. Combining the errors of the relative and absolute normalization the systematic error of the simulation is less than 0.6% for the full momentum range. However, due to its position inside the beampipe, the inner PIN diode unfortunately detects background, which cannot be corrected, as discussed in the next chapter.

The combination of left and right PIN diode is the next best choice for an accurate measurement of the luminosity. It allows to determine the relative luminosity with a systematic error of less than 0.9% for the major part of the momentum range. Only for beam momenta below 1455 MeV/c the systematic error of the relative normalization increases from 0.5% to 3.0%. When comparing results for low beam energies with results from the secondary electron monitor SEM, appropriate care has to be taken. Combining the errors of the relative and absolute normalization the systematic error of the simulation is less than 1.0% for the major part of the momentum range. For small beam momenta below 1455 MeV/c it increases to 3.1%.

Chapter 5

Results of Efficiency Calculations

This chapter lists Monte Carlo simulations carried out to calculate the luminosity per count for the PIN diode setups of April 1996. Resulting luminosities are compared to measurements taken with the secondary electron monitor SEM.

5.1 Performed Simulations

In this section the simulated luminosities per count for the data taking period of April 1996 are presented. The examined luminosities per count included three different setups of PIN diodes. For each PIN diode three distinct beam and target setups had to be simulated.

5.1.1 Simulation Setup

The simulation setups refer to the three PIN diodes described in great detail in Section 3.2. They include the inner PIN diode, which was mounted inside the beampipe prior to the data taking period of April 1996, the left PIN diode mounted inside the left beampipe window and the right PIN diode, which was mounted on top of the right beampipe window. In setups prior to April 1996, the right PIN diode had been positioned inside the beampipe window like the left PIN diode.

In April 1996 a fourth PIN diode was positioned into the beampipe window at an angle of $\phi = 270°$. It was named *bottom* PIN diode, accordingly. Due to a lack in electronic equipment the setup of the bottom PIN diode did not allow separation of hadronic background. Consequently, proper analysis of the data taken was impossible and a calculation of the luminosity per count considered unnecessary.

Beam and target setup have a large influence on the luminosity per count for each particular PIN diode. Especially target position as well as beam position and width play an important role. For this reason, one series of simulations has to be performed for each distinct set of beam and target properties. For analyzing beam and target setups of all runs taken in April 1996, three typical beam and target setups can be found. All runs of a particular setup are equivalent in the sense that an efficiency calculation performed for each run would render identical results for a given beam momentum. The particular setups can be represented by three typical runs: run 182, run 421 and run 965. Table 5.1 shows a list of runs equivalent to the chosen representative runs. Some runs are not considered, because the data was taken for hardware calibration or reference measurements.

Representative Run	*List of Equivalent Runs*
Run 182	75..258
Run 421	412..704, 778..894
Run 965	895..1078

Table 5.1: List of runs with equivalent beam and target characteristics. Missing runs correspond to hardware calibration runs or reference measurements.

Every simulation for the PIN diodes and representative runs was performed using the simulation method described in Section 3.2.

5.1.2 List of Simulations Performed

For each combination of a representative run and PIN diode one set of simulations was prepared and executed. Each set of simulations covers a momentum range of 1000 MeV/c ... 3250 MeV/c in 50 MeV/c increments. To initialize the target event generator for the representative runs listed in Table 5.1, automatic selection of beam and target properties from databases was used.

For each simulation 800000 events were generated, tracked through the detector and analyzed. For the left and right PIN diode this procedure has a statistical error of approximately 0.7 %, which is well below the systematical errors of 2.1 % to 4.3 % for the right and 2.0 % to 3.8 % for the left PIN diode. For the inner PIN diode the statistical error is 0.34 % and of the same order as the systematical error of 0.3 % to 0.6 %.

A total of 414 simulations were performed, each calculation lasting 6 hours for 800000 events on a PC workstation using a Pentium II-CPU at 266 MHz. The total computation time for all combinations of representative run, PIN diode setup and beam momentum was 14 weeks and 5 days. To accomplish these results in a reasonable time six PC workstations were employed for 2.5 weeks.

5.2 Simulation Results

Simulation results for representative run 965 are presented as a typical example of the simulations performed. For each PIN diode setup the resulting efficiencies and luminosities per count are discussed.

5.2.1 General Considerations

Typical results for representative run 965 of the simulations performed are given in Figure 5.1. The first plot presents the detection efficiency ε_{det} of the three PIN diodes, the second the calculated luminosity per count. Here, the detection efficiency ε_{det} is defined as the number of *detected hits* N_{det} divided by the number of *geometrical hits* N_{geom}:

$$\varepsilon_{det} = N_{det} / N_{geom} \tag{5.1}$$

A simulated event is counted as geometrical hit, if the projected path of the initial electron through the detector intersects with the active volume of the PIN diode examined. When the electron is tracked through the detector and the energy loss in the considered active volume is above the threshold of the PIN diode examined, it is counted as detected hit. Subsection 3.2.4 gives a precise definition of detected and geometrical hits and lists the thresholds used.

This definition of efficiency was chosen, because of its simple physical interpretation. For a pencil beam it is identical to the definition of Equation (3.8), if the solid angle Ω_0 exactly covers the active volume of the PIN diode, i.e. the number of geometrical hits N_{geom} is equal to the number $N_e(\Omega_0)$ of δ-electrons emitted into the solid angle Ω_0. For extended beams the solid angle covered by the active volume of the PIN diode varies with each event vertex. The following equation allows converting the detection efficiency ε_{det} into the efficiency $\varepsilon(\Omega_0)$ defined in Equation (3.8):

$$\varepsilon(\Omega_0) = \varepsilon_{det} \cdot N_{geom} / N_e(\Omega_0) \tag{5.2}$$

with: N_{geom}: number of geometrical hits in the PIN diode
$N_e(\Omega_0)$: number of electrons emitted into solid angle Ω_0

The luminosity per count L_{count} is related to the detection efficiency accordingly:

$$L_{count} = \frac{N_e(\Omega_0)}{\varepsilon_{det} \cdot N_{geom} \cdot \int_{\Omega_0} \frac{d\sigma}{d\Omega} \cdot d\Omega} \tag{5.3}$$

with: $d\sigma/d\Omega$: Rosenbluth cross section

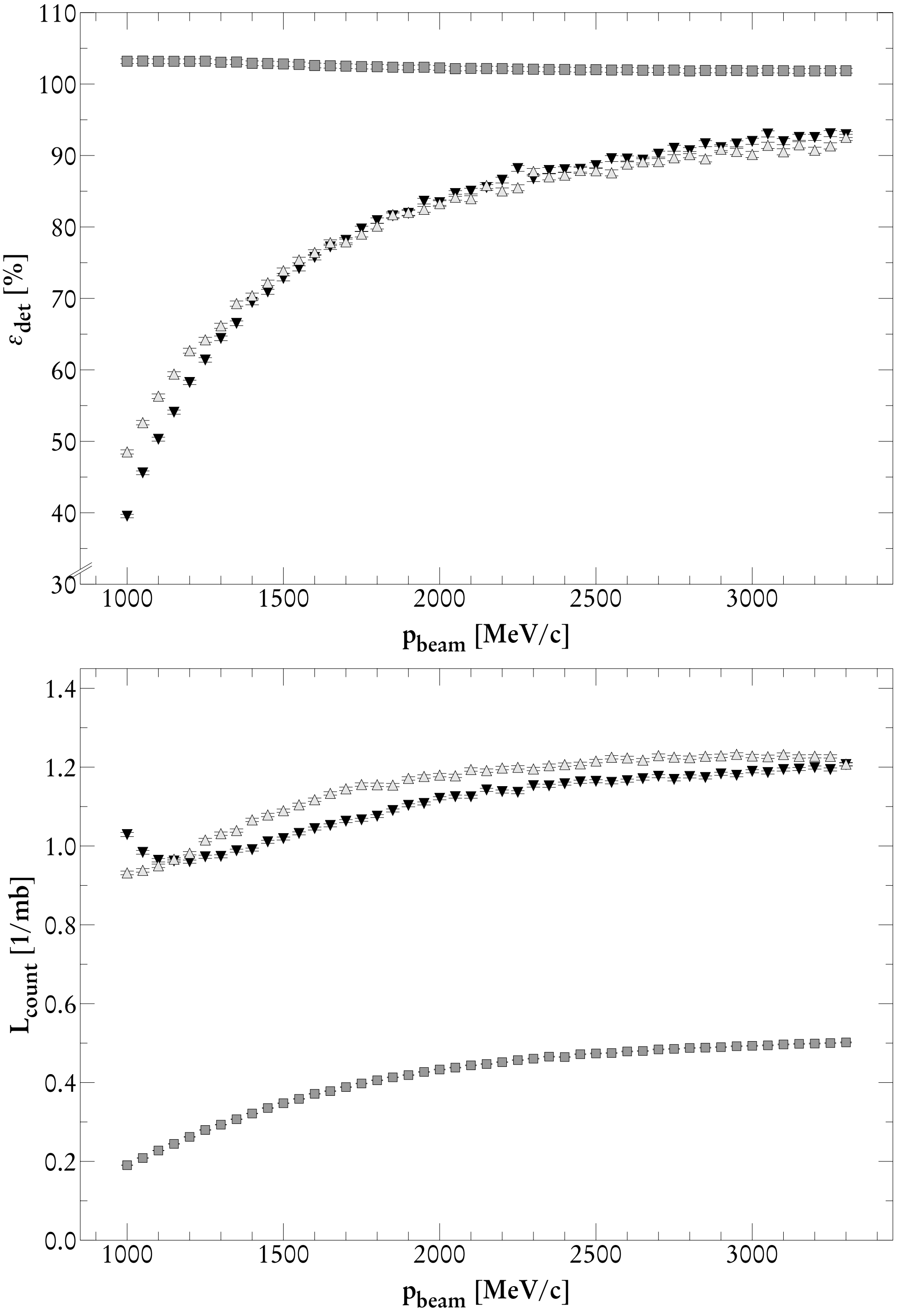

Figure 5.1: Typical results for the detection efficiency ε_{det} and luminosity per count L_{count} versus beam momentum for run 965 and three PIN diode setups: ■ inner PIN diode, ▼ left PIN diode, △ right PIN diode. The detection efficiency of the inner PIN diode is higher than 100% due to multiple scattering effects in the inactive PIN volume (see text).

5.2.2 The Inner PIN Diode

For the inner PIN diode Figure 5.1 shows that the detection efficiency ε_{det} is nearly constant with a slight drop from 103.2 % to 101.8 % (±0.24 %) in the beam momentum range from 1000 .. 3250 MeV/c. The detection efficiency is higher than 100%, because more electrons than expected from mere geometrical considerations are detected. Using the simulation software to visualize individual events simulated, a certain number of electrons can be seen to enter the silicon volume, into which the active PIN diode volume is embedded. On a straight path these electrons would pass by the active volume without entering. Nevertheless, a considerable fraction of electrons change direction and enter the active PIN diode volume due to multiple scattering. Consequently, the number of detected hits is larger than the number of geometrical hits. Since the kinetic electron energy increases with beam momentum, the mean multiple scattering angle decreases. Less electrons are able to enter the active volume leaving the surrounding silicon. Therefore, the detection efficiency of the inner PIN diode decreases with beam momentum.

The luminosity per count L_{count} is a smooth function of beam momentum. Its functional dependence is dominated by the variation of the Rosenbluth cross section with beam momentum, since the detection efficiency is nearly constant. This confirms the achievement of one of the design goals of the inner PIN diode.

5.2.3 The Left and Right PIN Diode

Figure 5.1 demonstrates that the efficiency of left and right PIN diode behave similar. Due to the fact that the right PIN diode is mounted *onto* the beampipe window, its efficiency can generally be expected to be lower than the efficiency of the left PIN diode. This is true for beam momenta above 1600 MeV/c and for the other beam and target setups not shown (see Appendix D). For beam momenta below 1600 MeV/c, the efficiency of the right PIN diode is higher. For the specific beam and target setup of run 965 and equivalent runs, the mean position of the beam is off axis and closer to the right PIN diode for low beam momenta (see Figure 5.2). The right PIN diode is mounted at x = -80 mm, the left PIN diode at x = 75.25 mm. The mean emission angle θ of electrons detected in the right PIN diode is shifted towards smaller angles. As a result, the mean kinetic energy of electrons detected increases and the detection efficiency is enhanced. The equivalent argument applies to the left PIN diode, only with opposite signs. The efficiency of the left PIN diode decreases, for small beam momenta in Figure 5.1 even below the efficiency of the right PIN diode. This again demonstrates that a precise knowledge of the beam and target properties is essential for an accurate calculation of the luminosity per count for both PIN diodes.

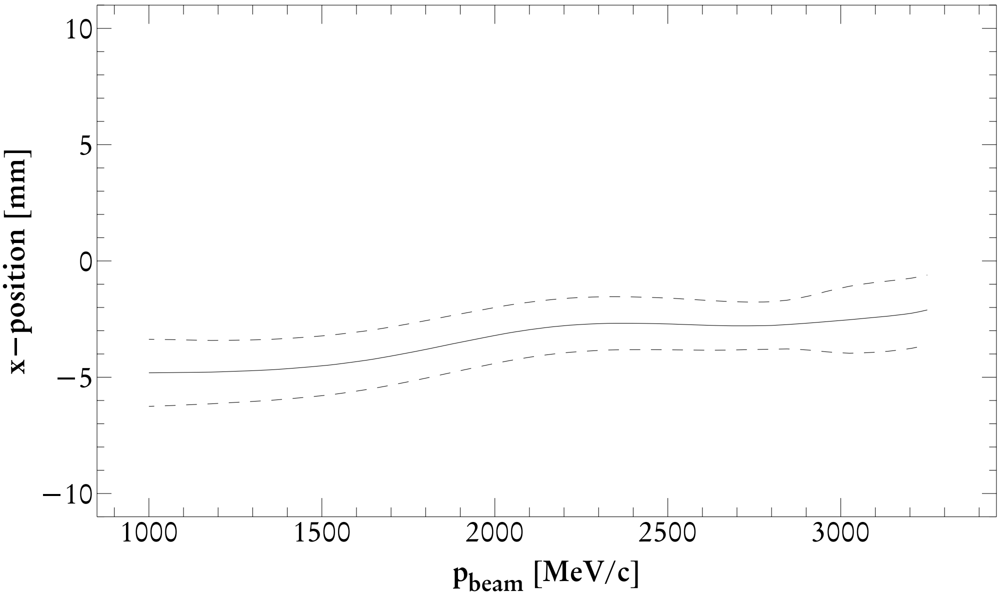

Figure 5.2: Mean position and width of the COSY beam versus beam momentum for overlapping region of target and beam in April 1996 (run 965).

The luminosity per count is a relatively smooth function of the beam momentum. Irregularities on the 1.5% level in the functional dependence of the luminosity per count are due to variations in beam and target properties or due to statistics.

5.3 Comparing SEM and PIN Monitor

The luminosities per count simulated and electron count rates measured in April 1996 are used to compare results of the different PIN diode luminosity monitors to the data taken with the SEM.

5.3.1 Background Separation for the PIN Diodes

The PIN diode luminosity monitor is based on measuring δ-electrons, which are emitted from the target due to proton-electron elastic scattering. Nevertheless, hadronic background processes in the target, e.g. proton-proton elastic scattering, are also detected. Count rates in the PIN diodes have to be corrected for hadronic background, accordingly. Due to their low energy of 0.5 MeV to 1.2 MeV, δ-electrons are typically stopped before they reach the outer layer. On the other hand, the energy deposit of hadrons in the outer layer is large enough to be properly detected. A hit in the outer layer in coincidence with a PIN diode allows distinguishing hadronic background from δ-electrons. To reduce random coincidences, only those detector elements of the semi-ring and bar layer, which are in line with a PIN diode and the target, are used. Their discriminated signals create a stop signal for a time-to-digital converter (TDC), which is started by a hit in the associated PIN diode. In the offline analysis the values read out from the TDC enable separation of hadronic background. It has to be stressed that this method only allows correcting background particles emitted from the target.

5.3.2 Analyzed Data

The following subsection names the different samples measured during the data taking period of April 1996. Table 5.2 lists the samples and the runs analyzed. Each sample consists of several runs containing data, which was taken using an identical beam tuning, trigger and target.

The luminosities L_{PIN} measured with the different PIN diodes are set in relation to the luminosity L_{SEM} measured by the SEM. The measured luminosities are sorted into 90 beam momentum bins with a bin width of 25 MeV/c, ranging from a beam momentum of 1000 MeV/c to 3250 MeV/c. For each momentum bin the following ratio R is calculated:

$$R = L_{SEM} \,/\, L_{PIN} \tag{5.4}$$

The luminosity measurements provide relative normalization only. The arbitrary constants of Equations (3.3) and (3.4) scale luminosity results for all beam momenta simultaneously. For both luminosity monitors they are determined by normalizing EDDA cross section data measured at p_{beam} = 1455 MeV/c to high precision cross section data from [Sim93] and [Sim96], measured at the same beam momentum. Consequently, the ratio R must be equal one for a beam momentum of p_{beam} = 1455 MeV/c. In the figures of the following subsections, the data shown are normalized accordingly.

Sample	*List of Analyzed Runs*	*Sample*	*List of Analyzed Runs*
2-1	77..98 (**182**)	6-1	646..681 (**421**)
3-1	100..125 (**182**)	6-2	778..805, 807..814,
4-1	143..182 (**182**)		816..819 (**421**)
4-2	217..258 (**182**)	7-1	895..934 (**965**)
5-1	421..446 (**421**)	8-1	965..995, 997..1001 (**965**)
5-2	466..495 (**421**)	9-1	1032..1078 (**965**)

Table 5.2: List of samples and the runs analyzed. The corresponding representative runs used for simulations are shown in parentheses. Luminosities were analyzed only for measurements with a CH_2-target, because results from luminosity measurements with carbon targets do not enter cross section calculations.

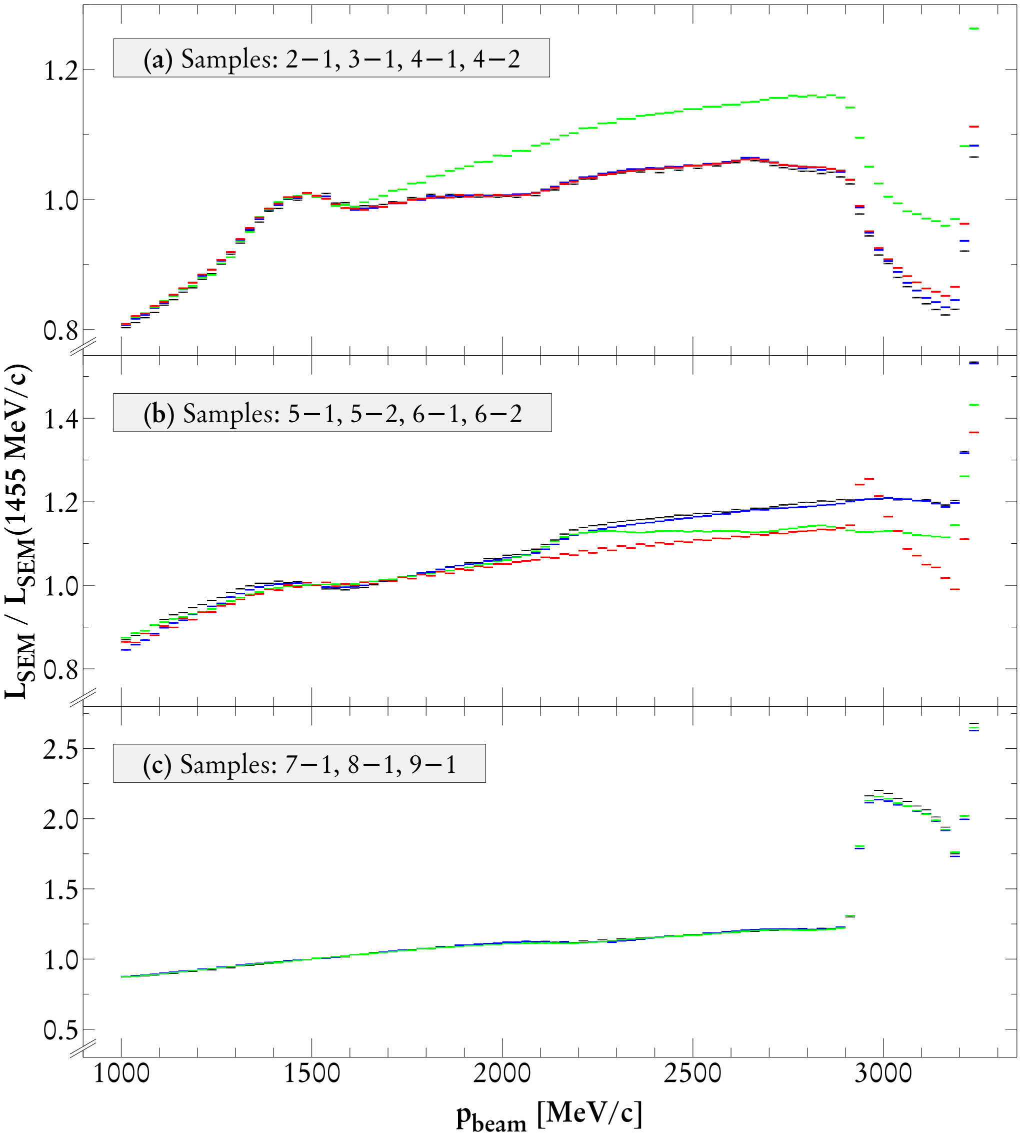

Figure 5.3: Results of the luminosity measurements with the SEM for reference. Luminosities are normalized to unity at a beam momentum of 1455 MeV/c for easier comparison. Errors bars are too small to be visible. The sudden rise of luminosity near 2900 MeV/c is due to a sudden change of the vertical betatron function β_y causing a higher beam density at the fiber target. The rise at 3300 MeV/c is due to the integration of countrate in the flattop.

For the representative runs 421 and 965 all corresponding samples are combined into one plot each. Comparison of SEM luminosities to PIN luminosities show no relevant variation of R within samples 5-1, 5-2, 6-1 and 6-2 (representative run 421) or samples 7-1, 8-1 and 9-1 (representative run 965). For representative run 182, the variation of R with beam momentum displays a behavior, which differs distinctively between sample 4-1 and samples 2-1, 3-1 and 4-2. In order to present this differing behavior, all figures of 5.4-5.11, which display the ratio *R* as function of beam momentum, show two plots for run 182.

Figure 5.3 shows the results of the luminosity measurements with the SEM for reference. Samples taken with identical beam setups are combined in one figure. For most samples of one beam setup, the luminosity as function of the beam momentum is relatively reproducible indicating a stable operation of COSY.

5.3.3 Comparing Results from the Inner PIN Diode to the SEM

Figure 5.4 shows the ratio R for the inner PIN diode. For samples 2-1 to 4-2 (Figure 5.4(a), (b)) R continuously decreases by 20%, while for the other samples (Figure 5.4(c), (d)) the inner PIN luminosity measurements agree with the SEM on a 6% level. From the error analysis of Chapter 4 an agreement of less than 1% had to be expected. Since the efficiency of the inner PIN diode is approximately constant and varies only by 1.5% within this beam momentum range, this behavior cannot be explained by a systematic error in the simulation.

Additionally, the luminosity per count of the inner PIN diode is a smooth function of the beam momentum, which again cannot explain the negative peak of R seen in Figures 5.4(a) and (b) in the momentum range of 2850 MeV/c to 3000 MeV/c. The peak value is 5% below the normal, extrapolated course of R. It is due to a small peak in the count rate detected by the inner PIN diode (Figure 5.5). Only the inner PIN diode measures a peak in the luminosity, which is seen just before the luminosity drops by approximately 20% in the momentum range 2900 MeV/c to 3150 MeV/c (see Figure 5.3(a)). It is reasonable to assume that the inner PIN diode measures an increasing background rate from the beam halo due to increasing beam losses. Beyond 2900 MeV/c, the beam losses lead to a drop in the luminosity. The inner PIN diode has a higher sensitivity to this type of background than the other PIN diodes, because it is mounted inside the beampipe. It is not, like the other PIN diodes, to a certain extent shielded by the beampipe. Hence, background from the beam halo cannot be corrected using the method presented in Subsection 5.3.1.

Related effects are evident in other samples, too. In Figure 5.4(d) a spontaneous increase of R by 3% at a beam momentum of 2900 MeV/c is another hint that the inner PIN diode measures background. It is coincident with the increase in luminosity by a factor 1.8 measured by the SEM (Figure 5.3(c)). Due to the background the luminosity increase seen in the inner PIN diode is smaller than in the SEM. Hence, the ratio R shows a step at 2900 MeV/c.

The measurements of SEM and inner PIN diode agree better for samples 5-1 to 9-1 than for samples 2-1 to 4-2. Assuming that the background seen in the inner

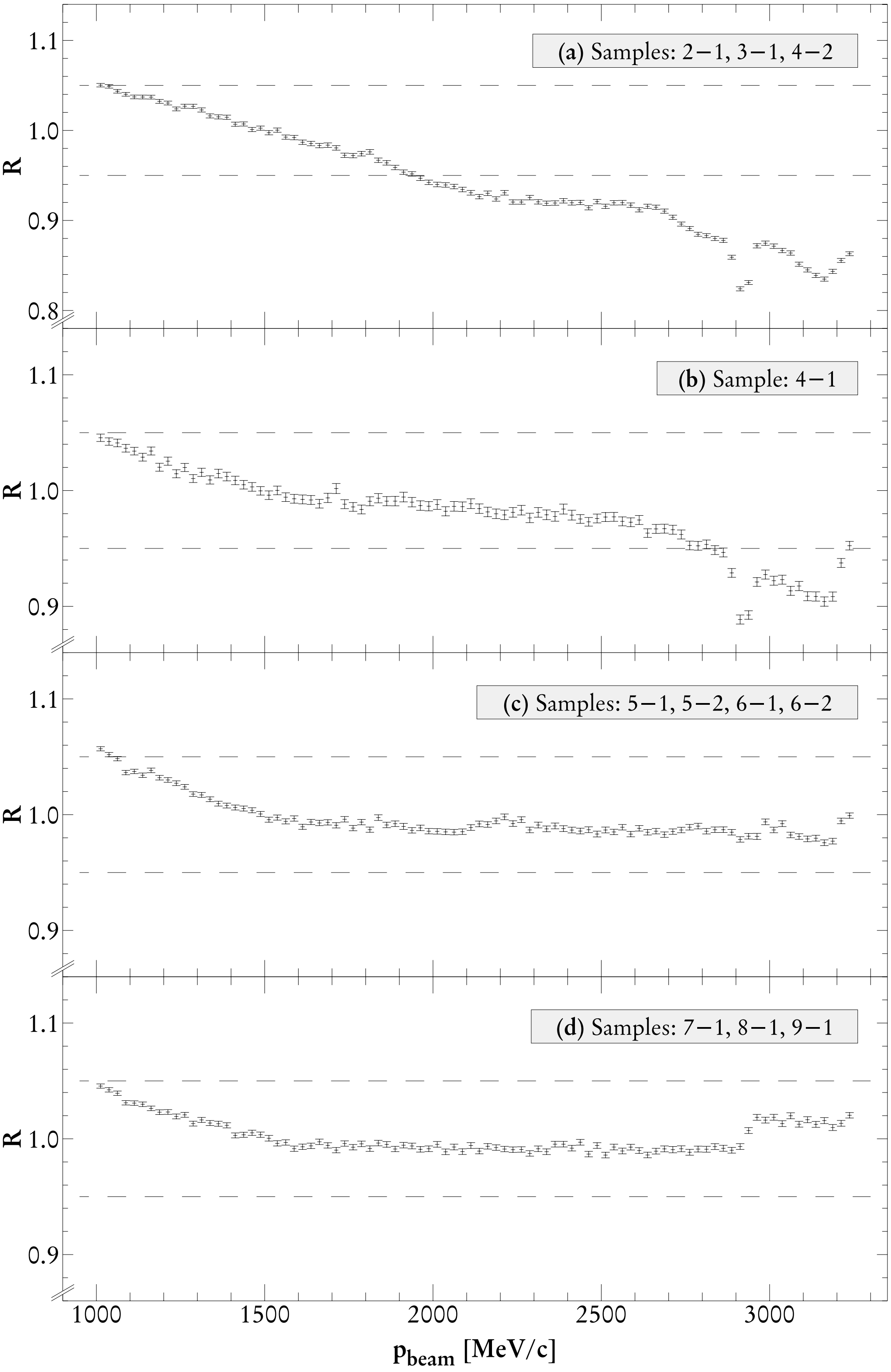

Figure 5.4: Ratio R of SEM luminosity and luminosity of inner PIN diode, $R = L_{SEM} / L_{PIN}$ versus beam momentum.

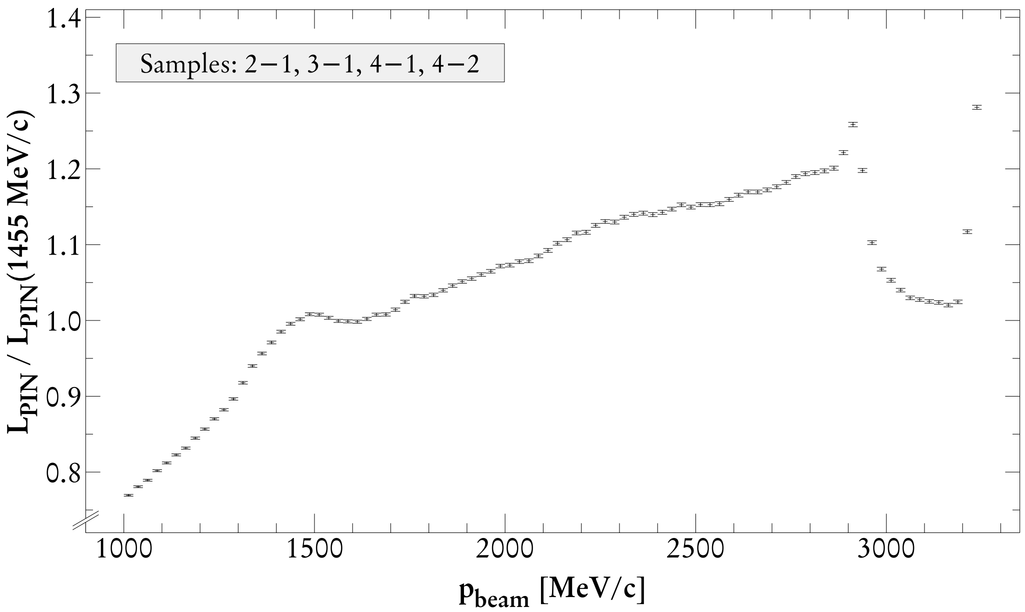

Figure 5.5: Luminosity measured with the inner PIN diode versus beam momentum for combined samples 2-1, 3-1, 4-1 and 4-2. The peak in the luminosity at 2900 MeV/c is only seen by the inner PIN diode. This indicates that the inner PIN diode measures background, which cannot be corrected.

PIN diode was considerably smaller for the samples 5-1 to 9-1 provides a consistent explanation for this observation.

Unfortunately, the data taken in April 1996 are not sufficient to prove the assumption that the inner PIN diode measured to a certain extent background, which did not originate in the target. Nevertheless, this assumption provides a consistent explanation of the data.

5.3.4 Comparing Results from the Left PIN Diode to the SEM

Comparing results for the SEM with the left PIN diode, the variation of the ratio R with beam momentum is presented in Figure 5.6. Again, agreement between the two measurements is not as good as expected, especially for beam momenta below 1200 MeV/c. Above a beam momentum of 1455 MeV/c the measurements typically differ by less than 5%. From the error analysis of Chapter 4, a deviation of only 1.5% for the major part of the momentum range had to be expected.

Looking at energy loss spectra of the left PIN diode, an unexpected, additional peak below the normal spectrum appears for all beam momenta (Figure 5.8). Its position is independent of beam momentum. For small beam momenta the peak is immediately evident, because the spectrum is typically dominated by the stop

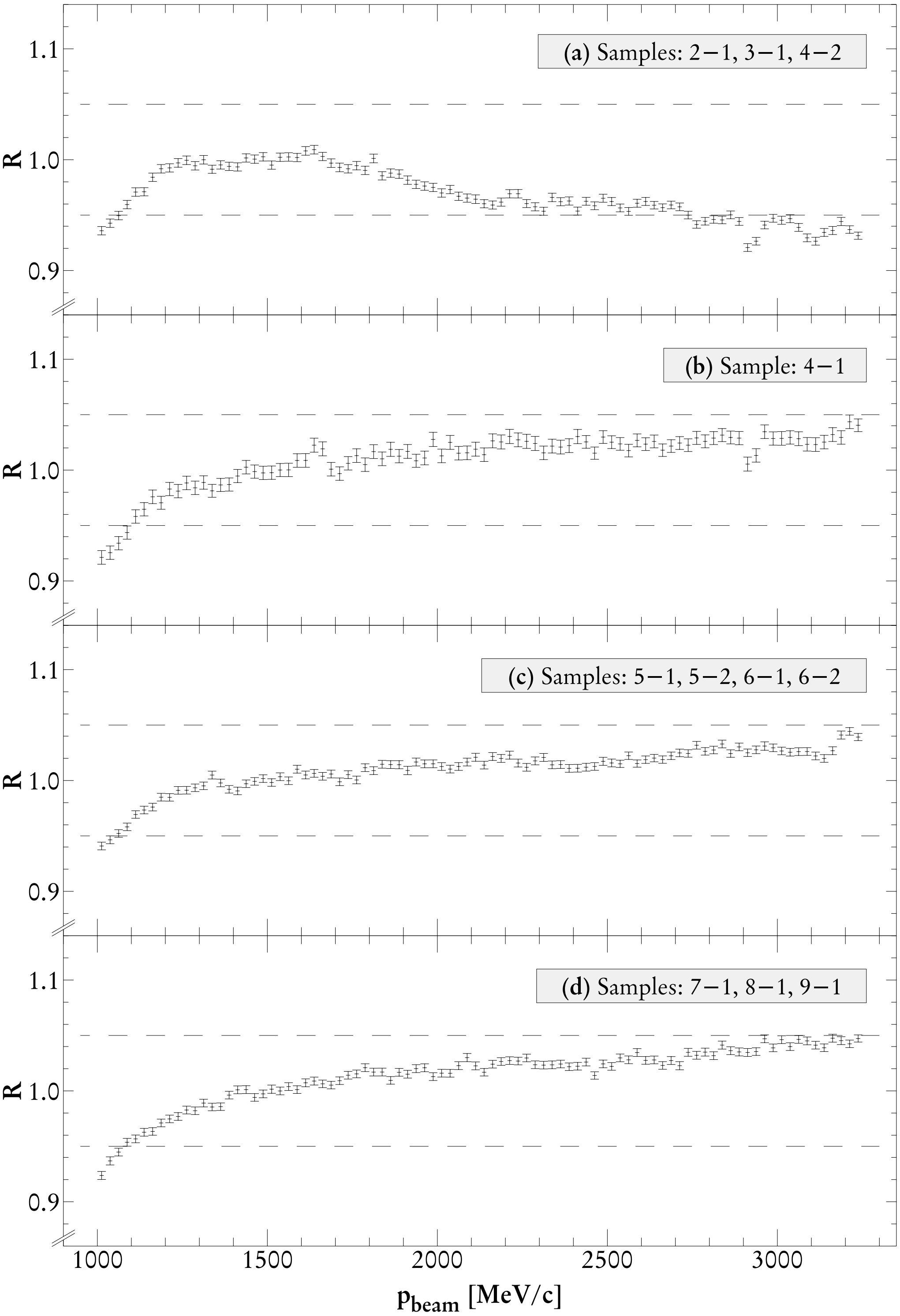

Figure 5.6: Ratio R of SEM luminosity and luminosity of left PIN diode, $R = L_{SEM} / L_{PIN}$ versus beam momentum. Results for the left PIN diode are not corrected for the additional peak seen in the energy loss spectrum of the left PIN diode (see Figure 5.8).

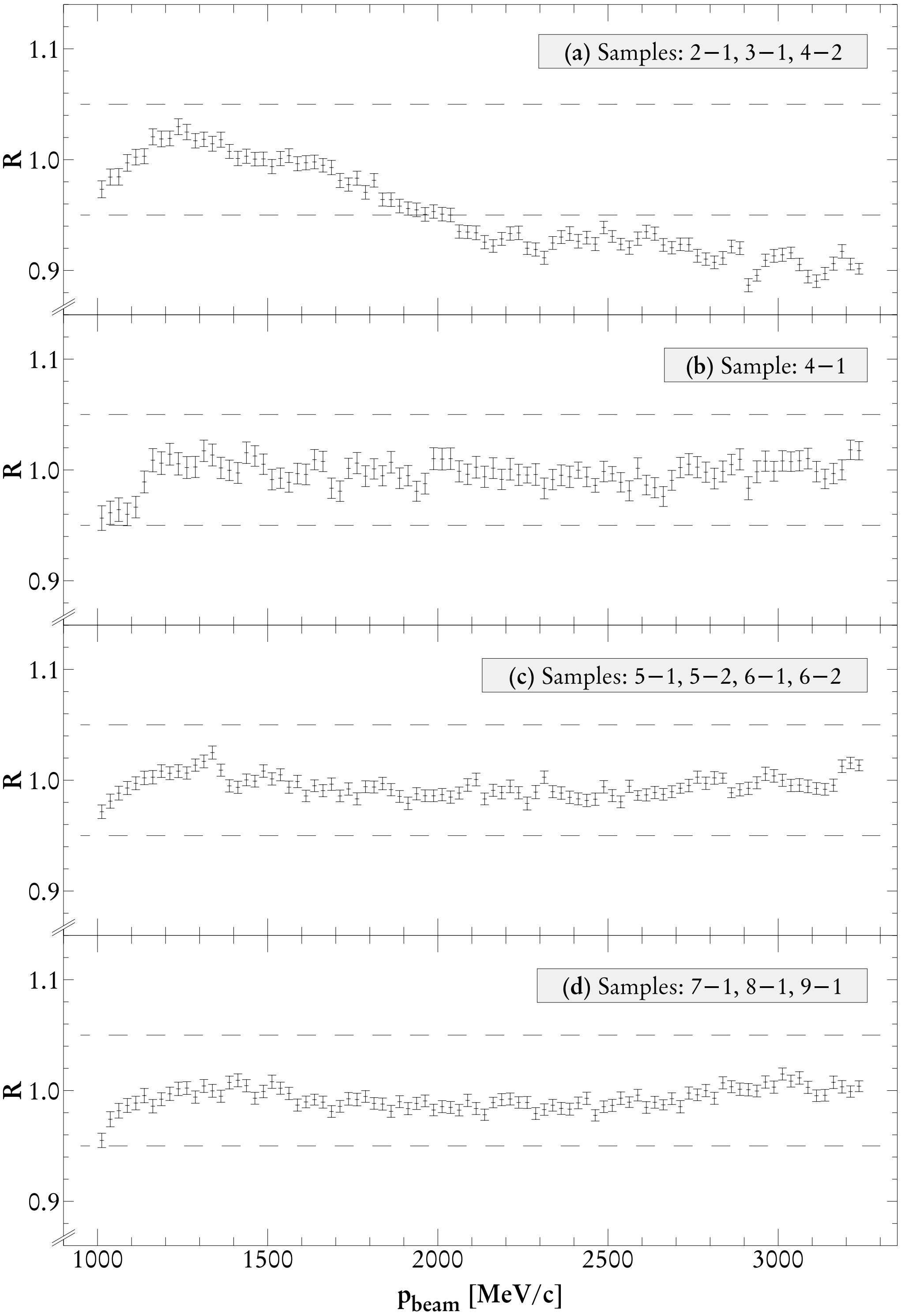

Figure 5.7: Corrected ratio R of SEM luminosity and luminosity of left PIN diode, $R = L_{SEM} \, / \, L_{PIN}$ versus beam momentum. The luminosity measurement with the left PIN diode is corrected by introducing a higher threshold into the offline analysis (see text).

peak of the electrons at energy losses above 200 keV. For higher beam momenta it overlaps with the typical stopping power peak in the spectrum, which is due to particles passing through the active volume of the PIN diode. The low energy edge of the stopping power peak around 100 keV is blurred by the additional peak.

The properties of the additional peak is probably due to electronic noise. To support this assumption, the effects of the additional peak on the luminosity measurement are corrected by introducing a higher threshold $E_{thresh} = 120$ keV into the offline analysis. Then, for each beam momentum bin, electron counts are corrected by the counts above the threshold divided by the total counts in the spectrum. Background subtraction and the efficiency calculation have to be modified accordingly. Results are compared with the SEM luminosity measurements

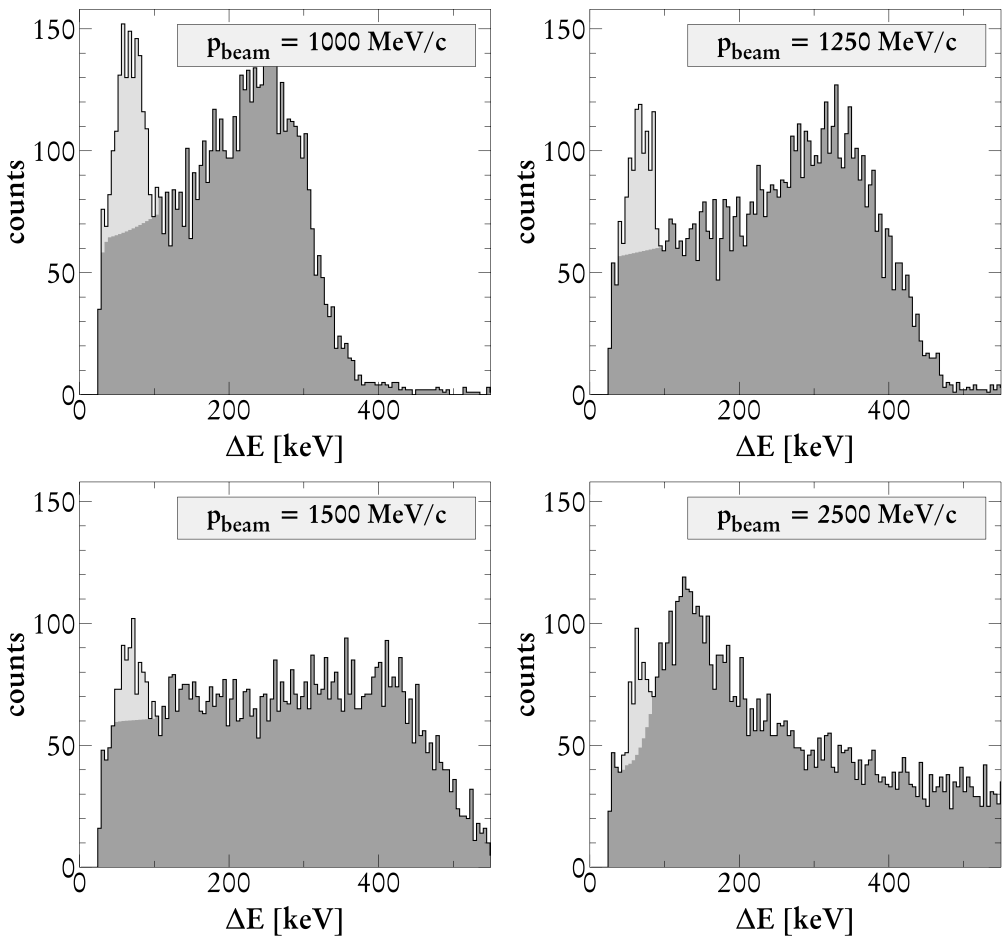

Figure 5.8: Spectra of the left PIN diode from sample 8-1 for four typical beam momenta. Especially at low beam momenta an additional peak, shown in light gray is evident in the spectrum.

and shown in Figure 5.7. The two luminosity measurements now agree on the 1.5% level for the major part of the momentum range and for most samples. Exceptions are the momenta around 1000 MeV/c and the samples 2-1, 3-1 and 4-2.

The data taken in April 1996 do not permit to determine the definite cause of the additional peak in the energy loss spectrum. Nevertheless, electronic noise would consistently explain the additional peak. Whatever the cause of the additional peak might be, it seems reasonable to assume that it is not due to electrons detected in the left PIN diode. Given this assumption, the correction made in the offline analysis are completely valid and can be trusted.

5.3.5 Comparing Results from the Right PIN Diode to the SEM

Figure 5.9 compares results from the SEM to the right PIN diode. For all beam momenta and samples except samples 2-1, 3-1 and 4-2 agreement between the two measurements is better than 5% meeting the expectation from the error analysis in Chapter 4.

Interestingly, the difference are largest for small beam momenta while increasing for higher momenta. Exactly this behavior is predicted for some of the systematical errors studied in Chapter 4. It is reasonable to assume that the deviations of the PIN diode measurements from the results of the SEM are caused by erroneous input parameters of the simulation. When combining results of the left and right PIN diode, the momentum dependent deviation of SEM and PIN measurement almost disappears (Figure 5.11). Only a deviation of the value for the x-coordinate, used in the simulation of the beam position, from its correct, yet unknown one can explain these effects seen in the luminosity measurement.

Initially, the agreement between the two measurements was not satisfactory. Several sources of error in the analysis were studied, before the thickness of the aluminum window in the beampipe emerged as the simulation parameter most probable in error. Luckily, the beampipe used in April 1996 was no longer mounted in the accelerator ring and was available for studying. In July 2000 the beampipe was brought to BBA Friction Group in Leverkusen, Germany, and the thickness of the window was determined. Details of this measurement are given in Appendix D. The two horizontal windows have a mean thickness of $251 \pm 5\,\mu$m and $229 \pm 5\,\mu$m. Unfortunately, the dismounted beampipe does not allow reconstructing the exact way it was mounted in April 1996. Only the vertical axis is fixed; the beampipe could have been mounted in two positions differing by a rotation of 180° around the beam axis. Onto which of the two horizontal windows the right PIN diode was mounted is unknown. There are some hints (scratches on the inner beampipe surface, tape on an unused window) indicating that the right PIN diode was attached to the window with thickness $229\,\mu$m. In-

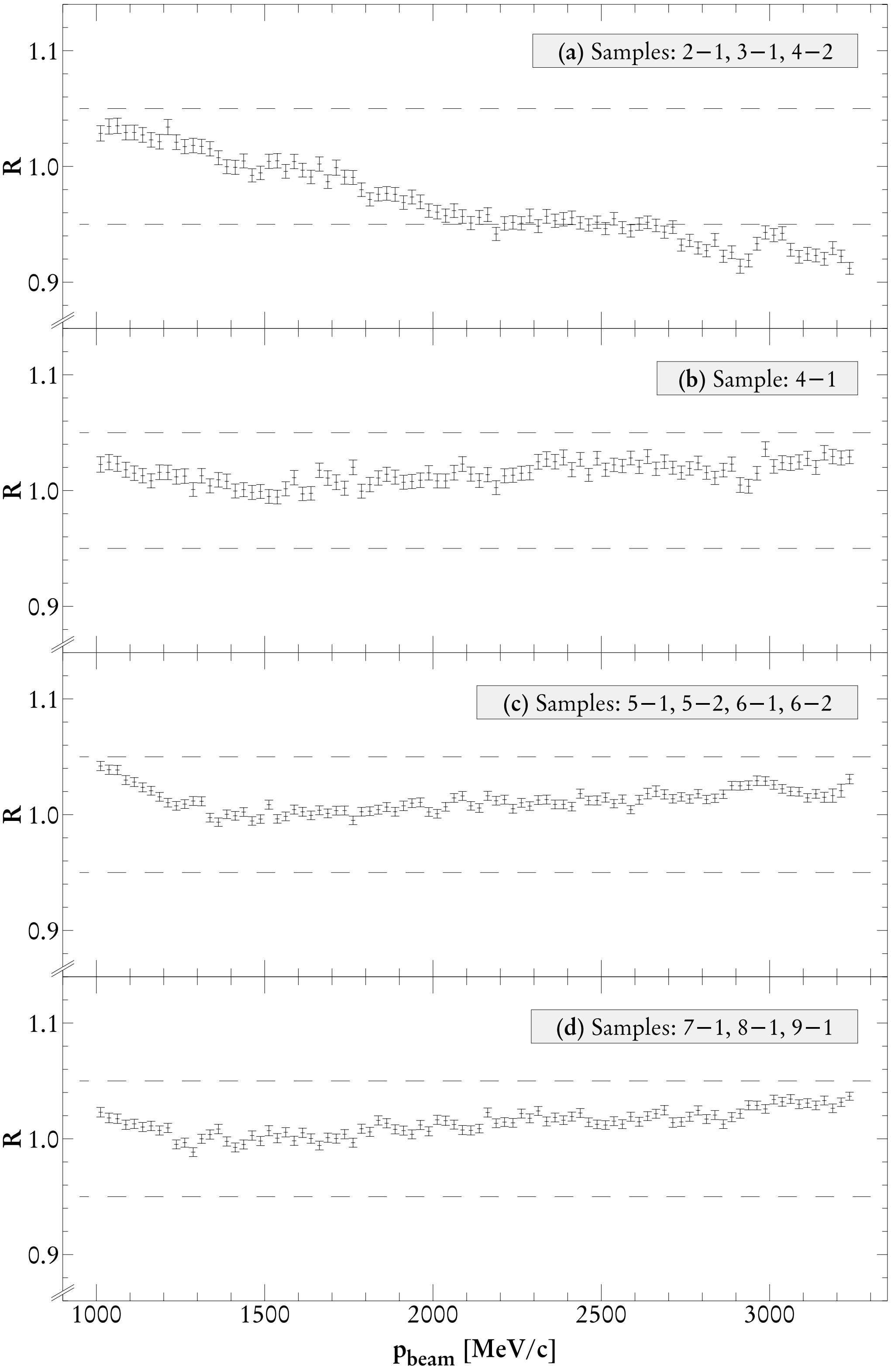

Figure 5.9: Ratio R of SEM luminosity and luminosity of right PIN diode, $R = L_{SEM} / L_{PIN}$ versus beam momentum.

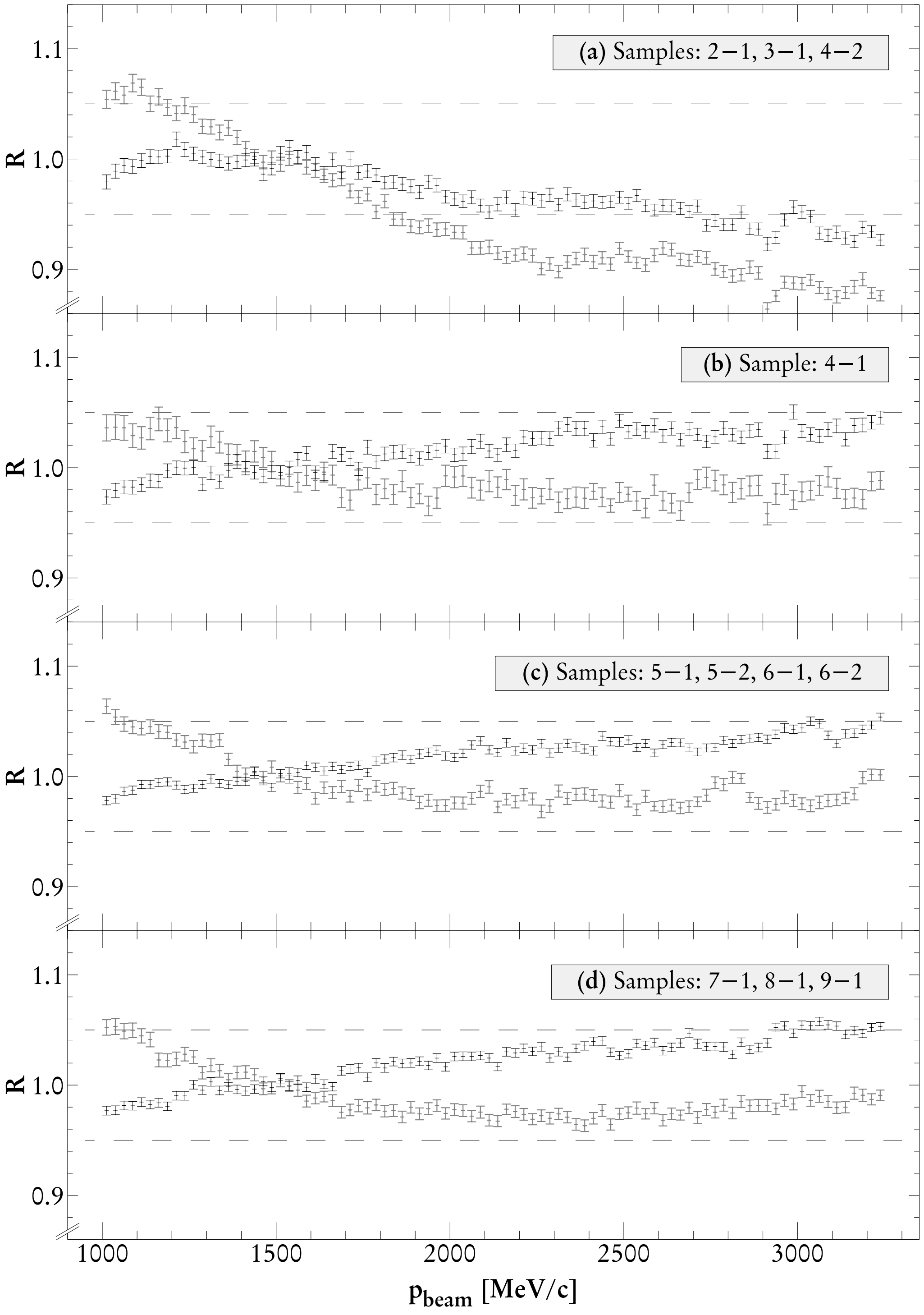

Figure 5.10: Ratio R of SEM luminosity and luminosity of left (+)/right (**+**) PIN diode, $R = L_{SEM}\,/\,L_{PIN}$ versus beam momentum. Results are for completeness only. Efficiency calculations are based on the wrong combination of PIN diode and beampipe window: right PIN diode mounted onto the beampipe window of thickness 251 μm; left PIN diode mounted into the beam pipe window of thickness 229 μm.

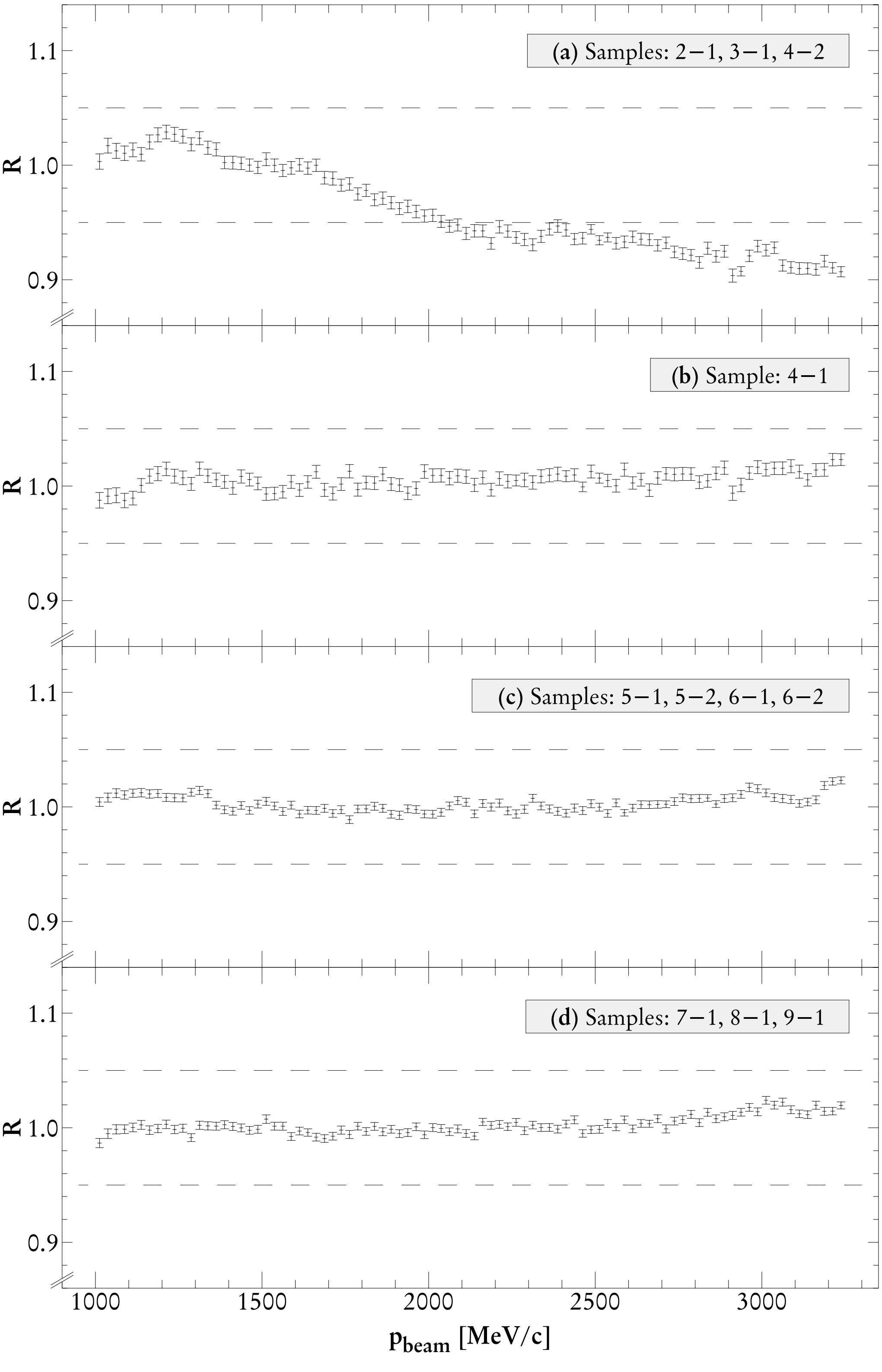

Figure 5.11: Ratio R of SEM luminosity and the mean luminosity of left and right PIN diode, $R = L_{SEM} / L_{PIN}$ versus beam momentum.

deed, only this combination provides sufficient agreement between the measurements with SEM and left/right PIN diode. Results for the other combination of window and PIN diode are presented in Figure 5.10. Clearly, the results shown indicate an insufficient agreement between the measurements with SEM and left/right PIN diodes for this combination.

The results of Figures 5.6 and 5.9 in contrast to results of Figure 5.10 are sufficient proof that the left PIN diode was mounted into the window with thickness 251 μm and the right PIN diode onto the window with thickness 229 μm. Hence, this combination of windows and PIN diodes is considered correct and used for the remaining results of this chapter.

5.3.6 Combining Results from the Left and Right PIN Diode

Figure 5.11 presents results for the mean of the luminosities measured with the left and right PIN diode compared to the SEM. Agreement between SEM and PIN measurements is better than 2.5% for samples 4-1 and 5-1 to 9-1, the discrepancy seen with the other samples is discussed in the next subsection. Still, this result is better than for the left and right PIN diodes alone. Especially the long range variation of R with beam momentum, which is typical for a systematic error, is suppressed in the combined measurements. It is reasonable to assume that the major systematic error in the single PIN diode measurements is an erroneous x-coordinate of the beam position used in the simulation. The effects of this error on the measurement cancel to a certain extent, when the arithmetic mean of the luminosity measurements of the two PIN diodes is computed.

5.3.7 Inconsistency of Samples 4-1 and 4-2

Samples 2-1, 3-1, 4-1 and 4-2 were measured with identical beam properties, which are represented by run 182 for the efficiency simulations. The offline analysis treats these samples independently, because they were taken with different targets or different trigger settings. Samples 2-1 and 3-1 were taken with a CH_2-target named **A2**. For sample 4-1 a new CH_2-target named **A3** was used, only to be replaced by the previous target A2 for sample 4-2. The trigger was modified between samples 2-1 and 3-1 and between samples 3-1 and 4-1.

The luminosity measured with the SEM depends on the target used as shown in Figure 5.12(a). For the momentum range from 1400 MeV/c to 2800 MeV/c and for the target A2, the SEM sees only a 5% increase in luminosity. For each sample taken with target A2 and analyzed individually, the luminosity measured with the SEM is consistent with this behavior. For the same momentum range, but target A3, the SEM measures an increase of the luminosity by 16%. It is worth noting

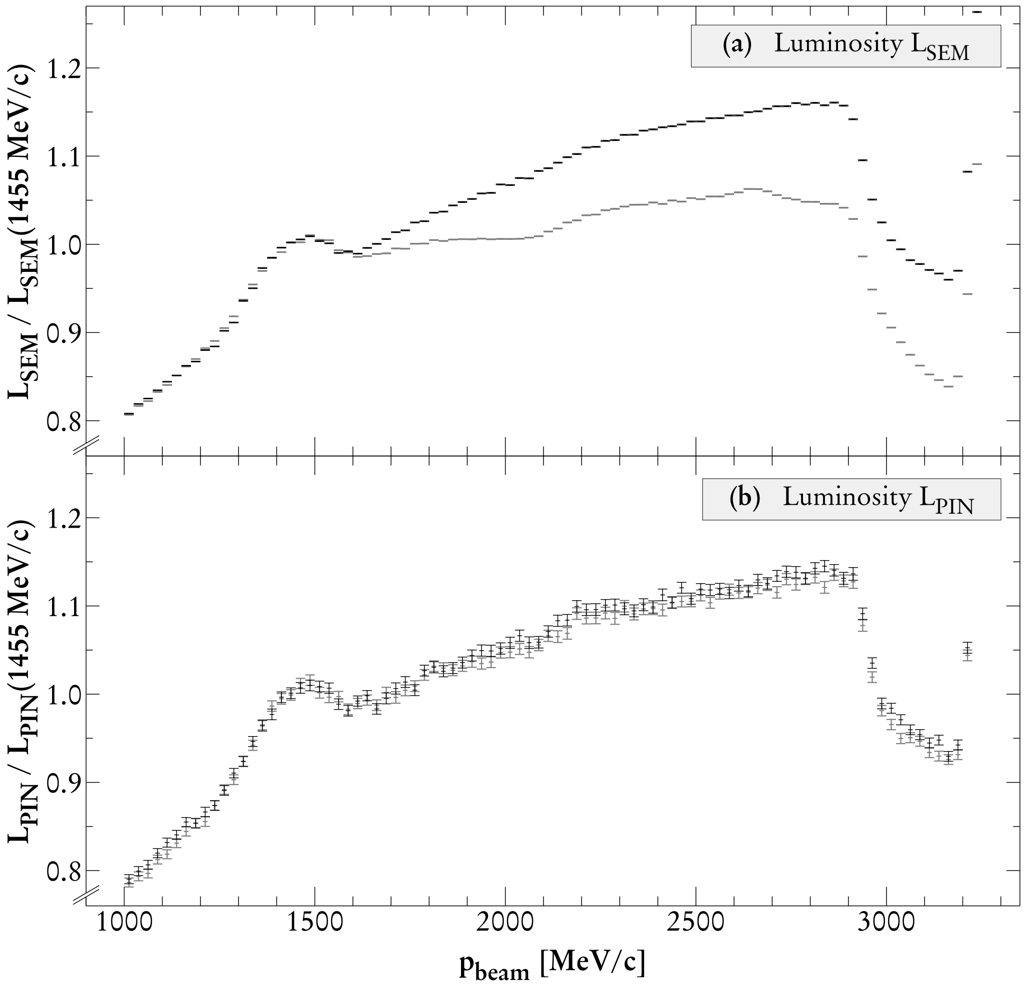

Figure 5.12: Luminosity of COSY beam for samples 2-1, 3-1, 4-2 (gray, target A2) and 4-1 (black, target A3): (a) measured with SEM (b) measured with right PIN diode. Luminosities are normalized to unity at a beam momentum of 1455 MeV/c for easier comparison.

that the luminosity seen by the SEM returns to its original behavior, when target A3 is replaced by the original target A2 for sample 4-2.

This different course of the luminosity with beam momentum for different samples is not seen in any of the PIN diodes. As an example for the PIN diode measurements, Figure 5.12(b) shows results for the right PIN diode. Again, when analyzing each sample individually, results are consistent with the course of the luminosities depicted in Figure 5.12(b). To prove that these results are not caused by inadequate efficiency simulations, raw count rates of the PIN diodes were studied. For any PIN diode, the ratio between raw count rates of any two different samples is constant within 4% for the given beam momentum range. An effect of the target on the PIN diode luminosity could not be observed.

Additionally, other quantities correlated with the beam luminosity were studied. This included the count rates of events with a hit pattern *211* in the outer layer. The pattern 211 denotes that two clusters of bars, one cluster of left and one cluster of right semi-rings were hit. When detector elements, which are immediate neighbors, detect energy losses in coincidence, the group of detector elements is called a cluster. Events from pp-elastic scattering are typically detected as hit pattern *211*. For simplicity reasons carbon background was not subtracted from the count rates. Neither count rates from the outer layer nor the trigger count rate gave reason to believe that the momentum dependence of the relative luminosity changed with a change of targets.

The following summarizes the situation:

- Luminosity measurements of PIN diodes and SEM are in good agreement for all samples but samples 2-1, 3-1 and 4-2.
- All PIN diode measurements *and* the count rates from the outer layer indicate that no change in the course of the luminosity occurred, when targets were changed.
- These observations even hold, when samples 4-1 and 4-2 are divided in subsamples being individually analyzed.

Given these observations, it does not seem advisable to trust the luminosity measurements with the SEM for samples 2-1, 3-1 and 4-2. Until a thorough study of the effects leading to these discrepancies is carried out and a complete understanding of the mechanisms involved is accomplished, samples 2-1, 3-1 and 4-2 should not be included in cross section results. Such a study, however, is beyond the scope of this thesis.

5.4 Conclusion

The following section conclude the results of the luminosity measurements with the PIN diodes. Since the left/right PIN diode and the inner PIN diode have quite different properties, results are presented individually.

5.4.1 The Left and Right PIN Diode

Analyzing the data taken with the left and right PIN diode relies heavily on the efficiency calculation made available by the SIGI simulation software. Results of the relative luminosity measurement with the individual PIN diodes have a systematic error of less than 1.9% for the major part of the momentum range. For the combination of left and right PIN diode the systematic error of this method is even less than 0.9% for most beam momenta. Only for small beam momenta below 1455 MeV/c the systematic error increases to 3.0%. These error limits are confirmed, when results are compared to the luminosity measurements with the SEM. This is not the required accuracy to allow the two PIN diodes to be used as primary luminosity monitors. Nevertheless, when appropriate care is taken, they provide an excellent check for the proper operation of the SEM. This is demonstrated for samples 2-1, 3-1 and 4-2 of the data taken in April 1996. When results from the PIN diode measurements are taken seriously, these samples show a 10% discrepancy between the PIN diode measurements and the SEM results. It coincides with the target used and disappears with a change of targets. These samples should not be included in the full cross section analysis, until the effects observed are fully understood. Altogether, the left and right PIN diodes, despite their limitations, have proven their usefulness in the EDDA experiment.

5.4.2 The Inner PIN Diode

The efficiency calculations show that the inner PIN diode almost meets the properties, which led to its design: its efficiency is approximately independent of the beam momentum. Additionally, luminosity measurements with the inner PIN diode have small systematic errors, making it a strong contender for the SEM as luminosity monitor. Unfortunately, the inner PIN diode not only sees background count rate from the target, but also from the beam halo. Attempts to eliminate this background in the offline analysis were not successful. Unless measures are taken to effectively suppress this background by additional hardware the inner PIN diode is of limited use. The *sandwich design* for the PIN diodes [Hüs97] includes this additional hardware. An inner PIN diode using this design is a highly accurate luminosity monitor. Unfortunately, this design was not available in phase one of the EDDA experiment before luminosity monitoring became unnecessary at the beginning of phase two, i.e. the measurement of spin observables.

Chapter 6

Conclusion

In order to simulate the EDDA experiment a Monte Carlo software named SIGI was developed. The program SIGI is based on the Gismo package. Though some initial questions could be studied with a program based on the GEANT III toolkit, it soon became clear that only Gismo fulfilled the requirements set forth by the design of the EDDA detector. In order to cover all aspects of the EDDA experiment, SIGI extends Gismo by a hadronic shower code named MICRES, especially suitable for the intermediate energy range available. Several geometrical elements were added including the helix layer, which was particularly difficult to model. For certain parts of the detector the tracking performance was considerably improved. Finally, the touching boundary problem was solved. Only the excellent object-oriented design of Gismo enabled these extensions and allowed a seamless embedding of the new algorithms into Gismo.

This simulation code SIGI was successfully applied to a variety of questions, which arose during the design phase and the active phase of the EDDA detector. Especially the data taken by the PIN diode luminosity monitors can only be interpreted properly, if the efficiency of the PIN diodes is simulated and the results are corrected accordingly. Applying this method, the relative luminosity can be measured with a systematical error of less than 0.9 % for the major part of the momentum range and the combination of the left and right PIN diode. Only for small beam momenta below 1455 MeV/c the systematical error increases to 3.0 %. The inner PIN provides a consistent measurement of the relative luminosity with an even higher accuracy of less than 0.5 %. Unfortunately, the inner PIN diode detects background, which cannot be corrected. The systematic error of the absolute luminosity is 0.5 % for the combination of left and right PIN diode and 0.2 % for the inner PIN diode. When appropriate care is taken, luminosity measurements with the PIN diodes and the secondary electron monitor SEM agree very well. Altogether, the PIN diodes provide an excellent check for the proper operation of the luminosity monitoring in the EDDA experiment.

Appendix A

Modeling Signal Noise

The simulation software applied to the problem of PIN diode efficiencies only supplies spectra of electron energy losses in the sensitive area of the PIN counters. When comparing measured to simulated spectra, signal noise has to be taken into account. This appendix describes a method to model signal noise and fit the free parameters by minimizing the difference between simulated and measured energy loss spectra. Since the minimization process requires the variation of free parameters, it is impractical to include the model in the simulation itself. Instead, all considerations of the following sections start with a successful simulation and the unmodified energy loss spectra, not including electronic effects like signal noise.

A.1 Calculating the Effects of Signal Noise

To model the effects of signal noise, a normal distribution of noise signals is assumed. The signal noise is taken to be independent of the energy losses detected and simply added to the original energy loss signals. To compute the final energy loss spectrum including signal noise, the convolution of the original simulated spectrum and a normal distribution has to be calculated for each momentum:

$$h'_i = \sum_{j=1}^{n} h_j \cdot \frac{1}{\sigma\sqrt{2\pi}} \int_{E_i}^{E_{i+1}} \exp\left(-\frac{1}{2\sigma^2} \cdot \left(E - E_{j,center}\right)^2\right) dE \tag{A.1}$$

with:

h'_i: contents of i^{th} channel of convoluted spectrum

n: number of energy loss channels in spectrum

h_j: contents of j^{th} channel of original spectrum

E_i, E_{i+1}: lower and upper boundary of i^{th} channel

$E_{j,center} = (E_j + E_{j+1})/2$: center of j^{th} channel

σ: standard deviation of normal distribution

The equation can be interpreted as follows. To each simulated energy loss detected in a given energy loss channel j, signal noise is added. Since the exact value of the simulated energy loss is lost at this stage of the analysis, the energy loss $E_{j,center}$ is used instead. The energy loss $E_{j,center}$ corresponds to the center of the j^{th} energy loss channel and is a good estimate for the mean energy loss of all entries in this channel. The probability that the energy loss $E_{j,center}$ is shifted into the i^{th} bin ranging from E_i to E_{i+1} due to signal noise, is expressed by the integral in the equation. This probability is multiplied with the contents h_j of the j^{th} energy loss channel, which basically implies that the contents h_j is distributed among its neighboring channels. Consequently, the contents of a channel h'_i in the convoluted spectrum is simply the sum of all contributions from neighboring channels h_j.

The standard deviation σ of the normal distribution is a free parameter and has to be determined from data. It is assumed constant for all beam momenta during an accelerator cycle and for all samples of data taken in April 1996. The standard deviation σ should merely depend on the PIN diode used. For each momentum p_k the simulated, convoluted spectrum and the spectrum extracted from the corresponding set of EDDA runs are used to calculate the following $\chi_k{}^2$:

$$\chi_k^2 = \sum_{i=1}^{n} \left(c_k \cdot h'_i - d_i\right)^2 \;/\; \sqrt{c_k^2 \cdot \Delta h'^2_i + \Delta d_i^2} \qquad \text{(A.2)}$$

with:
h'_i, $\Delta h'_i$: contents and error of ith channel in the simulated, convoluted energy loss spectrum
d_i, Δd_i: contents and error of ith channel in the measured energy loss spectrum
c_k: momentum dependent scale factor
n: number of channels in an energy loss spectrum

Since the standard deviation σ is assumed independent of the beam momentum, it should be fitted for all momentum bins simultaneously. For all momenta p_k the $\chi_k{}^2$ are summed to give an overall χ^2, which is then minimized to fit σ. This procedure is repeated for all PIN diodes. Results are presented in the next section.

The scale factor c_k in Equation (A.2) has to be determined, still. It gives credit to the fact that simulated and measured spectra were taken with differing luminosities. It may be unusual to consider simulated data to be taken with a certain luminosity. Nevertheless, this luminosity can be calculated from the number of simulated events and the given cross section of the reaction studied.

For each momentum the detected hits n_{det} scale with the luminosity L of beam and target, the detector efficiency ε and the cross section σ of the reaction studied:

$$n_{det} = \varepsilon \cdot L \cdot \sigma \tag{A.3}$$

This holds for measured and simulated data. The cross section σ can be considered identical in the measurement and the simulation. Additionally, the detector efficiency ε should be approximately equal for simulated and measured data. In fact, the idea of simulations is to provide an accurate model of reality and compute physical quantities like the detector efficiency ε based on this model. Then, the luminosities of simulated and measured data are equal, if the number of detected hits are identical. In order to compare spectra taken with identical luminosities, the scaling factor c_k has to be chosen according to:

$$c_k = \frac{n_{data}}{n_{sim}} \tag{A.4}$$

with: n_{sim}: number of detected hits in the simulation
n_{data}: number of detected hits in the measurement

Again, this choice for the scaling factor c_k is not imperative, since it is based on the assumption that simulated and real detector efficiency are identical. This is obviously only an approximation. Unfortunately, the real detector efficiency is not known, making the choice given for the scaling factor c_k the best choice available.

A.2 Results

The fit results for the standard deviation σ describing the normal distribution of signal noise in the simulation model of the PIN diodes are presented in the following table.

PIN diode	σ_{PIN}
inner	31 ± 5 keV
right	48 ± 5 keV
left	48 ± 5 keV

Table A.1: Fit results for standard deviation σ of the normal distribution describing signal noise in the PIN diodes

Appendix B

Listing of Errors

In Chapter 4 several input parameters to the calculation of the luminosity per count and their error propagation were examined. Only an overall error combined for each PIN diode setup and beam momentum was given. This appendix gives a detailed listing of the results for all combinations of PIN diodes, beam momenta and parameters examined.

B.1 Definitions

This section gives a short explanation of the input parameters studied in the error analysis. For an extensive discussion the reader is referred to Chapter 4.

To model the overlap of target and beam, event vertices are chosen from a normal distribution along the x-axis, while y- and z-coordinate are fixed. The corresponding input parameters to the simulation are denoted x_{total} and σ_x (mean and standard deviation of the normal distribution) and y_{total} and z_{total}. The beam direction is described by the parameters x'_{total} and y'_{total}. Other input parameters are the thickness d_{active} and the area $l_{active} \times l_{active}$ of the active silicon volume in a PIN diode. Finally, the thickness d_{Al} of the beampipe window is an important input parameter for simulations of the left and right PIN diode.

Several sources of error can contribute to the error of a given input parameter, e.g. Δx_{pipe} (the misalignment of beampipe and outer layer) and Δx_{PIN} (the misalignment of PIN diode and beampipe) contribute to Δx_{total}. Contributions may be momentum dependent or independent. The propagation of the two classes of errors differs dramatically; results are listed in two tables, accordingly. For momentum independent contributions the error of Q_{1455} is negligible.

Q is the quotient of luminosity per count L_p simulated at a given momentum p over the luminosity per count L_{1455} simulated at 1455 MeV/c. Q combines all simulation related quantities and was studied at beam momenta 1000 MeV/c, 1455 MeV/c and 2500 MeV/c. The error analysis distinguishes between errors of the absolute and the relative normalization. The simulation related contributions to the error of the relative normalization will be denoted ΔQ_{1000}, ΔQ_{1455} and ΔQ_{2500}. The simulation related contribution to the error of the absolute normalization will be denoted ΔQ_{norm}.

B.2 The Left PIN Diode

The following tables give detailed results for the simulation related systematic errors for the left PIN diode and the beam momenta and parameters studied.

Parameter	**Error**	ΔQ_{norm}	ΔQ_{1000}	ΔQ_{1455}	ΔQ_{2500}
$\Delta x_{\mathrm{total}}$	1.0 mm	1.4 %	1.3 %	1.4 %	1.4 %
$\Delta\sigma_x$	0.50 mm	0.15 %	0.28 %	0.15 %	0.054 %
$\Delta x'_{\mathrm{total}}$	0.50 mrad	0.053 %	0.065 %	0.053 %	0.16 %
$\Delta y'_{\mathrm{total}}$	0.50 mrad	0.056 %	0.034 %	0.056 %	0.014 %
		1.5 %	1.3 %	1.4 %	1.4 %

Table B.1: Systematic errors for momentum dependent sources of error and for the left PIN diode.

Parameter	**Error**	ΔQ_{1000}	ΔQ_{2500}
$\Delta x_{\mathrm{total}}$	0.50 mm	1.1 %	0.12 %
$\Delta y_{\mathrm{total}}$	1.3 mm	0.20 %	0.066 %
$\Delta z_{\mathrm{total}}$	1.3 mm	2.4 %	0.21 %
$\Delta x'_{\mathrm{total}}$	0.70 mrad	0.16 %	0.19 %
$\Delta y'_{\mathrm{total}}$	0.80 mrad	0.15 %	0.082 %
$\Delta d_{\mathrm{active}}$	10 µm	0.14 %	0.010 %
$\Delta l_{\mathrm{active}}$	0.50 mm	0.22 %	0.32 %
Δd_{Al}	5.0 µm	1.9 %	0.41 %
		3.3 %	0.61 %

Table B.2: Systematic errors for momentum independent sources of error and for the left PIN diode.

B.3 The Right PIN Diode

The following tables give detailed results for the simulation related systematic errors for the right PIN diode and the beam momenta and parameters studied.

Parameter	Error	ΔQ_{norm}	ΔQ_{1000}	ΔQ_{1455}	ΔQ_{2500}
Δx_{total}	1.0 mm	1.5 %	1.7 %	1.5 %	1.4 %
$\Delta\sigma_x$	0.50 mm	0.21 %	0.36 %	0.21 %	0.12 %
$\Delta x'_{total}$	0.50 mrad	0.26 %	0.28 %	0.26 %	0.13 %
$\Delta y'_{total}$	0.50 mrad	0.027 %	0.061 %	0.027 %	0.014 %
		1.6 %	1.7 %	1.6 %	1.4 %

Table B.3: Systematic errors for momentum dependent sources of error and for the right PIN diode.

Parameter	Error	ΔQ_{1000}	ΔQ_{2500}
Δx_{total}	0.50 mm	1.1 %	0.12 %
Δy_{total}	1.5 mm	0.23 %	0.019 %
Δz_{total}	1.5 mm	2.6 %	0.41 %
$\Delta x'_{total}$	0.70 mrad	0.30 %	0.41 %
$\Delta y'_{total}$	0.80 mrad	0.058 %	0.020 %
Δd_{active}	10 μm	0.049 %	0.057 %
Δl_{active}	0.50 mm	1.8 %	1.2 %
Δd_{Al}	5.0 μm	1.7 %	0.38 %
		3.7 %	1.4 %

Table B.4: Systematic errors for momentum independent sources of error and for the right PIN diode.

B.4 Combination of Left and Right PIN Diode

The following tables give detailed results for the simulation related systematic errors for the beam momenta and parameters studied. The reader is reminded that for the error analysis of the combination of left and right PIN diode, the combined luminosity per count *L* was defined as arithmetic mean of the left and right luminosity per count.

Parameter	Error	ΔQ_{norm}	ΔQ_{1000}	ΔQ_{1455}	ΔQ_{2500}
Δx_{total}	1.0 mm	0.49 %	0.89 %	0.49 %	0.55 %
$\Delta \sigma_x$	0.50 mm	0.18 %	0.32 %	0.18 %	0.25 %
$\Delta x'_{total}$	0.50 mrad	0.023 %	0.054 %	0.023 %	0.066 %
$\Delta y'_{total}$	0.50 mrad	0.017 %	0.047 %	0.017 %	0.014 %
		0.69 %	0.95 %	0.52 %	0.61 %

Table B.5: Systematic errors for momentum dependent sources of error and for the combination of left and right PIN diode.

Parameter	Error	ΔQ_{1000}	ΔQ_{2500}
Δx_{total}	0.59 mm	0.24 %	0.088 %
Δy_{total}	1.2 mm	0.19 %	0.029 %
Δz_{total}	1.2 mm	2.2 %	0.22 %
$\Delta x'_{total}$	0.70 mrad	0.11 %	0.056 %
$\Delta y'_{total}$	0.80 mrad	0.10 %	0.033 %
Δd_{active}	10 µm	0.090 %	0.023 %
Δl_{active}	0.50 mm	0.78 %	0.43 %
Δd_{Al}	5.0 µm	1.5 %	0.29 %
		2.9 %	0.58 %

Table B.6: Systematic errors for momentum independent sources of error and for the combination of left and right PIN diode.

B.5 The Inner PIN Diode

The following tables give detailed results for the simulation related systematic errors for the inner PIN diode and the beam momenta and parameters studied. Sources of error related to the misalignment of beampipe and outer layer are missing in the tables, because the position of the inner PIN diode was extracted from data taken with the outer layer. For obvious reasons, the thickness d_{Al} of the beampipe window does not contribute either.

Parameter	Error	ΔQ_{norm}	ΔQ_{1000}	ΔQ_{1455}	ΔQ_{2500}
Δx_{total}	1.0 mm	0.13 %	0.077 %	0.13 %	0.12 %
$\Delta \sigma_x$	0.50 mm	0.029 %	0.016 %	0.029 %	0.025 %
$\Delta x'_{total}$	0.50 mrad	0.015 %	0.019 %	0.015 %	0.012 %
$\Delta y'_{total}$	0.50 mrad	0.16 %	0.24 %	0.16 %	0.17 %
		0.21 %	0.26 %	0.21 %	0.21 %

Table B.7: Systematic errors for momentum dependent sources of error and for the inner PIN diode.

Parameter	Error	ΔQ_{1000}	ΔQ_{2500}
Δx_{total}	0.50 mm	0.023 %	0.007 %
Δy_{total}	1.5 mm	0.28 %	0.29 %
Δz_{total}	1.2 mm	0.23 %	0.20 %
Δd_{active}	10 µm	0.031 %	0.017 %
Δl_{active}	0.50 mm	0.11 %	0.28 %
		0.37%	0.45%

Table B.8: Systematic errors for momentum independent sources of error and for the inner PIN diode.

B.6 Summary of Error Estimates

In the following table the results of all errors for each particular PIN diode and the combination of left and right PIN diode are summed and listed. The overall systematic errors of the relative normalization is given for each momentum studied. In addition, the overall systematic error of the absolute normalization is listed. These results are also presented and discussed in great detail in Chapter 4.

PIN diode	ΔQ_{norm}	ΔQ_{1000}	ΔQ_{1455}	ΔQ_{2500}
inner	0.2 %	0.4 %	0.2 %	0.5 %
left+right	0.5 %	3.0 %	0.5 %	0.9 %
right	1.5 %	4.0 %	1.5 %	1.9 %
left	1.4 %	3.5 %	1.4 %	1.5 %

Table B.9: Overall systematic errors for the different PIN diodes and the combination of left and right PIN diode.

For convenience the following table combines the systematic errors of the relative and absolute normalization. Simulation related contributions to the systematic error of the luminosity are denoted ΔL_{1000}, ΔL_{1455} and ΔL_{2500}.

PIN diode	ΔL_{1000}	ΔL_{1455}	ΔL_{2500}
inner	0.5 %	0.3 %	0.6 %
left+right	3.1 %	0.7 %	1.0 %
right	4.3 %	2.1 %	2.9 %
left	3.8 %	2.0 %	2.1 %

Table B.10: Combination of the systematic errors of the relative and absolute normalization for the different PIN diodes and the combination of left and right PIN diode.

Appendix C

Listing of PIN Diode Efficiencies

Chapter 5 presented results for the efficiency simulations of the PIN diodes used in April 1996. To provide a concise treatment, efficiencies and luminosities per count were only shown for one specific beam and target setup, represented by run 965. Then, the important comparison of luminosity measurements with PIN diodes and secondary electron monitor SEM was carried out in great detail. A full listing of efficiencies and luminosities per count for all combinations of PIN diode, beam momentum and representative run was missing. It is given in this appendix. For reference, results for all combinations of beampipe window thickness and PIN diodes are listed.

C.1 Definitions

The following sections give the complete listings for the detection efficiency $\varepsilon_{\mathrm{det}}$ and the luminosity per count L_{count} for all combinations of PIN diode, beam momentum and representative run examined. The detection efficiency ε_{det} is defined as the number of detected hits divided by the number of geometrical hits. The exact definition of detected and geometrical hits is given in Subsection 3.2.4. This definition of efficiency was chosen, because of its simple physical interpretation. The efficiency of Equation (3.8) is related to the detection efficiency ε_{det}, if the solid angle Ω_0 is chosen to be the solid angle covered by the PIN diode examined.

C.2 Results

In the following listings no errors are given. A complete discussion of errors was given in Chapter 4. The statistical errors of the results vary little with beam momentum and are better than 0.6 % (0.35 % inner PIN diode) for the detection efficiency ε_{det} and 0.5 % (0.24 % inner PIN diode) for the luminosity per count L_{count}.

	run 183		run 421		run 965	
p_{beam} [MeV/c]	ε_{det} [%]	L_{count} [1/mb]	ε_{det} [%]	L_{count} [1/mb]	ε_{det} [%]	L_{count} [1/mb]
1000	103.2	0.190	103.1	0.190	103.2	0.190
1050	103.2	0.209	103.1	0.207	103.2	0.209
1100	103.2	0.228	103.3	0.228	103.2	0.228
1150	103.2	0.244	103.1	0.243	103.2	0.244
1200	103.2	0.262	103.2	0.260	103.2	0.262
1250	103.1	0.278	103.1	0.277	103.2	0.280
1300	103.1	0.293	103.1	0.292	103.1	0.293
1350	103.1	0.309	103.0	0.308	103.1	0.307
1400	103.0	0.322	102.9	0.321	102.9	0.321
1450	102.8	0.335	102.9	0.333	102.9	0.335
1500	102.8	0.348	102.8	0.347	102.8	0.348
1550	102.8	0.359	102.8	0.357	102.7	0.359
1600	102.6	0.371	102.7	0.369	102.6	0.371
1650	102.7	0.381	102.7	0.378	102.6	0.378
1700	102.5	0.387	102.5	0.387	102.5	0.388
1750	102.5	0.398	102.4	0.396	102.4	0.398
1800	102.4	0.405	102.5	0.403	102.4	0.406
1850	102.3	0.411	102.4	0.413	102.4	0.413
1900	102.3	0.419	102.4	0.418	102.3	0.419
1950	102.3	0.427	102.3	0.423	102.4	0.427
2000	102.2	0.433	102.2	0.432	102.3	0.433
2050	102.2	0.437	102.2	0.438	102.2	0.438
2100	102.1	0.443	102.1	0.444	102.2	0.444
2150	102.2	0.448	102.2	0.446	102.2	0.447
2200	102.1	0.453	102.1	0.447	102.2	0.452
2250	102.1	0.456	102.1	0.455	102.1	0.457
2300	102.0	0.461	102.0	0.458	102.1	0.461
2350	102.0	0.463	102.0	0.462	102.0	0.466
2400	102.0	0.467	102.1	0.466	102.0	0.465
2450	102.0	0.471	102.0	0.470	102.0	0.472
2500	101.9	0.472	101.9	0.472	102.0	0.474
2550	101.9	0.476	102.0	0.475	102.0	0.475
2600	101.9	0.477	101.9	0.476	102.0	0.479
2650	101.9	0.481	102.0	0.479	101.9	0.480
2700	101.9	0.483	101.9	0.481	101.9	0.484
2750	101.9	0.485	101.9	0.481	102.0	0.485
2800	101.8	0.488	101.9	0.486	101.8	0.488
2850	101.8	0.489	101.9	0.486	101.9	0.488
2900	101.9	0.493	101.8	0.491	101.9	0.490
2950	101.8	0.492	101.8	0.489	101.9	0.492
3000	101.9	0.494	101.8	0.492	101.8	0.493
3050	101.8	0.495	101.9	0.494	101.9	0.494
3100	101.8	0.496	101.8	0.495	101.9	0.497
3150	101.8	0.498	101.8	0.497	101.8	0.498
3200	101.8	0.499	101.8	0.498	101.8	0.499
3250	101.8	0.499	101.9	0.501	101.9	0.500
3300	101.8	0.502	101.8	0.498	101.9	0.502

Table C.1: Full listing of simulation results for the inner PIN diode.

	run 183		**run 421**		**run 965**	
p_{beam} **[MeV/c]**	ε_{det} **[%]**	L_{count} **[1/mb]**	ε_{det} **[%]**	L_{count} **[1/mb]**	ε_{det} **[%]**	L_{count} **[1/mb]**
1000	41.4	1.011	42.2	1.003	39.5	1.029
1050	46.0	0.991	47.8	0.976	45.6	0.984
1100	51.0	0.967	52.4	0.962	50.3	0.964
1150	55.4	0.959	56.1	0.962	54.1	0.962
1200	58.9	0.958	60.2	0.961	58.2	0.960
1250	62.5	0.968	63.3	0.967	61.4	0.973
1300	64.7	0.983	65.4	0.984	64.4	0.974
1350	67.1	0.993	68.6	0.987	66.5	0.988
1400	69.0	1.009	70.0	1.014	69.4	0.991
1450	71.7	1.010	72.1	1.017	70.9	1.011
1500	72.7	1.030	74.3	1.030	72.8	1.019
1550	74.6	1.039	75.4	1.043	74.2	1.032
1600	76.2	1.047	77.4	1.051	75.7	1.044
1650	78.5	1.051	77.7	1.066	77.2	1.052
1700	78.5	1.073	79.0	1.079	78.1	1.063
1750	79.6	1.081	79.7	1.093	79.7	1.066
1800	81.1	1.088	81.3	1.092	80.9	1.076
1850	82.2	1.098	83.0	1.099	81.6	1.090
1900	83.0	1.106	82.4	1.116	81.9	1.103
1950	83.2	1.116	83.8	1.120	83.6	1.108
2000	84.7	1.121	85.0	1.130	83.4	1.121
2050	84.9	1.127	85.0	1.141	84.7	1.125
2100	85.6	1.135	86.1	1.145	85.0	1.125
2150	85.9	1.145	86.8	1.150	85.5	1.142
2200	86.7	1.143	86.9	1.150	86.6	1.138
2250	87.6	1.147	87.5	1.163	88.2	1.136
2300	87.3	1.163	88.5	1.161	86.8	1.153
2350	88.2	1.157	88.5	1.164	87.9	1.153
2400	88.9	1.160	87.6	1.175	88.0	1.158
2450	88.9	1.165	89.2	1.173	88.1	1.163
2500	89.3	1.166	89.5	1.173	88.6	1.164
2550	89.3	1.173	89.4	1.175	89.6	1.162
2600	89.9	1.173	90.2	1.178	89.5	1.166
2650	90.0	1.176	90.6	1.178	89.4	1.171
2700	90.4	1.180	90.9	1.179	90.2	1.177
2750	90.4	1.183	90.7	1.181	91.0	1.169
2800	90.8	1.182	90.6	1.185	90.7	1.176
2850	91.2	1.181	90.7	1.192	91.7	1.174
2900	92.0	1.178	92.2	1.185	91.1	1.183
2950	91.3	1.187	92.3	1.189	91.6	1.179
3000	92.6	1.185	93.0	1.194	92.0	1.189
3050	91.7	1.190	92.4	1.197	93.0	1.186
3100	91.6	1.204	92.6	1.201	91.9	1.194
3150	92.4	1.195	92.0	1.207	92.5	1.195
3200	93.2	1.190	93.3	1.201	92.5	1.199
3250	93.4	1.189	93.9	1.208	93.1	1.194
3300	93.1	1.195	93.0	1.210	92.9	1.207

Table C.2: Full listing of simulation results for the left PIN diode mounted into a beampipe window of thickness $d_{Al} = 250\,\mu$m.

	run 183		**run 421**		**run 965**	
p_{beam} [MeV/c]	ε_{det} [%]	L_{count} [1/mb]	ε_{det} [%]	L_{count} [1/mb]	ε_{det} [%]	L_{count} [1/mb]
1000	46.7	0.940	46.0	0.925	48.5	0.932
1050	51.3	0.937	50.7	0.921	52.6	0.938
1100	55.3	0.946	54.8	0.931	56.3	0.950
1150	58.5	0.964	57.7	0.946	59.4	0.966
1200	61.6	0.979	60.8	0.966	62.7	0.982
1250	64.0	1.000	63.4	0.987	64.2	1.015
1300	66.5	1.017	66.1	1.000	66.2	1.031
1350	68.9	1.032	66.9	1.028	69.3	1.039
1400	69.6	1.061	69.7	1.038	70.4	1.066
1450	72.0	1.069	70.8	1.058	72.2	1.079
1500	73.5	1.086	73.4	1.065	73.9	1.089
1550	74.2	1.099	74.1	1.083	75.4	1.104
1600	75.8	1.108	75.5	1.093	76.4	1.117
1650	77.5	1.114	76.8	1.104	77.8	1.133
1700	78.3	1.130	77.8	1.112	77.9	1.145
1750	79.7	1.133	78.4	1.128	79.0	1.156
1800	79.2	1.155	79.5	1.130	80.1	1.155
1850	81.0	1.150	80.3	1.144	81.7	1.154
1900	81.7	1.161	81.2	1.146	82.0	1.171
1950	82.3	1.172	82.2	1.148	82.5	1.176
2000	82.6	1.171	82.1	1.166	83.3	1.180
2050	84.2	1.177	83.1	1.156	84.2	1.178
2100	84.6	1.178	83.4	1.164	84.0	1.194
2150	85.6	1.183	84.0	1.173	85.8	1.191
2200	84.3	1.198	84.6	1.176	85.0	1.198
2250	85.8	1.192	84.9	1.182	85.5	1.199
2300	86.2	1.197	86.4	1.178	87.8	1.195
2350	86.8	1.196	86.0	1.186	87.0	1.204
2400	87.1	1.199	86.6	1.189	87.2	1.206
2450	87.6	1.202	87.2	1.189	87.9	1.208
2500	87.4	1.204	87.4	1.197	87.9	1.215
2550	88.3	1.208	87.6	1.201	87.6	1.225
2600	88.5	1.211	88.1	1.203	88.8	1.223
2650	89.1	1.214	88.8	1.201	89.1	1.218
2700	89.3	1.217	89.8	1.203	89.1	1.229
2750	89.5	1.218	89.2	1.207	89.7	1.225
2800	89.1	1.225	89.5	1.205	90.1	1.224
2850	89.5	1.223	89.6	1.212	89.5	1.228
2900	90.2	1.221	90.9	1.202	90.9	1.229
2950	90.1	1.226	90.1	1.209	90.6	1.232
3000	90.1	1.226	90.7	1.210	90.1	1.228
3050	91.1	1.222	89.4	1.218	91.4	1.226
3100	90.7	1.227	90.6	1.209	90.5	1.232
3150	91.8	1.222	89.9	1.218	91.5	1.227
3200	91.3	1.223	90.7	1.213	90.7	1.228
3250	91.3	1.231	90.7	1.209	91.3	1.227
3300	91.7	1.227	91.2	1.208	92.5	1.208

Table C.3: Full listing of simulation results for the right PIN diode mounted onto a beampipe window of thickness $d_{Al} = 229\,\mu$m.

	run 183		**run 421**		**run 965**	
p_{beam} [MeV/c]	ε_{det} [%]	L_{count} [1/mb]	ε_{det} [%]	L_{count} [1/mb]	ε_{det} [%]	L_{count} [1/mb]
1000	46.3	0.904	47.5	0.892	45.0	0.905
1050	51.2	0.889	52.4	0.891	50.2	0.895
1100	56.0	0.881	56.5	0.893	54.8	0.885
1150	59.8	0.888	60.7	0.889	58.5	0.889
1200	62.7	0.899	63.7	0.907	61.9	0.904
1250	65.8	0.919	66.3	0.924	65.1	0.917
1300	68.1	0.933	68.7	0.935	67.8	0.926
1350	70.9	0.941	71.4	0.949	70.3	0.935
1400	72.7	0.958	73.2	0.969	71.9	0.957
1450	74.3	0.974	74.9	0.979	74.0	0.969
1500	75.8	0.989	76.6	0.999	75.5	0.982
1550	77.4	1.001	78.6	1.000	76.9	0.996
1600	79.2	1.007	79.5	1.022	78.6	1.006
1650	80.2	1.028	80.9	1.024	79.7	1.020
1700	81.2	1.038	81.5	1.046	80.7	1.029
1750	82.3	1.045	82.5	1.057	81.7	1.041
1800	83.3	1.058	83.7	1.061	83.0	1.048
1850	84.1	1.072	84.3	1.081	83.7	1.062
1900	85.0	1.080	85.2	1.079	84.5	1.069
1950	85.5	1.086	85.7	1.096	85.6	1.082
2000	86.7	1.095	86.7	1.107	86.1	1.086
2050	87.2	1.098	87.4	1.111	87.2	1.092
2100	87.7	1.107	88.1	1.118	87.0	1.100
2150	88.4	1.114	88.5	1.127	87.8	1.113
2200	88.7	1.117	88.5	1.129	88.3	1.116
2250	89.0	1.129	89.5	1.137	89.4	1.121
2300	89.6	1.133	89.8	1.143	89.3	1.120
2350	90.2	1.132	90.1	1.143	89.7	1.130
2400	90.9	1.136	90.8	1.134	89.7	1.136
2450	90.7	1.142	91.0	1.150	90.2	1.135
2500	91.2	1.141	91.2	1.151	91.0	1.133
2550	91.6	1.143	91.8	1.144	91.3	1.139
2600	92.1	1.145	91.8	1.157	91.4	1.141
2650	91.8	1.153	92.2	1.157	91.5	1.144
2700	92.5	1.153	92.4	1.159	92.1	1.152
2750	92.3	1.158	92.7	1.156	92.3	1.153
2800	92.9	1.155	93.1	1.153	92.5	1.154
2850	92.9	1.159	93.3	1.158	92.8	1.159
2900	93.2	1.162	93.6	1.168	93.2	1.157
2950	93.2	1.163	93.4	1.174	93.1	1.161
3000	93.7	1.171	93.6	1.186	93.5	1.170
3050	93.7	1.165	94.1	1.175	93.7	1.178
3100	93.9	1.175	94.6	1.176	94.1	1.167
3150	94.1	1.173	94.4	1.177	94.2	1.174
3200	94.4	1.175	94.7	1.183	94.6	1.173
3250	94.8	1.171	94.8	1.196	94.6	1.175
3300	94.7	1.175	94.8	1.186	95.1	1.180

Table C.4: Full listing of simulation results for the left PIN diode mounted onto a beampipe window of thickness $d_{Al} = 229\,\mu\text{m}$.

	run 183		run 421		run 965	
p_{beam}	ε_{det}	L_{count}	ε_{det}	L_{count}	ε_{det}	L_{count}
[MeV/c]	[%]	[1/mb]	[%]	[1/mb]	[%]	[1/mb]
1000	44.1	1.022	42.6	1.026	45.7	1.015
1050	48.8	1.010	47.3	1.012	50.0	1.011
1100	53.1	1.010	52.2	1.003	54.1	1.014
1150	56.8	1.017	55.4	1.010	57.1	1.031
1200	60.1	1.028	59.0	1.021	60.3	1.045
1250	62.9	1.043	61.3	1.045	63.5	1.051
1300	64.8	1.069	64.1	1.057	65.9	1.061
1350	67.2	1.083	66.1	1.066	67.5	1.093
1400	69.3	1.093	68.3	1.085	69.7	1.103
1450	71.0	1.112	70.3	1.092	71.4	1.118
1500	72.8	1.123	71.7	1.116	72.9	1.131
1550	74.3	1.125	73.5	1.118	74.3	1.148
1600	75.2	1.144	75.0	1.128	75.5	1.159
1650	76.6	1.155	76.2	1.139	76.9	1.175
1700	78.0	1.163	77.2	1.148	78.2	1.169
1750	78.7	1.175	78.0	1.163	78.8	1.187
1800	79.4	1.181	79.5	1.158	80.1	1.185
1850	80.5	1.186	80.3	1.173	81.0	1.194
1900	81.0	1.200	81.2	1.175	82.2	1.198
1950	82.4	1.200	82.1	1.178	82.6	1.204
2000	82.2	1.205	82.5	1.189	83.0	1.213
2050	84.0	1.209	83.1	1.184	84.0	1.209
2100	84.0	1.216	83.8	1.189	84.8	1.212
2150	85.3	1.216	84.3	1.199	85.0	1.232
2200	85.1	1.217	84.3	1.209	85.7	1.219
2250	86.2	1.215	85.7	1.201	85.8	1.225
2300	86.5	1.223	86.3	1.209	87.1	1.235
2350	87.2	1.220	86.5	1.208	87.0	1.234
2400	86.9	1.232	86.8	1.216	88.1	1.225
2450	88.0	1.226	87.8	1.211	88.3	1.234
2500	88.2	1.224	88.0	1.220	88.0	1.244
2550	88.7	1.233	87.9	1.227	88.7	1.240
2600	88.7	1.238	88.6	1.227	89.3	1.248
2650	88.9	1.246	88.9	1.230	89.3	1.247
2700	89.7	1.242	89.5	1.238	90.3	1.245
2750	89.6	1.248	89.1	1.239	90.3	1.248
2800	89.7	1.248	89.8	1.232	89.7	1.261
2850	90.5	1.240	90.3	1.233	90.4	1.247
2900	90.4	1.248	90.4	1.239	91.0	1.259
2950	90.5	1.251	90.3	1.237	91.9	1.246
3000	90.9	1.246	90.8	1.240	90.8	1.250
3050	90.8	1.258	91.2	1.225	92.4	1.245
3100	91.2	1.251	90.6	1.239	91.7	1.247
3150	91.6	1.257	90.9	1.235	91.7	1.256
3200	91.7	1.248	91.0	1.240	91.7	1.246
3250	92.4	1.249	91.5	1.229	91.6	1.256
3300	92.5	1.248	91.5	1.236	92.3	1.242

Table C.5: Full listing of simulation results for the right PIN diode mounted onto a beampipe window of thickness $d_{Al} = 250\,\mu$m.

Appendix D

The PIN Window Thickness

In Chapter 5 luminosity measurements with the PIN diodes and the secondary electron monitor SEM of April 1996 were compared. Initially, agreement between the methods of measurement was not satisfactory. The thickness of the beampipe windows turned out to be the primary candidate for a discrepancy between simulation model and reality. The beampipe used in April 1996 had been unmounted and was available for examination. To determine the correct window thickness using a non-destructive method, the beampipe was transported to the material testing laboratory of BBA Friction Group in Leverkusen, Germany. This appendix presents the details of this measurement and gives the results.

D.1 Measurement Setup

The department for quality assurance of BBA Friction Group in Leverkusen has long experience in the measurement of small layers of material. Their primary responsibility is testing the quality of brake blocks and their linings, which are produced in small series during the development cycle of new products. Accordingly, their personnel is experienced and well equipped for the measurement of the window thickness of the beampipe. The following sections gives a detailed description of the equipment and methods applied and their limitations.

D.1.1 Method of Measurement

The instrument used to measure the window thickness was a Permascope M11D with a probe KB4. The probe is put into contact with the test piece, e.g. the aluminum window of the beampipe, and measures a signal, which the electronic equipment converts into a distance. The measurement technique uses the magnetic induction method according to ISO 2178 [Fis01]. Figure D.1 shows the basic principle. The soft iron core of the probe is brought into contact with the test piece. The other side of the test piece must be in close contact with an iron or steel substrate. A low frequency alternating excitation current around the iron core generates a low frequency magnetic field. The magnetic flux density depends on the distance between the probe and the ferro-magnetic substrate. A probe output signal is generated by means of a pick-up coil. In the instrument, the signal measured is translated into the thickness of the test piece based on the characteristics of the probe and a suitable mathematical conversion model.

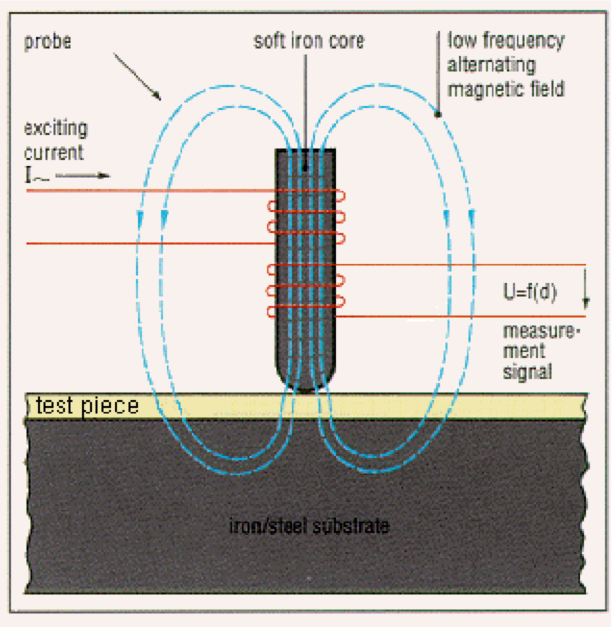

Figure D.1: Principle of the magnetic induction method ISO 2178 used to measure non-destructively the thickness of a small test piece [Fis01].

To assure proper operation of probe and instrument, test measurements of aluminum foils of known thickness were executed. Results were consistent within the required accuracy of 5 μm.

In order to measure the thickness of the beampipe windows a suitable iron or steel substrate had to be produced. The inner radius of the beampipe was measured with an accuracy of $\pm$ 5 μm and two blocks of steel were produced with dimensions $35 \times 40 \times 26$ mm^3 (see Figure D.2). Out of one side of each block material was mill-cut to fit the inner radius of the beampipe. Each block was mounted onto screws. The screws were then connected with a nut of 47 mm length. Additionally, a steel rod connected the two steel blocks and disabled distortions around the screw axis. This mechanism enabled very fine control, when inserting the steel blocks into the beampipe. By turning the nut, the steel blocks were pushed apart until the outer radius of the steel blocks fitted closely to the inner radius of the beampipe.

Figure D.2: Picture of steel substrate used as counterpart for the probe, when measuring the thickness of the beampipe windows. The nut is used to adjust the distance between the two steel blocks, until they fit closely to the inner wall of the beampipe.

D.1.2 Limitations of the Measurements

The probe KB4 has two iron cores, which are mounted parallel into a small plastic block of dimensions $6 \times 10 \times 10$ mm^3. Due to the two iron cores the probe KB4 can only measure the thickness of the test piece averaged over a small area of approximately 5×2 mm^2. Fortunately, this limitation has no negative implications, since the roughness of the surface can be expected to have only a minor influence on the PIN diode efficiency. Knowing the average thickness is sufficient for simulating the efficiencies and luminosity per count within the required accuracy.

The setup of probe, beampipe window and steel substrate allows for thin layers of air between steel substrate and beampipe. Obviously, these thin layers of air lead to a systematic error, which overestimates the window thickness. In order to avoid this problem, the probe was put with light pressure onto the window when executing a measurement.

To confirm beyond doubt that the instrument, probe and method used are applicable to the problem, Gerhard Hämmerle of Helmut Fischer GmbH + Co. KG, manufacturer of the Permascope M11D and the probe KB4, was contacted and given the full details of the measurement [Häm00]. He assured us that apart from the limitations already mentioned, results are reliable.

D.2 Results

The following sections shows a numbering scheme to identify thickness results for a particular window. Then, the different positions inside the window at which measurements were executed are presented. Finally, the results of the thickness measurements using the method of the last section are listed.

D.2.1 Numbering Scheme for the Beampipe Windows

Unfortunately, the exact mounting position of the beampipe in April 1996 cannot be reconstructed. Only the mounted position relative to the vertical axis is unambiguous, because two holes had been drilled into the beampipe at 90° and 270°. The holes were used to aid positioning the beampipe. To relate results of a measurement to the beampipe window examined, the windows were numbered with increasing ϕ starting at an arbitrary window. The numbers were written onto the beampipe. Two combinations of window number and window position (left, top, right, bottom) are possible. They are listed in the following table.

Number	Combination 1	Combination 2
1	right (ϕ=180°)	left (ϕ=0°)
2	bottom (ϕ=270°)	top (ϕ=90°)
3	left (ϕ=0°)	right (ϕ=180°)
4	top (ϕ=90°)	bottom (ϕ=270°)

Table D.1: Possible combinations of beampipe window number and window position.

A strong evidence in favor of combination 1 is the fact that window 4 was covered with tape to protect it against destruction. In April 1996 the top PIN diode was not mounted leaving the corresponding window without its protective cover. Instead the inner PIN diode was taking data at the angular position of ϕ=90°.

In Chapter 5, both combinations were simulated for the left and right PIN diode and the resulting luminosities compared to the measurements with the secondary electron monitor SEM. Only for combination 1, measurements with the SEM and PIN diode agree. This is sufficient proof that combination 1 is correct.

D.2.2 Measurement Scheme

Unlike shown in Figure D.1, the probe KB4 has two iron cores, which are mounted parallel into a small plastic block. The head of both iron cores must touch the beampipe during a measurement. The two iron cores define a natural direction of the probe KB4. For each beampipe window measurements were executed at nine positions. At six positions probe and beampipe axis were aligned, at the other three positions the probe was perpendicular to the beampipe axis. Three of the six positions with probe and beampipe aligned were upstream, three downstream. Figure D.3 shows the different positions examined. The two connected dots indicate the points, where the heads of the two iron cores touch the beampipe window.

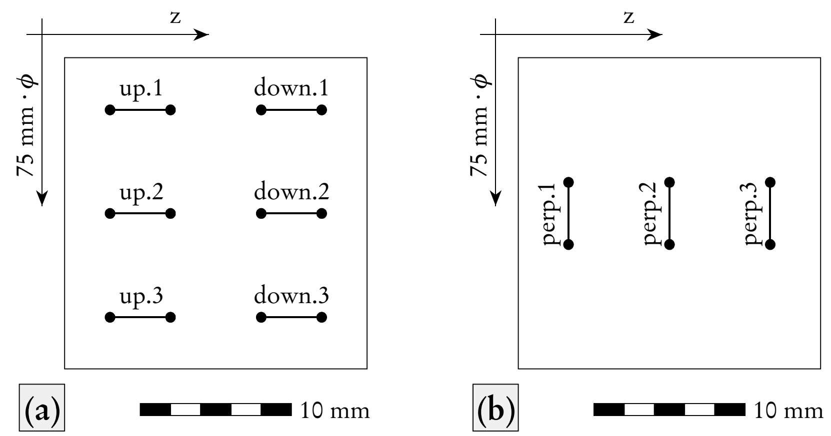

Figure D.3: The different positions of the thickness measurements for a given beampipe window: a) probe and beampipe axis aligned b) probe perpendicular to beampipe. The two connected dots indicate the points, where the heads of the two iron cores of the probe KB4 touch the beampipe window.

To ensure consistent results, measurements at a given position were repeated. The errors given in Figures D.4 to D.7 are statistical and computed from the standard deviation. From the data sheets, the error of the Permascope M11D and the probe KB4 is 1%. This amounts to approximately 2.5 μm for the measurement of the window thickness. Then, the total error of a measurement is typically 5 μm.

D.2.3 Results

Figures D.4 to D.7 present for each beampipe window the results for the measurements of the thickness at the different positions examined. The mean thickness of the beampipe window is given in Table D.2. In simulations of the left and right PIN diode, the beampipe window was modeled with constant thickness. The mean thickness of the beampipe windows given in Table D.1 was used for this purpose. Especially for the left and right PIN diode (window 1 and 3), the thickness of the window is relatively constant. The error of the thickness was estimated to be the typical error of the thickness measurements.

Window Number	**Mean Thickness d_{Al} [μm]**
1	229.0 ± 5
2	238.3 ± 5
3	251.5 ± 5
4	239.8 ± 5

Table D.2: Table of mean window thicknesses. In simulations windows are modeled with the constant thicknesses listed.

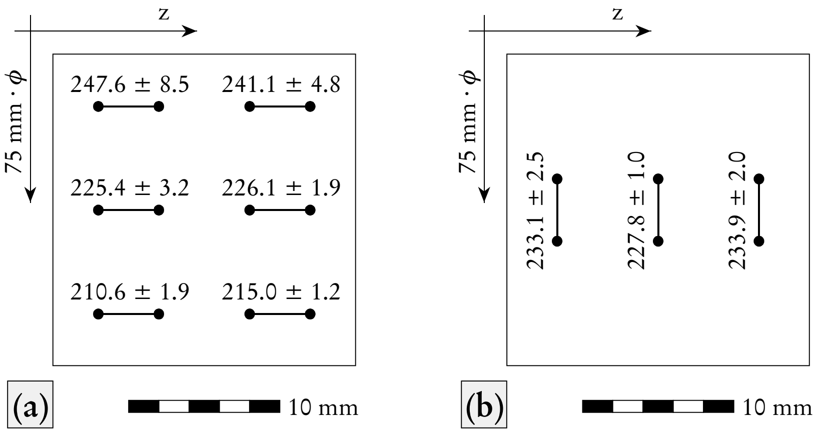

Figure D.4: Thickness results for window 1: a) probe and beampipe aligned b) probe perpendicular to beampipe. All thickness results are given in μm.

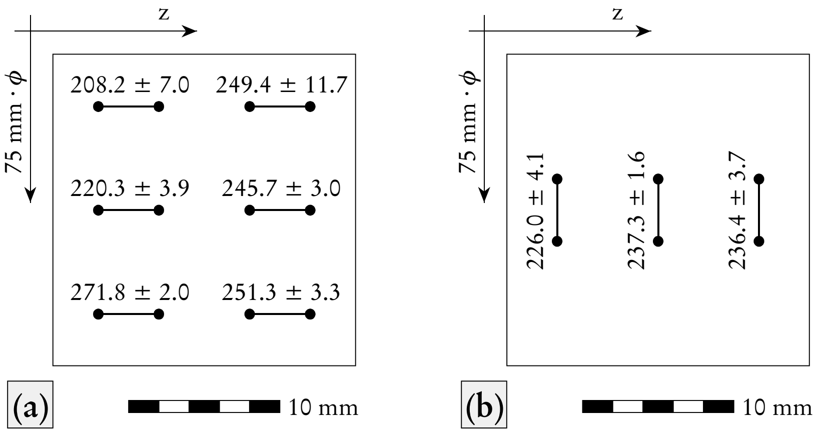

Figure D.5: Thickness results for window 2: a) probe and beampipe aligned b) probe perpendicular to beampipe. All thickness results are given in μm.

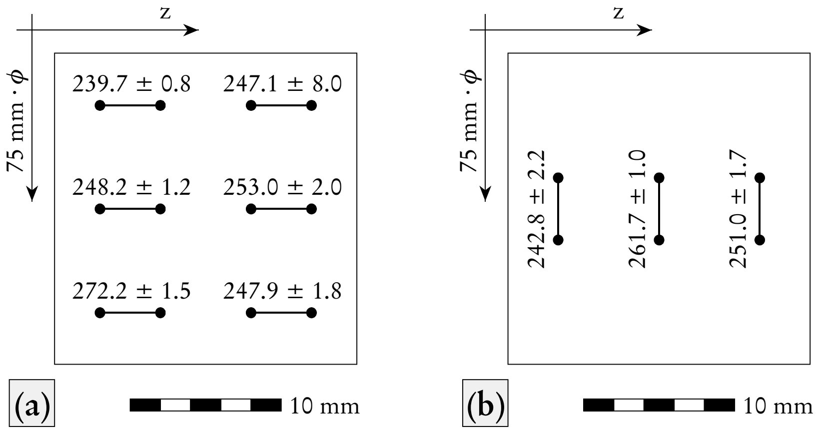

Figure D.6: Thickness results for window 3: a) probe and beampipe aligned b) probe perpendicular to beampipe. All thickness results are given in μm.

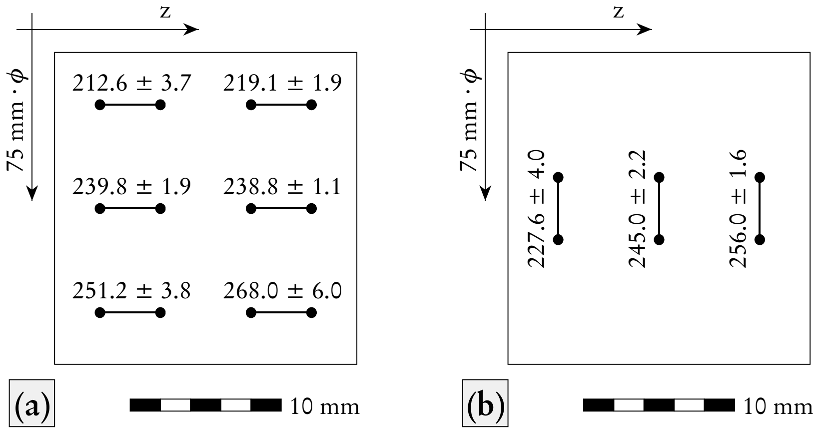

Figure D.7: Thickness results for window 4: a) probe and beampipe aligned b) probe perpendicular to beampipe. All thickness results are given in μm.

References

[Aer78] A. Th. M. Aerts et al., Phys. Rev. D **17** (1978) 260

[Alb97] D. Albers et al., Proton-proton elastic scattering excitation functions at intermediate energies, Phys. Rev. Lett. **78** (1997) 1652

[Arn97] R. A. Arndt et al., Nucleon-nucleon elastic scattering analysis to 2.5 GeV, Phys. Rev. C **56** (1997) 3005-3013

[Atw92] W. B. Atwood, T. Burnett, R. Cailliau, D. R. Myers, K. M. Storr, Gismo: An Object-Oriented Program for High-Energy Physics Event Simulation and Reconstruction, Int. Jour. o. Mod. Phys. **C3** (1992) 459

[Atw93] W. B. Atwood, A. Breakstone, D. Britton, T. Burnett, D. R. Myers, G. Word, The Gismo Project, SLAC-PUB-6135 (1993)

[Bet53] H. A. Bethe, Molière's Theory of Multiple Scattering, Phys. Rev. **89** (1953) 1256

[Bie94] A. F. Bielajew, H. Hirayama, W. R. Nelson, D. W. O. Rogers, History, Overview and Recent Improvements of EGS4, National Research Council of Canada Report NRC-PIRS-0436 (1994)

[Bru87] R. Brun et al., GEANT 3.11 users guide, Data Handling Division, DD/EE/84-1 (1987)

[Die96] O. Diehl, Private Communication (1996)

[Eng98] H. P. Engelhardt, Bestimmung des COSY-Strahlimpulses während der Hochbeschleunigung sowie Einbau und Überwachung eines Vertexdetektors aus szintillierenden Fasern für das EDDA-Experiment, Ph. D. Thesis, Univ. Bonn (1998)

[Fes85] H. Fesefeldt, The Simulation of Hadronic Showers, Physics and Applications, PITHA 85/02 (1985)

[Fis01] Fischerscope® MMS®, Universal Coating and Material Property Measurement System, Data Sheet (2001)

[Gar85] M. Garcon et al., The continuous energy dependence of pp differential elastic cross sections between 500 and 1200 MeV, Nucl. Phys. **A445** (1985) 669

[GEA95] GEANT - Detector Description and Simulation Tool, CERN Program Library Long Writeup W5013, CERN (1995), also via WWW: `http://wwwinfo.cern.ch/asdoc/geant_html3/geantall.html`

[Gea98] GEANT4: An Object-Oriented Toolkit for Simulation in HEP, LCB Status Report / RD44, CERN/LHCC 98-44 (1998), also via WWW: `http://wwwinfo.cern.ch/asd/geant/documents/StatusReport98.html`

[Gea98b] Geant4 User's Guide - For Toolkit Developers (1998)

[Gol89] T. Goldmann et al., Phys. Rev. C **39** (1989) 1889

[Gro93] R. Groß-Hardt, Simulation des EDDA-Detektors - erste Ergebnisse, Diplomarbeit, ISKP Univ. Bonn (1993)

[Häm00] G. Hämmerle, Helmut Fischer GmbH + Co. KG, Private Communication (2000)

[Hei95] A. Heine, Luminositätsüberwachung am EDDA-Experiment, Diplomarbeit, ISKP Univ. Bonn (1995)

[Hin89] F. Hinterberger, Anregungsfunktionen im p-p-Stoß, Jül-Spez-489, (1989)

[Hüs97] T. Hüskes, Verbesserung der Luminositätsüberwachung im EDDA-Experiment mit Hilfe elastischer e^-p-Streuung, Diplomarbeit, ISKP Univ. Bonn (1997)

[Jam77] F. James, FOWL - A General Monte-Carlo Phase Space Program, CERN Computer Program Library, W505 (1977)

[Jes95] M. Jeske, Test eines zylindrischen Detektors aus szintillierenden Fasern, Diplomarbeit, ISKP Univ. Bonn (1995)

[Käl64] G. Källen: Elementarteilchenphysik, Bibliographisches Institut, Mannheim (1964)

[Kal87] Yu. S. Kalashnikova et al., Yad. Fiz. **46** (1987) 1181, trans. Sov. J. Nucl. Phys. **46** (1987) 689

[KEK94] Y. Kobayashi et. al., Energy-dependent measurements of the pp elastic analyzing power and narrow dibaryon resonances, Nucl. Phys. A **569** (1994) 791

[Kno79] G. F. Knoll, Radiation detection and measurement, John Wiley and Sons (1979) 414

[Kon87] N. Konno et al., Phys. Rev. D **35** (1987) 239

[Lac80] M. Lacombe et al., Phys. Rev. C **21** (1980) 861

[Laf86] P. LaFrance and E. L. Lomon, Phys. Rev. D **34** (1986) 1341, P. Gonzáles and E. L. Lomon, ibid. D **34** (1986) 1351, P. Gonzáles, P. LaFrance and E. L. Lomon, ibid. D **35** (1987) 2142

[Lah92] U. Lahr, Ein Detektor zur Messung von Anregungsfunktionen der elastischen Proton-Proton-Streuung an COSY, Ph. D. Thesis, Univ. Bonn (1992)

[Lec93] C. Lechanoine-Leluc, F. Lehar, Rev. Mod. Phys. **65** (1993) 47

[Mac87] R. Machleidt, K. Holinde, Ch. Elster, Phys. Rep. **149** (1987) 1

[Mac89] R. Machleidt, Adv. in Nucl. Phys. **19** (1989) 189

[Mol48] G. Z. Molière, Theorie der Streuung schneller geladenere Teilchen II. Mehrfach- und Vielfachstreuung, Z. Naturforsch. 3a (1948) 78

[Mos94] F. Mosel: Ein internes Wasserstofftarget für Speicherringexperimente, Ph. D. Thesis, Univ. Bonn (1994)

[Nel85] W. R. Nelson, H. Hirayama, D. W. O. Rogers, The EGS4 Code System, SLAC Report 265 (1985)

[Nel85b] W. R. Nelson, H. Hirayama, D. W. O. Rogers, The EGS4 Code System, SLAC Report 265 (1985) 83

[Nel85c] W. R. Nelson, H. Hirayama, D. W. O. Rogers, The EGS4 Code System, SLAC Report 265 (1985) 92

[PDG94] Particle Data Group, Review of Particle Properties, Phys. Rev. D **50** (1994) 1283

[PDG94b] Particle Data Group, Review of Particle Properties, Phys. Rev. D **50** (1994) 1251

[PDG94c] Particle Data Group, Review of Particle Properties, Phys. Rev. D **50** (1994) 1253

[PDG98] Particle Data Group, C. Caso et al., Review of Particle Physics, The European Physical Journal C **3** (1998) 1

[Roh95] H. Rohdjeß. Determining COSY Beam Parameters from Elastic Proton-Proton Scattering, EDDA internal report 95-04, ISKP Univ. Bonn (1995)

[Roh96] H. Rohdjeß, Private Communication (1996)

[Roh99] H. Rohdjeß, Private Communication (1999)

[Roß94] U. Roß, Simulationen zum EDDA-Experiment mit GISMO und MICRES, Diplomarbeit, ISKP Univ. Bonn (1994)

[Sch94] H. Scheid, Methoden zur Luminositätsbestimmung am COSY-Experiment EDDA, Doktorarbeit, ISKP Univ. Bonn (1994)

[Sim93] A. J. Simon et al., Absolute pp-elastic cross section from 492 to 793 MeV, Phys. Rev. C **48** (1993) 662

[Sim96] A. J. Simon et al., Absolute pp-elastic cross sections from 492 to 793 MeV using CH_2 targets, Phys. Rev. C **53** (1996) 30

[Ste57] E. J. Sternglass, Theory of Secondary Electron Emission by High-Speed Ions, Phys. Rev. **108** (1957) 1

[Sto93] V. G. J. Stoks, Partial-wave analysis of all nucleon-nucleon scattering data below 350 MeV, Phys. Rev. C **48** (1993) 792

[Sto94] V. G. J. Stoks, Construction of high-quality NN potential models, Phys. Rev. C **49** (1994) 2950

[The92] D. Theis, Inelastic Hadron-Nucleus Collisions for General Purpose Detector Detector Simulations at Intermediate Energies, Ph. D. Thesis, Univ. Bonn (1992)

[Tho96] S. Thomas, Datenauswertung mit einem zylindrischen Hodoskop aus szintillierenden Fasern, Diplomarbeit, ISKP Univ. Bonn (1996)

[Wei95] M. A. Weiss, Algorithms, Data Structures and Problem Solving with C++, Addison-Wesley (1995) 197

[Wei95b] M. A. Weiss, Algorithms, Data Structures and Problem Solving with C++, Addison-Wesley (1995) 169

[Wei97] E. Weise, Simulationsrechnung zur elastischen Streuung polarisierter Protonen, Diplomarbeit, ISKP Univ. Bonn (1997)

[Wei99] E. Weise, Private Communication (1999)

[Wel98] A. Wellinghausen, Das EDDA-Experiment bei COSY: Elastische Proton-Proton-Streuung und die Frage nach dibaryonischen Resonanzen, Ph. D. Thesis, Univ. Hamburg (1998)

[Wie94] W. Wiedmann, Ein zylindrischer Detektor aus szintillierenden Fasern und erste Messungen zum EDDA-Experiment an COSY, Ph. D. Thesis, Univ. Bonn (1994)

[Won78] C. W. Wong and K. F. Liu, Phys. Rev. Lett. **41** (1978) 82

[Won82] C. W. Wong, Prog. Part. Nucl. Phys. **8** (1982) 223

[Zie98] R. Ziegler, Die Innenschale des EDDA-Detektors und Messungen zur elastischen Proton-Proton-Streuung, Ph.D. Thesis, Univ. Bonn (1998)

Acknowledgments

Taking the opportunity at this place, I would like to thank all persons, whose support helped in accomplishing this thesis, especially

Director Prof. Dr. K. Maier for the opportunity to complete this thesis at the Institut für Strahlen- und Kernphysik,

Prof. Dr. F. Hinterberger for the great support he provided on countless occasions discussing intricate scientific problems,

Prof. Dr. J. Ernst for acting as coreferee for this thesis and for valuable advice,

Priv. Doz. Dr. R. Rohdjeß for many useful suggestions, thereby profiting from his deep insight into the details of the experiment,

The members of the EDDA collaboration for good teamwork and cooperation, especially Dr. R. Ziegler, A. Meinerzhagen, H. J. Trelle, K. Ulbrich, Dr. M. Busch, Dr. E. Weise, Dr. V. Schwarz, Dr. A. Wellinghausen, Dr. O. Diehl, T. Hüskes, S. Thomas and U. Roß.

Furthermore, I would like to thank my family and friends for continuous encouragement. Here, I particularly want to mention my wife. Without her support this thesis would not have been possible.